

# Design of a High Impedance Preamplifier for Coil Arrays

by

John Gabriel Kauffman

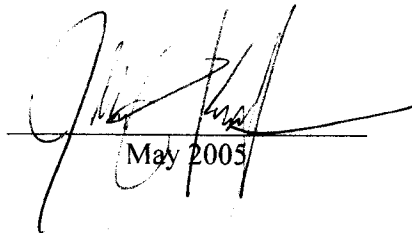
A Thesis  
Submitted to the Faculty  
of the

Worcester Polytechnic Institute

In partial fulfillment of the requirements for the  
Degree of Master of Science  
in

Electrical Engineering

by

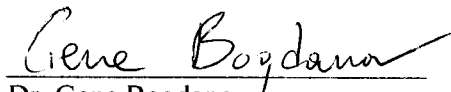


May 2005

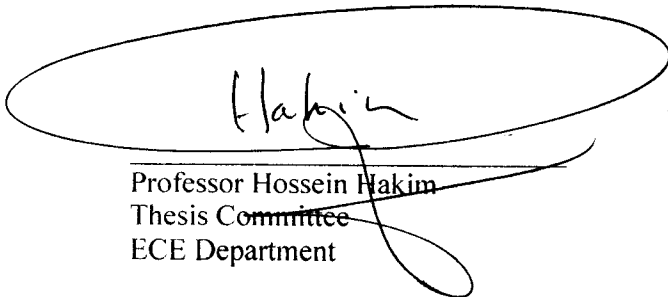
Approved:



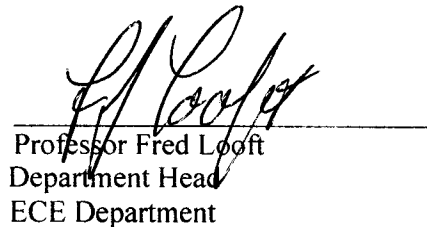
Professor Reinhold Ludwig  
Thesis Advisor  
ECE Department



Dr. Gene Bogdanov  
Thesis Committee  
ECE Department



Professor Hossein Hakim  
Thesis Committee  
ECE Department



Professor Fred Looft  
Department Head  
ECE Department

## **Abstract**

Magnetic Resonance Imaging (MRI) is a non-invasive procedure used in the medical community as a powerful way of creating images of the human anatomy. MRI is preferred over other examination techniques such as X-ray computed tomography (CT) because of its excellent soft tissue discrimination as well as the absence of ionizing radiation. Currently most clinical MRI systems use the single radio frequency coil imaging. However over past several years research has increasingly focused on the concept of using arrays of mutually decoupled surface coils. These surface coil arrays can simultaneously acquire multiple images, resulting in an increase in the field of view. This thesis pursues the design and construction of a high impedance preamplifier with the goal of investigating the decoupling of a surface coil array in a 4.7T magnetic resonance system.

## **Acknowledgements**

I would like to express my sincere gratitude and appreciation to my advisor Professor Reinhold Ludwig and Research Assistant Professor Gene Bogdanov for their guidance and encouragement throughout this thesis. I am also thankful to Professor Hossein Hakim for his willingness to serve on the thesis committee. I would also like to thank my colleagues in the RFW group at Analog Devices Inc: Eric Newman, Yuping Toh, Matthew Pilotte, Eamon Nash, Pavlo Fedorenko and Chris Huber for there time and patience. I am also very grateful and thankful for the help provided by my editor, Kimberly Johnstone.

Finally and most importantly, I would like to thank my parents John X Kauffman and Lyette Kauffman for their encouragement and support over the years.

# Table of Contents

Table of Figures .....	v
1. Introduction.....	1
1.1. Objective .....	1
1.2. Thesis Outline .....	2
2. Magnetic Resonance Imaging (MRI).....	3
2.1. Physical Principles .....	3
2.2. The Effect of an RF Pulse.....	6
2.3. Magnetic Resonance Imaging Hardware .....	10
2.3.1. Main Magnet.....	11
2.3.2. The Gradient Coils.....	11
2.3.3. The RF Transmit and Receive Coils.....	12
3. Preamplifier Design Considerations .....	13
3.1. Transistor Selection .....	13
3.2. Transistor Biasing .....	14
3.3. Stability .....	17
3.4. Impedance Matching.....	20
3.5. Quality Factor Q .....	21
3.6. Matching Network Types .....	22
3.7. Bilateral Matching .....	26
3.8. Low Noise Matching.....	28
3.9. Matching to the Coil .....	30
4. Noise Considerations .....	32
4.1. Thermal, Shot and Flicker Noise .....	32
4.2. Noise Figure and SNR .....	34
4.3. SNR in a Single Coil.....	35
4.4. SNR of an Array of Coils.....	36
4.5. Switched Versus Parallel Acquisition Arrays.....	39
4.6. Noise Figure of an Amplifier.....	40
5. Single Stage Preamplifier Design .....	42
5.1. The Demonstration Boards .....	42
5.2. ADS Simulations of Demo boards.....	44
5.3. Test Results of Demo Boards .....	48
6. Dual stage Preamplifier Design .....	52
6.1. Design and Simulation.....	52
6.2. Layout and Construction.....	66
6.3. Tested Results of the Dual stage Preamplifier.....	68
7. Testing of Decoupling Concept with Dual stage Preamplifier .....	72
7.1. Construction of Two Coils.....	73
7.2. Tuning of Coils .....	77
7.3. Simulation Check.....	80
7.4. The Magnet Test .....	82
8. Conclusion .....	87
8.1. Further Research .....	87
References.....	89

Appendix A.....	92
Measured Results on the Resistive Biased Board.....	93
Simulated Results on the Active Biased Board .....	95
Measured Results on the Active Biased Board.....	96
Appendix B .....	98
Simulated Results on dual stage Boards .....	98
Measured Results on the Dual stage Boards.....	100
Appendix C .....	104
Appendix D.....	108
Appendix E .....	132

## Table of Figures

Figure 2-1 - Magnetic dipole moment associated with spinning nucleus [11].	4
Figure 2-2 – (a) Randomly oriented nuclear magnetic moments. (b) parallel and	4
Figure 2-3 - Energy states E1 and E2 of spin alignments in a static field.	5
Figure 2-4 - (a) Spin alignment described by angle $\theta$ . (b) a collection of spins	5
Figure 2-5 - An RF pulse of 90 degrees.	7
Figure 2-6 - (a) A vector display of $T_1$ relaxation. (b) graphical example of $T_1$ relaxation over time.	8
Figure 2-7 - (a) A vector display of $T_2$ relaxation. (b) graphical example of $T_2$ relaxation over time.	8
Figure 2-8 - (a) Top view of $T_2$ relaxation.	9
Figure 2-9 – (a) Signal induced on a coil by the $T_2$ relaxation.	10
Figure 2-10 - Block diagram of a generic MRI system.	11
Figure 3-1- Transistor with active biasing network.	15
Figure 3-2 – Unconditional stability check.	18
Figure 3-3 - Example of input and output stability circles.	19
Figure 3-4 - Constant Q circles and matching example of $Q=1$ .	21
Figure 3-5 - The L Network.	22
Figure 3-6 - (a) T Network, (b) Pi Network	24
Figure 3-7 – T (top) and Pi (bottom) networks displaying virtual resistor placement.	25
Figure 3-8 - Low-Q matching Network.	25
Figure 3-9 - Generic preamplifier system with bilateral matching.	26
Figure 3-10 - Constant gain and noise input circles in the Smith Chart.	29
Figure 3-11 - Demonstration of high input reflection preamplifier matching concept.	30
Figure 4-1 - A linear array of four coils.	37
Figure 4-2 - Inductive coupling between two coils.	37
Figure 4-3 - (a) Switchable Array, (b) parallel Acquisition Array	39
Figure 4-4 - Example of a dual stage amplifier.	41
Figure 5-1 – Resistive biasing of ATF-551M4 transistor (Demo Board 1).	42
Figure 5-2 - Active biasing of ATF-551M4 transistor (Demo Board 2).	43
Figure 5-3 - (a) Stability plotted over frequency,	44
Figure 5-4 – The simulated NF of demo board 1.	45
Figure 5-5 - The simulated NF of demo board 2.	45
Figure 5-6 – Simulated gain of demo board 1.	46
Figure 5-7 – Simulated gain of demo board 2.	46
Figure 5-8 – Simulated $S_{11}$ of demo board 1.	47
Figure 5-9 - Simulated $S_{11}$ of demo board 2.	47
Figure 5-10 – (a) Constructed demo board 1, (b) constructed demo board 2.	48
Figure 5-11 – Measured NF of demo board 1.	49
Figure 5-12 – Measured NF of demo board 2.	49
Figure 5-13 – Measured $S_{21}$ gain of demo board 1.	50
Figure 5-14 – Measured $S_{21}$ gain of demo board 2.	50
Figure 5-15 – Measured $S_{11}$ of demo board 1.	51

Figure 5-16 – Measured $S_{11}$ of demo board 2.....	51
Figure 6-1 - Equivalent block diagram of first stage and second stage.....	52
Figure 6-2 - (a) Input stability circles, (b) output stability circles.....	53
Figure 6-3 - Pi attenuator deployment to create unconditional stability.....	54
Figure 6-4 - (a) Unconditional stability at the input, (b) unconditional stability at the output.....	54
Figure 6-5 - Designed dual stage preamplifier with no matching on the input or output.....	55
Figure 6-6 – Overall stability of dual stage preamplifier.....	56
Figure 6-7 - Bilateral matching representation.....	56
Figure 6-8 - (a) Noise circles, (b) gain circles, and .....	57
Figure 6-9 - Matching network for input of dual stage preamplifier.....	59
Figure 6-10 - The designed input matching network.....	61
Figure 6-11 - Simulated noise figure and minimum noise figure.....	61
Figure 6-12 - Input reflection coefficient with wide bandwidth matching network.....	62
Figure 6-13 - (a) Output matching network,.....	63
Figure 6-14 - Entire gain of dual stage preamplifier.....	63
Figure 6-15 - Entire dual stage preamplifier schematic with detuning network attached.....	65
Figure 6-16 - Dual stage preamplifier- top layer.....	67
Figure 6-17 - Dual stage preamplifier- bottom layer.....	67
Figure 6-18 - Constructed dual stage preamplifier.....	68
Figure 6-19 – Measured noise of preamp lifier.....	69
Figure 6-20 – Measured magnitude of $S_{11}$ .....	69
Figure 6-21 – The measured gain $S_{21}$ in dB.....	70
Figure 6-22 – Measured output reflection coefficient $S_{22}$ .....	71
Figure 6-23 - Two preamplifiers packaged for testing in the MRI system.....	71
Figure 7-1 - System diagram of the coil connected to the preamplifier.....	72
Figure 7-2 - The matching network required to connect the coil to the cable.....	73
Figure 7-3 - Balun constructed from tri-coaxial cable.....	75
Figure 7-4 - Layout of coil on bottom layer, with matching network with addition detuning components on top layer.....	76
Figure 7-5 - Constructed coil.....	76
Figure 7-6 - Constructed board with balun.....	76
Figure 7-7 - The Tuning setup for each coil.....	77
Figure 7-8 – Measured resonance at 200MHz and forward gain $S_{21}$ .....	78
Figure 7-9 - Matching of phase to a minimum.....	78
Figure 7-10 – The resonance splitting when coil 2 is connected to a $50\Omega$ load.....	79
Figure 7-11 - Resonance seen by coil 1 when coil 2 is decoupled.....	79
Figure 7-12 - Test simulation of coils connected to the $50\Omega$ load or preamplifier.....	80
Figure 7-13 - (a) Splitting of resonance when coil 2 is connected to $50\Omega$ ,.....	81
Figure 7-14 - The simulated isolation between coil 1 and coil 2.....	81
Figure 7-15 - Image acquired during test with CCNI preamplifier.....	84
Figure 7-16 – Image acquired during test with designed preamplifier–.....	85
Figure 7-17 - The resonance splitting in the magnet with $50\Omega$ load connected to coil 2, note the X-axis is frequency and the Y-axis is the magnitude of the resonance.....	86

# 1. Introduction

Many magnetic resonance imaging (MRI) systems use the single radio frequency coil imaging approach. Over the last several years many studies have debated with the idea of using arrays of mutually decoupled surface coils that can simultaneously acquire multiple images. This simultaneous imaging would directly translate to an increase of the field of view and the combination of each received image would lead to improving the signal-to-noise ratio (SNR) [22]. This improvement in SNR can only be obtained if the individual images are largely uncorrelated. To obtain these individual images, a high impedance preamplifier approach is needed to help in decreasing the mutual inductance of the coils. This thesis attempts to address these issues by proposing a dual stage preamplifier design solution.

## 1.1. Objective

The objective of this thesis is to design a prototype RF two-channel dual stage preamplifier with the intention to decouple two surface coils in a conventional 4.7T MRI system. To accomplish this task certain performance characteristics must be addressed. The preamplifier specifications will be as follows: an input reflection coefficient magnitude greater than 0.9, an operational bandwidth from 100MHz to 500 MHz, a gain over the bandwidth greater than 30dB and a noise figure of 0.8dB or better over the enter bandwidth. The 400MHz bandwidth requirement is not required for the decoupling of the coils, but is an additional asset of the preamplifier allowing it to perform under multiple system field strengths.



## **1.2. Thesis Outline**

This thesis is divided into eight chapters. Following the introductory chapter, Chapter 2 discusses the basic principles of magnetic resonance imaging (MRI), including a brief discussion on the role of RF coils in MRI systems. In Chapter 3, preamplifier design considerations are presented with the procedures of building a preamplifier from stability issues to matching networks. Also, the development of the matching network from the coil to the preamplifier is investigated. Chapter 4 then reviews noise considerations with the types of noise sources that exist and what pertain to MRI systems. Noise is then studied in the coils and how the mutual inductance creates more unwanted noise which can be reduced by a high impedance preamplifier. Chapter 5 investigates the biasing options of the chosen transistor by building two single stage preamplifiers, one with resistive biasing and one with active biasing. This investigation leads to Chapter 6 which is the construction and testing of four, dual stage preamplifiers. These four preamplifiers are typically needed when interfacing the coils to a multi-channel receiver system. Chapter 7 presents the design and construction of the coils which will be used to test the decoupling abilities of two preamplifiers. Finally, Chapter 8 concludes with a summary of achievements and future works. Additionally, all detailed data on the single and dual stage preamplifiers are summarized in the attached Appendices.

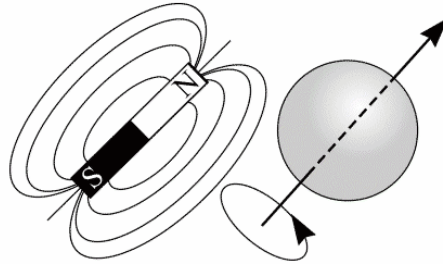
## **2. Magnetic Resonance Imaging (MRI)**

Magnetic resonance imaging (MRI) is a non-invasive procedure used in the medical community as a powerful way of creating images of the human anatomy. MRI is preferred over other clinical examination techniques such as X-ray computed tomography (CT) because of its excellent soft tissue discrimination and the fact that the patient is not exposed to ionizing radiation. MRI utilizes the properties of nuclear magnetic resonance (NMR) of hydrogen atoms to construct an image of the subject.

### **2.1. Physical Principles**

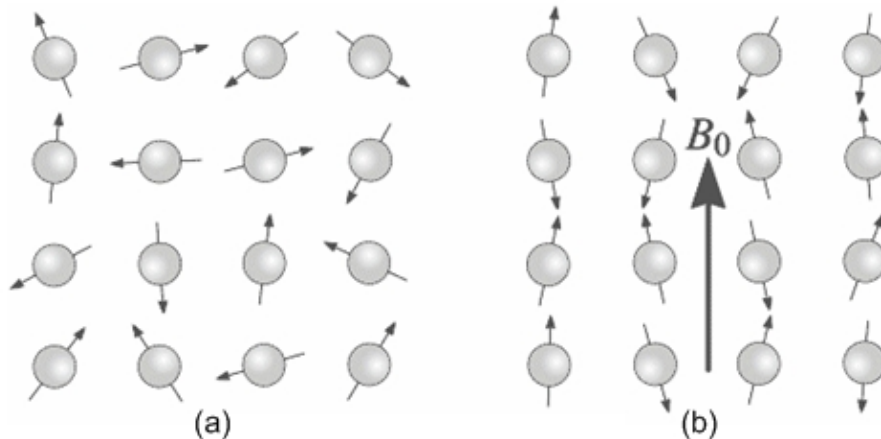
MRI technology is based on the principles of NMR; it makes use of the properties of an atomic nuclear spin angular momentum when immersed in a static magnetic field. If exposed to a second oscillating magnetic field for a limited time, a reorientation of the nuclei occurs. To provide a better intuitive understanding of how NMR works, the classical physics model will be adopted.

Figure 2-1 depicts an atomic nucleus spinning around its axis. Since the nucleus carries a net charge, the spinning motion creates a magnetic moment in accordance with Ampere's circuit law. This moment can be associated, at least in principles, with a bar magnet having both north and south poles [11]. However, the strength of the magnetic moment can differ due to the unique properties of different nuclei. The hydrogen atom is preferred over other types of atoms because it has the strongest magnetic moment and is the most abundant in biological tissue.



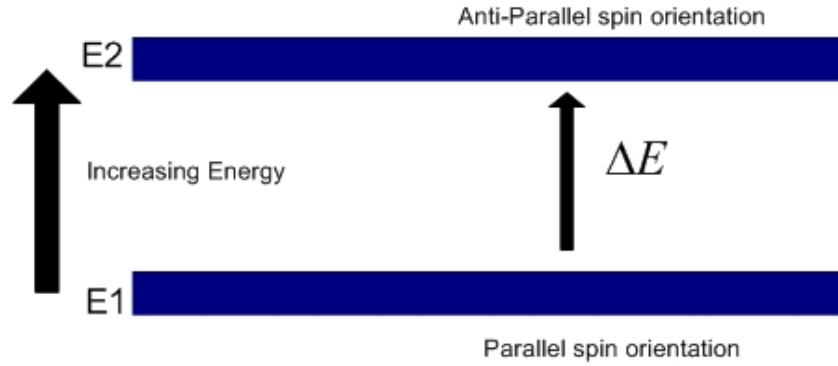
**Figure 2-1 - Magnetic dipole moment associated with spinning nucleus [11].**

Figure 2-2 (a) illustrates atoms in the absence of an externally applied magnetic field; we note that each individual atomic magnetic moment has no preferred orientation. However, when an external magnetic field  $B_0$  is applied, the magnetic moments of the atoms tend to align with the field  $B_0$ . As seen in Figure 2-2 (b), the nuclear magnetic moments in the field  $B_0$  may adopt one of two possible alignments: parallel or anti-parallel.



**Figure 2-2 – (a) Randomly oriented nuclear magnetic moments. (b) parallel and anti-parallel moments in an external magnetic field  $B_0$  [11].**

The two alignments described above each have a unique energy level associated with them, as seen in Figure 2-3. The parallel alignment with the magnetic field  $B_0$  is the lower energy state and is preferred over the anti-parallel alignment, which represents a slightly higher energy level [9].



**Figure 2-3 - Energy states E1 and E2 of spin alignments in a static field.**

When examining the alignments in more detail, the spins of the atoms are not exactly parallel or anti-parallel with respect to the applied magnetic field  $B_o$ , but are at an angle  $\theta$  seen in Figure 2-4(a). This angle  $\theta$  then causes the atom's associated spin to rotate around the applied field  $B_o$ . In Figure 2.4(b) it can be seen that the atoms are represented by vector arrows and that more atoms are aligned with the field  $B_o$  (parallel) than against it (anti-parallel). The two alignments tend to cancel each other out causing only the parallel alignments to remain under consideration as shown in Figure 2.4 (c) [11].

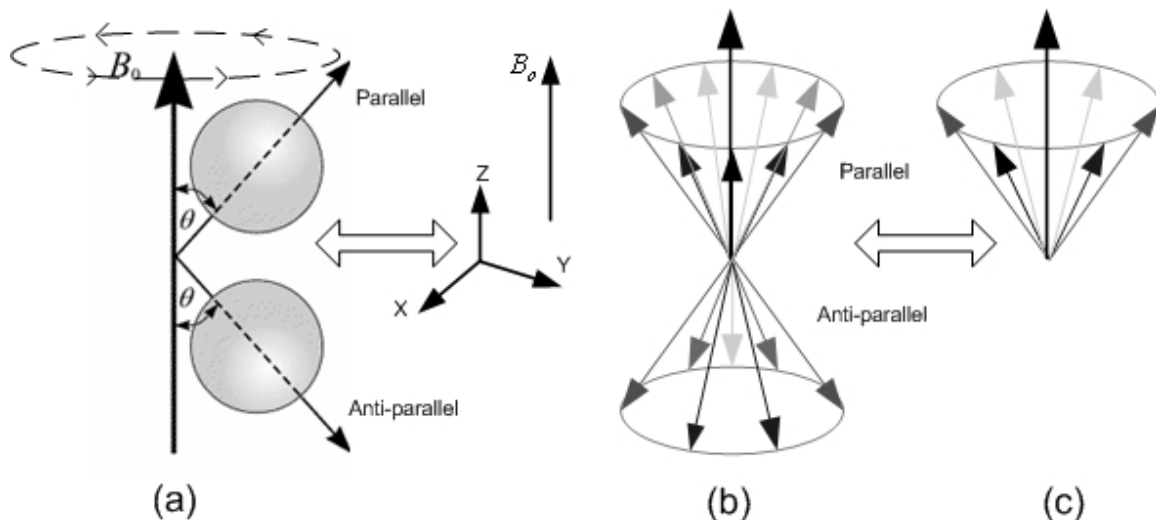


**Figure 2-4 - (a) Spin alignment described by angle  $\theta$ . (b) a collection of spins at any given time instant. (c) remaining spins after cancellation.**

If one considers only the remaining parallel alignments, the individual rotational speeds of the atoms around the field  $B_o$  can be determined. This speed is known as the Larmor frequency and can be calculated by using Equation (1). Here  $\omega$  is the Larmor angular frequency in Hz (Hertz),  $B_o$  is the strength of the magnetic field in T (Tesla) and  $\gamma$  represents the gyromagnetic ratio of the magnetic moment in Hz for the particular type of nucleus.

$$\omega = \gamma B_o \quad (1)$$

In order to detect a signal response from a subject, a second magnetic field set at the Larmor frequency needs to be introduced [9].

## **2.2. The Effect of an RF Pulse**

When applying an RF magnetic field pulse at the Larmor frequency, it interacts with the precessional motion of the nuclei. This magnetic field, known as field  $B_1$ , must be oriented perpendicular to the main field  $B_o$  to produce resonance. Resonance is the alternating absorption and dissipation of energy. The energy absorbed is from the field generated by the RF coil, while the energy dissipated is part of the relaxation process. When the RF field is turned on, the net magnetization vector begins to precess about the  $B_1$  axis. As a result, the net magnetization rotates from the longitudinal (Z) axis toward the transverse plane, then toward the  $-Z$  axis, followed by the opposite side of the transverse plane, and back to  $+Z$  and so on [11]. If the RF field is applied for a limited time, such as a finite RF pulse, an angle of rotation can be determined. This angle is termed the flip angle. In MRI practice, flip angles of  $90^\circ$  and  $180^\circ$  are of special importance in the imaging process and will be explained in more detail later.

When a RF pulse of  $90^\circ$  is applied, the pulse rotates the atoms' alignment away from the main field  $B_o$  to a new orientation parallel to the pulsed field  $B_1$ , as shown in Figure 2-5. This new alignment causes all the magnetization vectors to reside in the transverse plane. When the RF pulse ends, the atoms begin to realign with the static field  $B_o$ . This is known as relaxation. The relaxation process can be broken down into two components, a longitudinal component with time constant  $T_1$ , and a transverse component with time constant  $T_2$  [9].

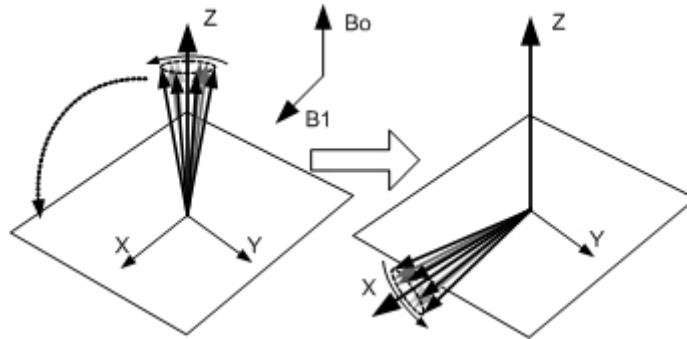


**Figure 2-5 - An RF pulse of 90 degrees.**

Demonstrated in Figure 2-6 is a vector example of longitudinal  $T_1$  relaxation. Directly after the RF pulse is introduced, the magnitude of  $M_{long}$  is close to zero in the Z-direction. Following this,  $M_{long}$  begins to realign with the main field  $B_o$  until  $M_{long} = M^o_{long}$ . Equation (2) mathematically represents this realignment over time with  $M^o_{long}$  being the magnitude of the original longitudinal alignment vector at time zero before the RF pulse is applied [11].

$$M_{long} = M^o_{long} \left( 1 - e^{-\frac{t}{T_1}} \right) \quad (2)$$

where  $T_1$  is the length of time necessary to decrease the difference between the current value of  $M_{long}$  and the equilibrium value by a factor of  $(1 - 1/e) \approx 0.63$ .

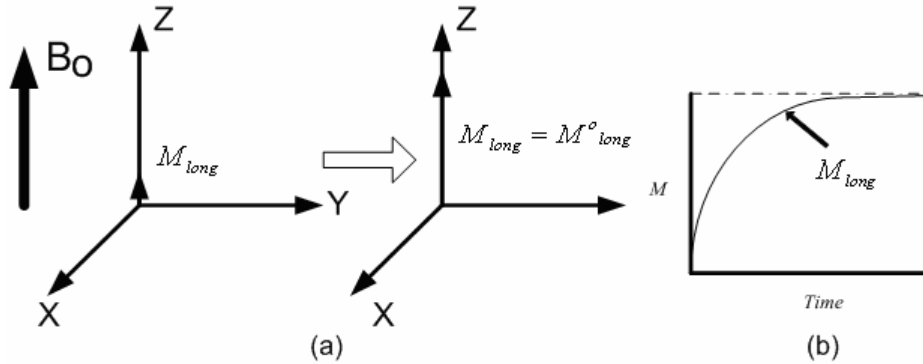


Figure 2-6 - (a) A vector display of  $T_1$  relaxation. (b) graphical example of  $T_1$  relaxation over time.

Figure 2-7 demonstrates the transversal  $T_2$  relaxation process. After the RF pulse is turned off, the alignments of the atoms are in the transverse plane. While in the transverse plane,  $M^0_{trans}$  begins to rotate around the main field  $B_0$  in a circular manner at the Larmor frequency. At the same time  $M^0_{trans}$  decreases in magnitude exponentially to zero, which can be seen in Figure 2-8(a). Equation (3) mathematically represents this realignment process over time with  $M^0_{trans}$  as the transverse magnitude at time zero when the RF pulse is applied [11].

$$M_{trans} = M^0_{trans} \cdot e^{-\frac{t}{T_2}} \quad (3)$$

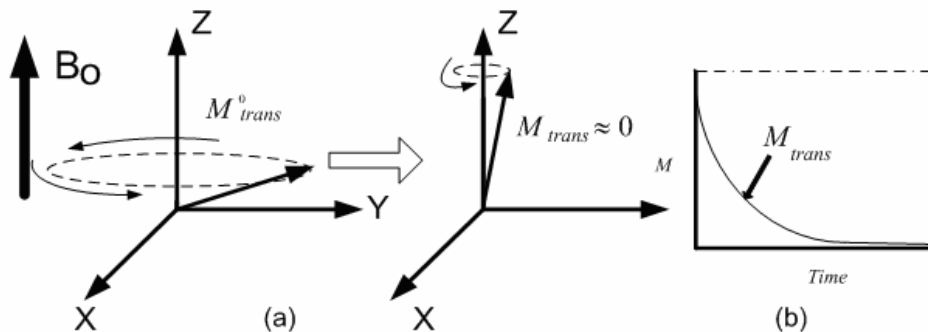
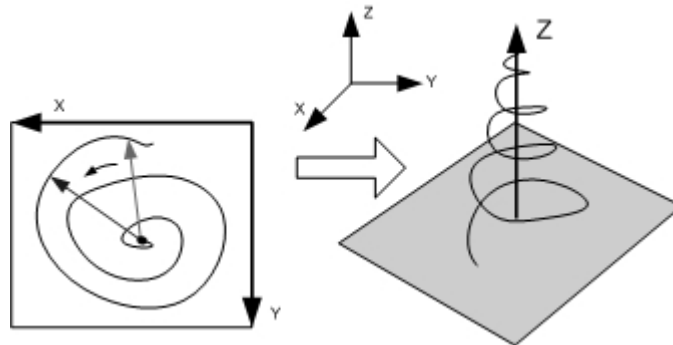


Figure 2-7 - (a) A vector display of  $T_2$  relaxation. (b) graphical example of  $T_2$  relaxation over time.

After displaying  $T_1$  and  $T_2$  in Figure 2-6 and Figure 2-7, both relaxations can be presented in a 3D manner as seen in Figure 2-8(b).



**Figure 2-8 - (a) Top view of  $T_2$  relaxation.**  
**(b) 3D display of  $T_1$  and  $T_2$  relaxation processes combined.**

There are several methods of acquiring the MRI signals and a detailed discussion of each method is beyond the scope of this thesis, only those principles pertinent to this research will be explained.

Recent interest in multiple RF receiver systems has prompted an increase in research and development of multi-coil configurations among major MR instrument vendors. Figure 2-9(a) for instance illustrates four RF coils connected to a preamplifier commonly used in the MRI process. When an RF pulse occurs, these coils will have a small AC current induced due to the time varying magnetic field produced by the relaxation of the atoms. Graphically seen in Figure 2-9 (b) is the recorded free induction decay (FID) signal response of what the coils would receive. Note that the envelope of the signal is related to the  $T_2$  relaxation and the attenuating waveform is at the Larmor frequency [5].



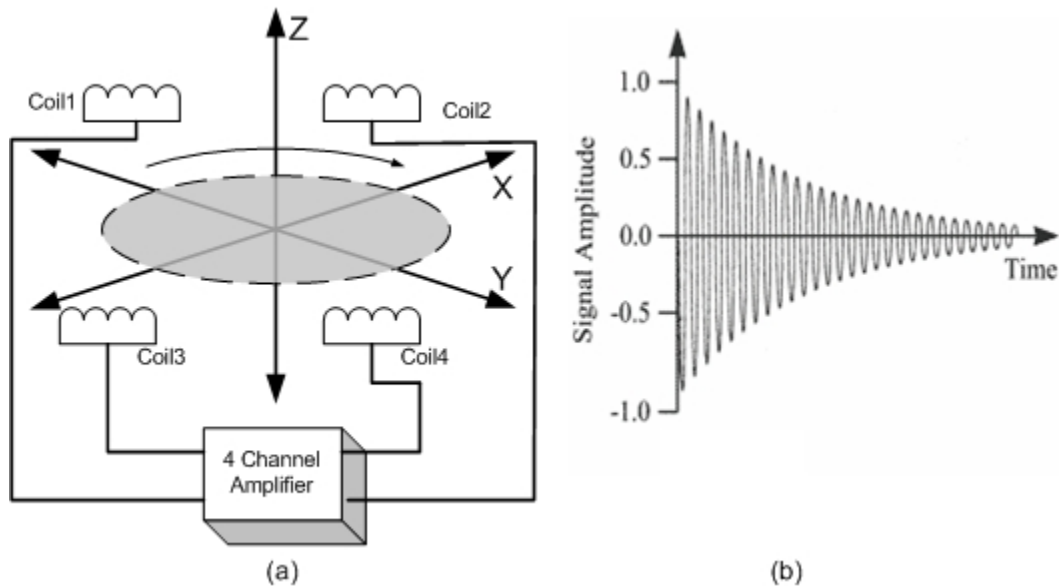


Figure 2-9 – (a) Signal induced on a coil by the  $T_2$  relaxation.  
 (b) graph of an induced signal in the coil.

This received signal is then amplified in a four-channel preamplifier as part of the MR front end system. The design of this preamplifier as well as its core properties including low noise, high gain, and high input impedance are the subject of this thesis. A more in-depth discussion will follow in subsequent chapters.

### 2.3. Magnetic Resonance Imaging Hardware

The three basic components of a MRI system are the main magnet, gradient coils and a RF transmitter and receiver unit. These components are shown in Figure 2-10 and are described in more detail below.

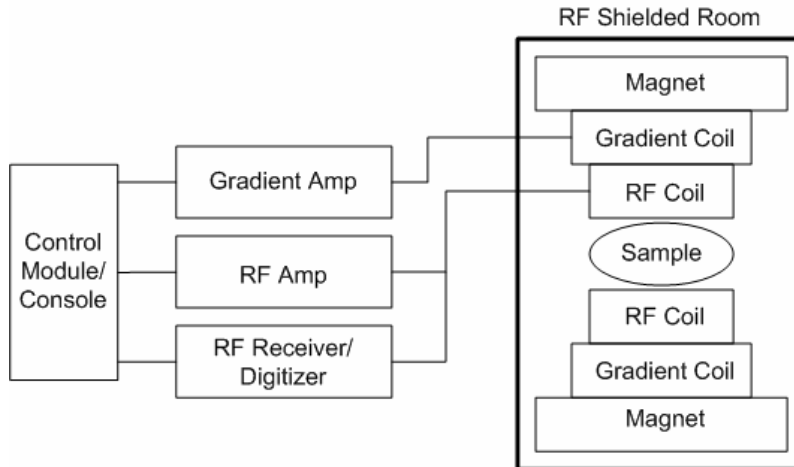


Figure 2-10 - Block diagram of a generic MRI system.

### 2.3.1. Main Magnet

The main magnet is required to generate the strong magnetic field  $B_0$ ; typical values range from 1.5T to 3T for humans. This main field has to be extremely homogeneous over the volume of interest with deviations recorded on the order of a few parts per million (ppm). If homogeneity is not met, spatial distortions in the received image might occur. Additionally, if the main field  $B_0$  is strong, an improved signal to noise ratio (SNR) and resolution will be obtained. This is due to the strength of the main field being directly related to the strength of the MR signals to be received. Additionally, so called shim coils are employed to improve the field uniformity [5].

### 2.3.2. The Gradient Coils

Gradient coils are used to create local variations in the field strength of the main magnet. These variations cause the Larmor frequency of the nuclei to shift. This shifting allows for specific nuclei position to be selected. In order to encode spatial information in the X, Y and Z directions, the gradient coils are then pulsed on and off consistent with the selected pulse sequence employed for a particular imaging modality [5].

### 2.3.3. The RF Transmit and Receive Coils

RF coils stimulate the nuclei creating a signal which is then received. This received signal is further processed to create an image. There are two types of RF coils: transmit and receive coils. The transmit coils are used to create the RF pulse which causes the desired flip angle of the nuclei into the transverse plane. The receiver coils are used to detect the signal that is produced by the atoms relaxing in the transverse plane [10]. A single coil can be used for both the transmit and receive signals. Since the received signal is on the order of one-billionth the power of the transmitted RF pulse, it needs to be amplified.

The preamplifier used to strengthen the received signal is required to meet several requirements. The amplifier must provide a gain that is sufficient enough to detect a signal with a noise figure (NF) on the order of 0.5-0.8 dB. If the NF is too large it will corrupt the received signal resulting in an unclear image. This low NF also allows for subsequent stages in the imaging process to have a much higher NF which in turn lower the enter noise figure of the receiver. The input sensitivity needs to be of a high reflection coefficient (0.90-0.99) which with combination with the cable and matching network, the coil loop itself sees high impedance. This high impedance will then result in blocking current flow in the coils. As explained later in more detail, if the current magnitude is limited, the mutual coupling between multiple RF receive coils is close to zero, thus limiting the crossover distortion. For this thesis, the amplifier will be constructed to have a bandwidth ranging from 100MHz to 500MHz; this will allow the amplifier to be used in multiple field strength systems ranging from 2.35T to 11.7T.

### **3. Preamplifier Design Considerations**

Low noise preamplifiers (LNA) are generically used in an MR scanner to amplify the small received signal obtained by the RF coil. The LNA will not only have to provide adequate gains at low noise levels, but will also be used to eliminate cross coupling between coils. It is essential that the aforementioned preamplifier meets the following requirements: high gain and low noise, stability, and high impedance matching to the coil. It is also important that all specifications are addressed with a small form factor.

#### **3.1. Transistor Selection**

In general, “The design of an RF preamplifier is a step-by-step logical procedure with an exact solution for each problem [1]”. In any RF preamplifier design the transistor selection determines the performance level. For our MRI system, the transistor must meet the following requirements: sufficient gain at low noise levels, stability over frequencies of interest, and linearity over the gain range. The preamplifier designed for this thesis must provide a minimum gain of 30dB, noise level not in excess of 0.8dB, stability over frequencies from 100MHz to 500MHz and an sufficient output 3<sup>rd</sup> order intercept point (OIP3) which measures linearity. The system is also limited to a power supply current budget of 150mA, thus current consumption needed to be considered.

The selection of a suitable transistor is vital in starting the designing process of the preamplifier. With Agilent Technologies providing high performance and quality devices, two transistors were considered, the ATF-541M4 and ATF-551M4. Both are enhancement mode pseudomorphic high electron mobility transistors (PHEMT) in miniature leadless packages. The ATF-541M4 and ATF-551M4 transistors were chosen based on their high linearity performance of 35.8dBm OIP3, and 24.1dBm OIP3

respectively; and a significantly low noise figures of 0.5dB compared to other products on the market. Finally, as discussed below the ATF-551M4 transistor was chosen based on its ability to operate at a lower voltage and current while providing more gain than the ATF-541M4. The ATF-541M4 did have a wider linearity range than the ATF 551M4 but was in excess. Thus, these qualities made the ATF-551M4 the more efficient component.

Enhancement mode PHEMT's provide the added benefit of performing without a negative power supply. The enhancement mode PHEMT's ability to operate without this negative voltage is due to its requirement that the gate be made more positive than the source for all normal operation. In comparison, the traditional depletion mode PHEMT's require the gate to be more negative with respect to the source [8].

### **3.2. Transistor Biasing**

Transistor biasing controls the operating performance of the active device. Different biasing levels can be used to manipulate the maximum gains and minimum noise levels. For the ATF-551M4 transistor, a drain-source biasing of  $V_{ds} = 2.7V$  with a drain-source  $I_{ds}$  current ranging from 15-20mA will provide adequate gain of 21dB and a minimum noise figure (NF) of 0.18dB.

The biasing network provided in Figure 3-1 can be used as a basis in designing the sufficient biasing configuration for the ATF-551M4 transistor. It is important to note that the PNP transistor (Q2) is employed as an active load. Active loading is preferred over a resistive load due to it acting as a low-frequency feedback loop to bias the ATF-551M4. The reasons why active loading was chosen will be described in more detail in Chapter 5.



current flow. Arguably most important, the resistance of  $10K\Omega$  of R5 limits the current flowing to the ATF-551M4 transistor in the presence of high RF drive levels as experienced at the 1dB gain compression point. C5 is then typically  $0.1\mu F$  to provide a low frequency bypass that reduces the effects of noise from Q2 on the ATF-551M4 transistor. Finally C1 and C2 are DC blocking capacitors and L1 and L2 are RF chokes. C3 and C4 are provided to short to ground if any RF passes through the chokes.

Provided below by the Agilent data sheet, Equations (4) through (8) will be used to calculate the values of the remaining resistors which create the desired bias levels.

$$V_E = V_{ds} + (I_{ds} \cdot R4) \quad (4)$$

$$R3 = \frac{V_{DD} - V_E}{I_{ds}} \quad (5)$$

$$V_B = V_E - V_{BE} \quad (6)$$

$$R1 = \frac{V_{DD}}{I_{BB} \cdot \left(1 + \frac{V_{DD} - V_B}{V_B}\right)} \quad (7)$$

$$R2 = \frac{R1(V_{DD} - V_B)}{V_B} \quad (8)$$

Equation (4) calculates the required emitter voltage of the PNP transistor based on the desired  $V_{ds}$  and  $I_{ds}$ . Given this equation a resistance of  $10\Omega$  for R4 results in a calculated emitter voltage  $V_E$  of 2.85V. Using Equation (5), R3 can be calculated to be  $143.33\Omega$  by using a supply voltage  $V_{DD}$  of 5V. Equation (6) calculates the voltage at the base of Q2 based on the assumption that the voltage from the base to emitter is approximately 0.7V. R1 can be calculated from Equation (7) to be  $4.3K\Omega$  and R2 can

be calculated to be  $5.7K\Omega$  with  $I_{BB}$  equal to  $0.5 \times 10^{-3}A$  which is the current flowing through the R1/R2 voltage divider network. These calculated values will comprise the biasing network for the ATF-551M4 transistor. To make the ATF-551M4 transistor stable over the frequencies of interest it may be necessary to make small component value adjustments to the bias network.

### 3.3. Stability

The stability of the transistor is the most important part of a high impedance preamplifier design due to the consideration of operating on the edge of the output stability circle. This operation close to the circle is what makes  $|S_{11}|$  high but less than 1. If operation of the transistor deviates too far from this stability circle the  $|S_{11}|$  would then go down, which is not desired. If proper considerations are not met and  $|S_{11}|$  becomes greater than 1, the preamplifier may become an oscillator. Stability considerations must then be addressed and stability circles can be plotted to determine the stable regions.

Equations (9) and (10), determine the determinant ( $Ds$ ) of the S parameter matrix which allows the calculation of the transistor stability using the Rollett stability factor  $k$  [14].

$$|Ds| = |S_{11}S_{22} - S_{12}S_{21}| \quad (9)$$

$$k = \frac{1 + |Ds|^2 - |S_{11}|^2 - |S_{22}|^2}{2|S_{12}||S_{21}|} \quad (10)$$



Referring to Equation (10) if  $k$  is greater than 1 and  $|D_S|$  is less than 1, the transistor will be unconditionally stable at the operating frequencies. Figure 3-2 depicts unconditionally stability over a frequency range with  $k$  greater than 1.

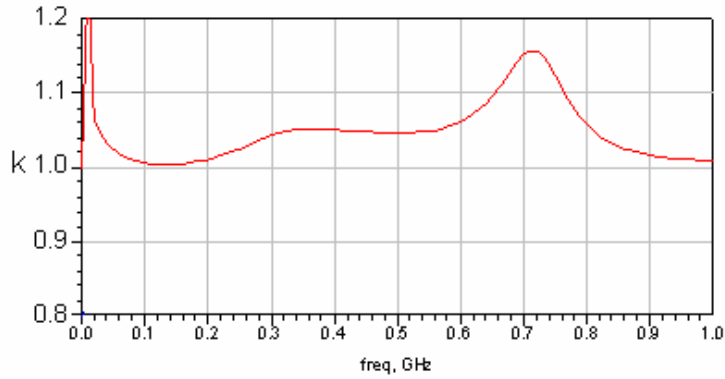


**Figure 3-2 – Unconditional stability check.**

If  $k$  is calculated to be less than 1, the transistor is potentially unstable. Having a  $k$  value of less than one does not imply that the transistor cannot be stabilized. Instead, this may indicate that the source and load impedances must be chosen carefully so that the transistor does not oscillate. If  $k$  is less than 1, input and output stability circles can be graphed to investigate the transistor stability [1].

Equations (11), (12) and (13) make up the input stability circle, with  $r_{s1}$  and  $p_{s1}$  as the center point and radius of the circle, respectively. Here,  $C_1$  is the desired load reflection coefficient for conjugate matching. The asterisk used below is to indicate the application of the complex conjugate [1].

$$C_1 = S_{11} - D_S S_{22}^* \quad (11)$$

$$r_{s1} = \frac{C_1^*}{|S_{11}|^2 - |D_S|^2} \quad (12)$$

$$p_{s1} = \left| \frac{S_{12}S_{21}}{|S_{11}|^2 - |D_S|^2} \right| \quad (13)$$

Equations (14), (15) and (16) make up the output stability circle, with  $r_{s2}$  and  $p_{s2}$  as the center point and radius of the circle, respectively. Again,  $C_2$  is the desired load reflection coefficient for conjugate matching [1].

$$C_2 = S_{22} - D_S S_{11}^* \quad (14)$$

$$r_{s2} = \frac{C_2^*}{|S_{22}|^2 - |D_S|^2} \quad (15)$$

$$p_{s2} = \left| \frac{S_{12}S_{21}}{|S_{22}|^2 - |D_S|^2} \right| \quad (16)$$

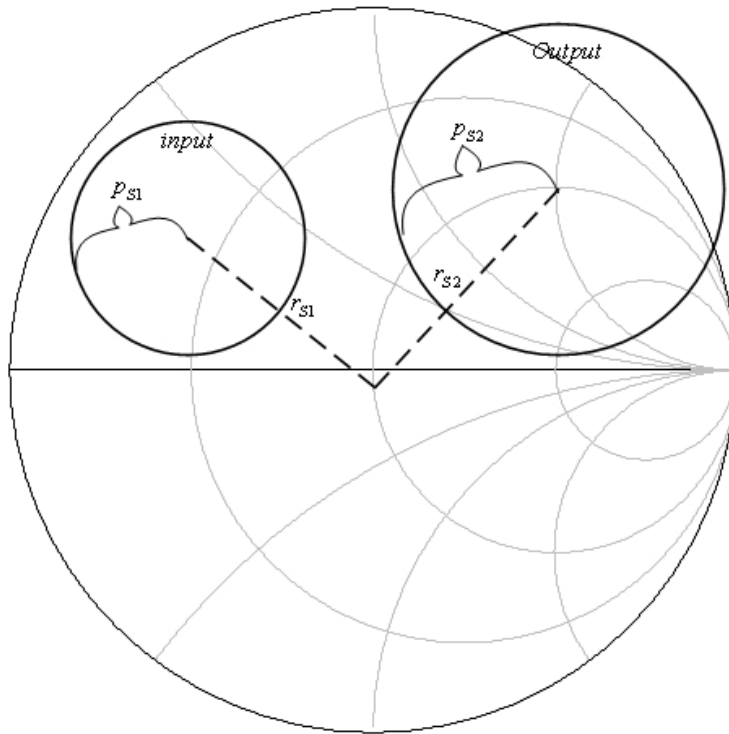


**Figure 3-3 - Example of input and output stability circles.**

After the input and output stability circles have been calculated, circles can be plotted on the Smith Chart, an example of this is shown in Figure 3-3. One now must determine if the inside or outside of the circles represent the stable regions. If  $|S_{11}| < 1$ , the origin is part of the stable region of the input stability circle and if  $|S_{11}| > 1$ , then the origin is part of the unstable region. This concept holds true for the output stability circle but in terms of  $|S_{22}|$  instead of  $|S_{11}|$  [14].

If the system is unconditionally stable and  $S_{11}$  and  $S_{22}$  have magnitudes less than 1, the plotted stability circles would reside entirely outside of the Smith Chart. To obtain stability, impedance matching can be used to move these circles outside of the smith chart.

### **3.4. Impedance Matching**

To achieve maximum power transfer, it is essential to match the impedance of a load to a source. This is accomplished by using a matching network. Matching networks are primarily built with reactive passive components to create a narrowband lossless network or with resistive components to create a wideband lossy network. Matching networks can be designed in multiple configurations such as L networks, T networks, Pi networks, and Low-Q networks. Each configuration is then implemented depending on the quality factor Q and other objectives chosen for matching [1]. Impedance matching will be explained in the preamplifier by bilateral matching with stability corrections, matching with low noise consideration, and by impedance matching to the coil.

### 3.5. Quality Factor Q

A guideline for building matching networks is by the quality factor Q. The Q determines the bandwidth of the matching network. Equation (17) and (18) define the loaded Q in terms of energy or frequency [14]. Note that all Q calculations are using an unloaded Q, it does not taking into account an external impedance.

$$Q = \omega \frac{\text{average\_stored\_energy}}{\text{power\_loss\_per\_cycle}} \Big|_{\omega = \omega_c} = \omega \frac{W_{\text{stored}}}{P_{\text{loss}}} \Big|_{\omega = \omega_c} \quad (17)$$

$$Q = \frac{f_c}{f_U^{3dB} - f_L^{3dB}} \equiv \frac{f_c}{BW^{3dB}} \quad (18)$$

Figure 3-4 illustrates the use of constant unloaded Q circles in the combined Z and Y Smith Chart and demonstrates a matching network with a Q = 1. How these circles are plotted are based on the points where Q is equal to the reactance over the resistance (x/r) for the right side circles and equal to the susceptances over the conductance (b/g) for the left side of the Smith Chart. Note that when matching with the preferred Q, the point of rotation cannot exceed the constant Q circle. If rotation exceeds the chosen Q, the bandwidth requirement will not be met [14].

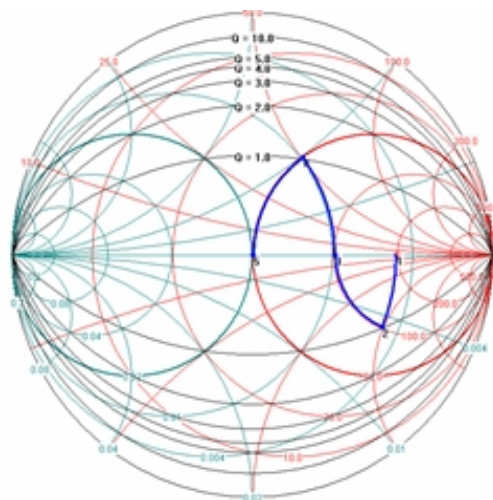


Figure 3-4 - Constant Q circles and matching example of Q=1.

### 3.6. Matching Network Types

The most simple and widely used matching network is the two element L network shown in Figure 3-5. L networks are generally selected based on their low cost and small foot print. A significant disadvantage is the fact that they cannot be built for a desired Q. The selection of the source and load subsequently determines the Q of the matching network. These characteristics of the L networks may lead to a low or high Q circuit behavior.

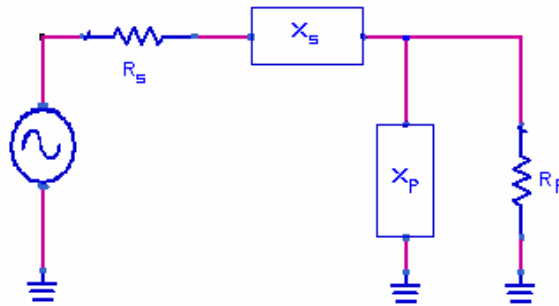


Figure 3-5 - The L Network.

The Q of the L network shown in Figure 3-5 can be calculated by using Equations (19) and (20) based on the external impedance elements  $R_s$  and  $R_p$  [1],

$$Q_s = Q_p = \sqrt{\frac{R_p}{R_s} - 1} \quad (19)$$

$$X_s = Q_s R_s \quad \text{and} \quad X_p = Q_p R_p \quad (20)$$

where, as shown in Figure 3-5:

$R_p$  = the shunt resistance (the load impedance),

$R_s$  = the series resistance (the source impedance),

$X_p$  = the shunt reactance,

$X_s$  = the series reactance.

Note that in the previous example the L networks only consist of a resistive source and load to show the simplicity of matching. If the source and load resistances are complex, the matching network can be adjusted to absorb the inductive or capacitive impedances by prudent placement. Resonance can also be used to “subtract” a complex impedance from another complex impedance. The matching network values  $X_s$  and  $X_p$  can either be capacitive or inductive reactance, but must always be opposite [1].

When  $X_s$  and  $X_p$  are calculated, Equations (21) and (22) are used to calculate the inductance and capacitance values according to

$$L = \frac{X_s}{2\pi \cdot f} \text{ or } L = \frac{X_p}{2\pi \cdot f} \quad (21)$$

$$C = \frac{1}{X_p \cdot 2\pi \cdot f} \text{ or } C = \frac{1}{X_s \cdot 2\pi \cdot f} \quad (22)$$

where  $f$  is the frequency of operation [1].

The L type networks are important due to fact that they provide the foundation of creating more complex networks. The combination of L networks can then produce high and low Q matching networks. For all future networks described, the values of inductance and capacitance are calculated in the same manner as the simple L matching network in which the reactance values are found first.

The three element T and Pi matching networks are very similar to that of the L network, shown in Figure 3-6. The difference between the two lies in the three element network’s ability to control Q. The T and Pi networks can never have a smaller Q than the L network with the same source and load. They can be designed, however, to have a

higher Q. This higher Q results in a narrower bandwidth which might be desirable for a particular system requirement.

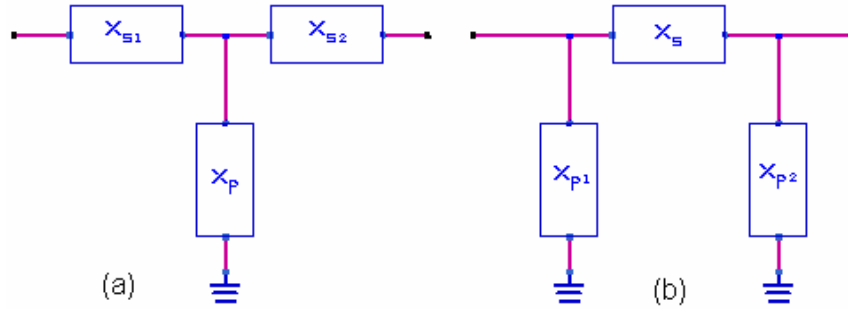


**Figure 3-6 - (a) T Network, (b) Pi Network.**

In designing a matching network with a desired Q for the T and Pi networks Equations (23) and (24) are used, respectively:

$$Q_T = \sqrt{\frac{R_{large}}{R} - 1} \quad (23)$$

$$Q_{Pi} = \sqrt{\frac{R}{R_{small}} - 1} \quad (24)$$

where,

$R_{large}$  = the largest terminating resistance  $R_S$  or  $R_L$ ,

$R_{small}$  = the smallest terminating resistance,

$R$  = the virtual resistance.

When building the T and Pi networks virtual resistors are calculated to meet the preferred Q requirements. Virtual resistors are not actually resistors in the matching network, but are considered as reference resistors to indicate what the first L network is matching to. Figure 3-7 illustrates the use of the virtual resistors, after which the series and parallel components can be simplified to make up the T and Pi networks [1].

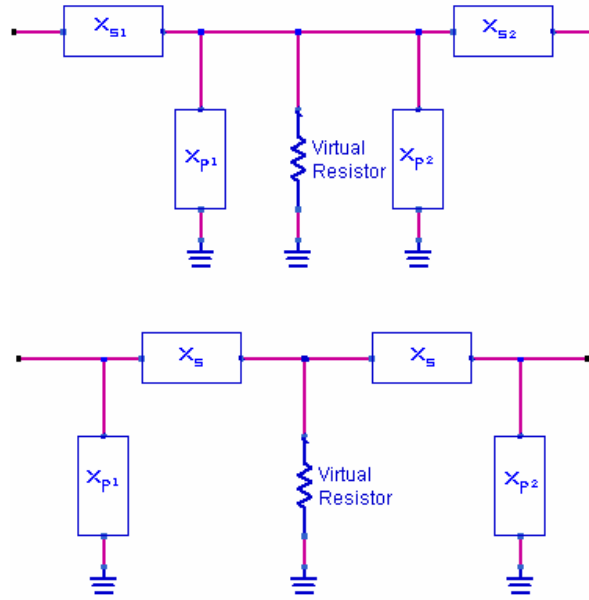


**Figure 3-7 – T (top) and Pi (bottom) networks displaying virtual resistor placement.**

When designing a low-Q network, multiple L-networks are used to acquire the preferred bandwidth for matching. Note that low Q networks cannot be simplified to create T or Pi networks, but instead are a continuous network constructed L networks.

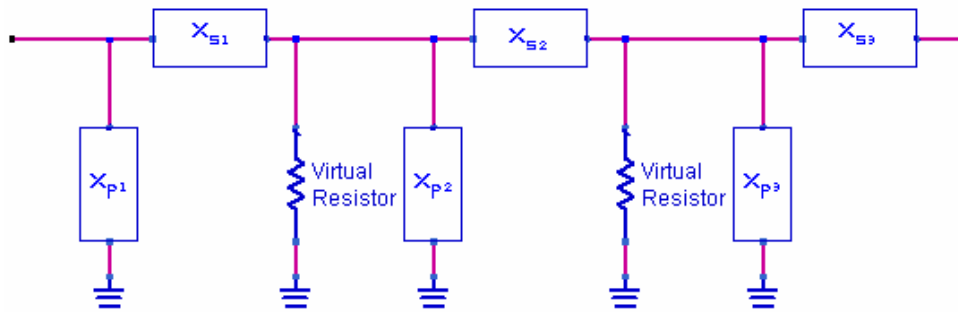


**Figure 3-8 - Low-Q matching Network.**

In designing a matching network with a desired low Q, Equation (25) can be used:

$$Q = \sqrt{\frac{R}{R_{smaller}} - 1} = \sqrt{\frac{R_{larger}}{R} - 1} \quad (25)$$

where,

$R$  = the virtual resistance,

$R_{smaller}$  = the smallest terminating resistance,

$R_{larger}$  = the largest terminating resistance.



If the Q is very low, multiple calculations of virtual resistance will occur, creating a long network. If space is limited a resistive network can be constructed [1].

Resistive matching can be constructed in the same configurations as the L, Pi and T networks. The advantage of using a resistive network is the bandwidth will be extremely large. The disadvantage is that the resistive network is lossy which may cause problems if the transmitted signal is small.

### 3.7. Bilateral Matching

For many practical circuits, matching networks are used to reduce undesired reflections and thus improve power flow. For preamplifier design a technique called bilateral matching is used and is shown below in Figure 3-9. Bilateral design takes into account the feedback of  $S_{12}$ . This is in contrast to the unilateral design which creates an error by setting  $S_{12} = 0$  [14].

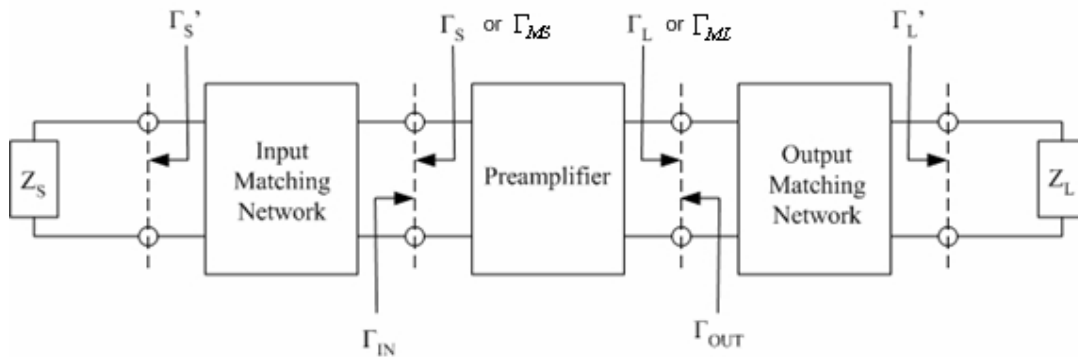


Figure 3-9 - Generic preamplifier system with bilateral matching.

Input and output reflection coefficients can then be calculated from Equations (26) and (27),

$$\Gamma_{MS}^* = S_{11} + \frac{S_{21}S_{12}\Gamma_{ML}}{1 - S_{22}\Gamma_{ML}} \quad (26)$$

$$\Gamma_{ML}^* = S_{22} + \frac{S_{21}S_{12}\Gamma_{MS}}{1 - S_{11}\Gamma_{MS}} \quad (27)$$

which requires a simultaneous conjugate match. Simultaneous matching implies that the matched source and load reflection coefficients  $\Gamma_{MS}$  and  $\Gamma_{ML}$  have to satisfy both coupled equations [14]. The matched source reflection coefficient  $\Gamma_{MS}$  is

$$\Gamma_{MS} = \frac{B_1}{2C_1} - \sqrt{\left(\frac{B_1}{C_1}\right)^2 - 4\frac{C_1^*}{C_1}} \quad (28)$$

where

$$C_1 = S_{11} - S_{22}^*Ds \text{ and } B_1 = 1 - |S_{22}|^2 - |Ds|^2 + |S_{11}|^2 \quad (29)$$

Similarly, the matched load reflection coefficient  $\Gamma_{ML}$  is

$$\Gamma_{ML} = \frac{B_2}{2C_2} - \sqrt{\left(\frac{B_2}{C_2}\right)^2 - 4\frac{C_2^*}{C_2}} \quad (30)$$

where

$$C_2 = S_{22} - S_{11}^*Ds \text{ and } B_2 = 1 - |S_{11}|^2 - |Ds|^2 + |S_{22}|^2 \quad (31)$$

For the load and source reflection coefficients,  $Ds$  is calculated from Equation (9). Finally, the matching networks are used to match the input and output impedances to the conjugate reflection coefficients, respectively.

For the design of the high impedance dual stage preamplifier, bilateral matching will not be used due to the objective of having a high input impedance. In fact the input matching network needs to provide the worst matching possible. This opposite matching is what will create the high input impedance. In addition, the network does need to match an expectable low noise figure. Also note that if bilateral matching was used, it would be extremely difficult to implement due to the wide frequency range of 100MHz to 500MHz.

### 3.8. Low Noise Matching

In many applications, RF amplifier requirements for signal amplification at low noise levels become essential. Unfortunately, designing for low noise levels can sometime compete with stability and gain. As stated by in many books, “a minimum noise performance at maximum gain cannot be obtained.” A method of plotting noise and gain circles can be used to find the minimum noise at a sufficient gain to meet system requirements [14]. All other aspects of noise generation will be described in more detail in Chapter 4. In this section only the basics of noise circles will be explained.

Equations (32) and (33) create noise circles with  $d_{F_k}$  and  $r_{F_k}$  as the center points and radii, respectively, [14].

$$d_{F_k} = \frac{\Gamma_{opt}}{1 + Q_k} \quad (32)$$

$$r_{F_k} = \frac{\sqrt{(1 - |\Gamma_{opt}|^2) Q_k + Q_k^2}}{1 + Q_k} \quad (33)$$

Here  $Q_k$  is a constant which controls the noise level of each circle in the form

$$Q_k = \left| 1 + \Gamma_{opt} \right|^2 \left( \frac{F_k - F_{min}}{4 R_n / Z_0} \right) \quad (34)$$

In Equation (34) the quantities  $F_{min}$ ,  $\Gamma_{opt}$ , and  $R_n/Z_0$  are specifications given by the manufacturer.  $F_{min}$  is the minimum obtainable noise possible for the selected transistor, with  $\Gamma_{opt}$  and  $R_n/Z_0$  as the optimum reflection coefficient and equivalent noise resistance respectively.  $F_k$  determines the radius of the circle. For example, if  $F_k = 0.7dB$  and  $F_{min} = 0.5dB$ , when moving from  $F_{min}$  to the circle of  $F_k = 0.7dB$  the noise would increase from  $0.5dB$  to  $0.7dB$  until the circle is reached.

Gain circles are then plotted with noise circles to determine the optimum point of matching seen in Figure 3-10. Equations (35) and (36) result in gain circles with  $d_{g_1}$  and  $r_{g_1}$  as the center points and radii respectively,

$$d_{g_1} = \frac{g_1 S_{11}^*}{1 - |S_{11}|^2 (1 - g_1)} \quad (35)$$

$$r_{g_1} = \frac{\sqrt{1 - g_1} (1 - |S_{11}|^2)}{1 - |S_{11}|^2 (1 - g_1)} \quad (36)$$

where  $g_1$  is the normalized gain of each circle [14]. Note that if  $g_1 = 1$  this would be maximum gain. For simplicity of plotting gain circles, each equation is derived from the unilateral design approach which neglects the reverse gain.

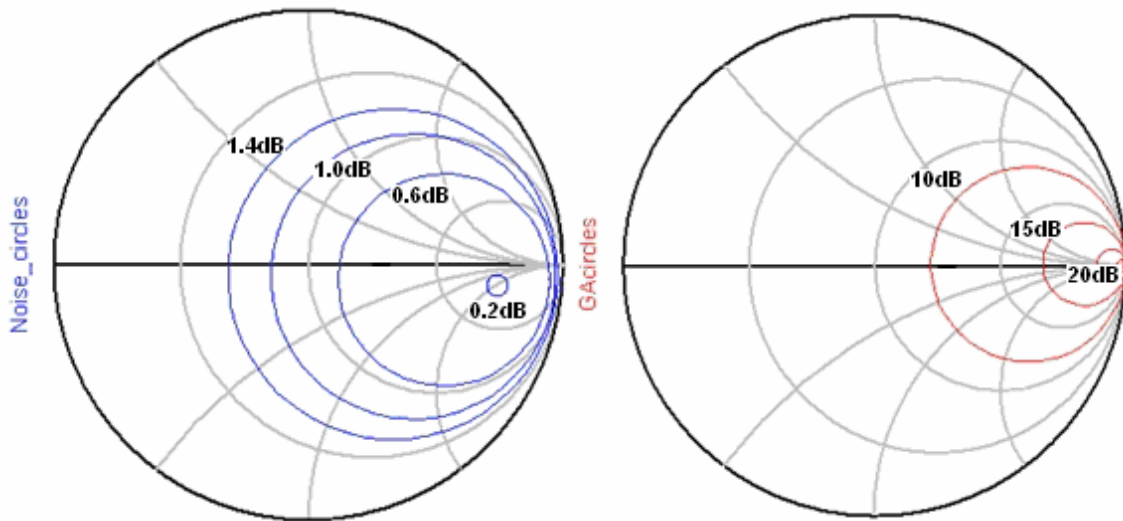


**Figure 3-10 - Constant gain and noise input circles in the Smith Chart.**

Now that gain and noise circles are plotted, an appropriate matching network can be constructed to match the input to the optimal impedance. This optimal impedance will then be matched to the coil.

### 3.9. Matching to the Coil

To ensure maximum power transfer from a small coil resistance to a high impedance preamplifier, a matching configuration is required. Figure 3-11 below shows the required matching design. This design incorporates a phase shifter and impedance transformation network [19].

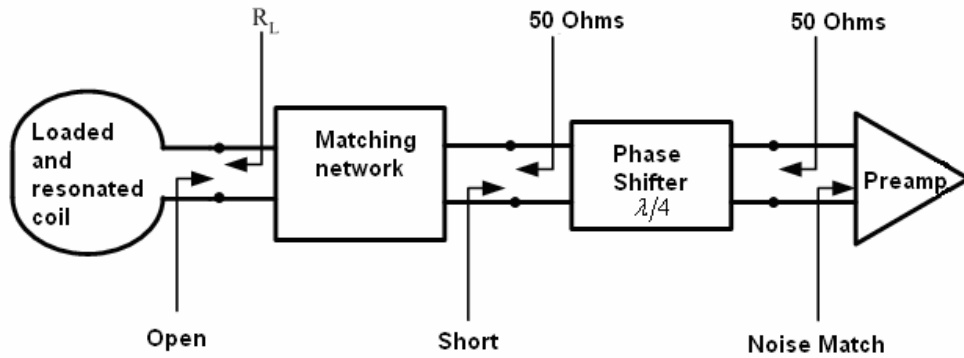


Figure 3-11 - Demonstration of high input reflection preamplifier matching concept.

The phase shifter network is used to transform the high input impedance of the preamplifier to a low impedance (a short) when looking in the direction of the preamplifier. Simultaneously, the phase shifter maintains the  $50\Omega$  match seen from the coil to the high impedance of the preamplifier. A phase shifter is generally a coaxial cable with its S-parameters given by Equation (37),

$$S = \begin{pmatrix} 0 & e^{-j\beta l} \\ e^{-j\beta l} & 0 \end{pmatrix} \quad (37)$$

where  $\beta = \sqrt{LC}$  with  $L$  and  $C$  as the inductance and capacitance per unit length of the cable and  $l$  is the length of the cable.

The impedance transformation network which is a balance-unbalance circuit (balun), seen in Figure 3-11, is then used to transform  $R_L$  into  $50\Omega$  to achieve a low noise matching looking in the direction from the preamplifier to the coil. Simultaneously the

network transforms the phase shifter's low impedance into a high impedance (an open) looking in the direction from the coil to the preamplifier. The importance of this high impedance seen by the coil will be explained in Chapter 4, as well as how it contributes in eliminating crossover distortion between adjacent coils by limiting the current flowing in the coils.

## 4. Noise Considerations

In general, “noise can be defined as any undesired disturbance, be it man-made or natural, in any dynamic electrical or electronic system [1].” Three types of noise sources will be of significance in this thesis; thermal, shot, and flicker noise. These noise types will be discussed in terms of Signal to Noise Ratios (SNR) in the receiver coils and in amplifier design requirements. The analysis presented below will provide both an analytical and an intuitive understanding of the needed performances of MRI equipment.

### 4.1. Thermal, Shot and Flicker Noise

Thermal noise, also known as Johnson noise, is generated by random voltages and currents created from the random motion of charged carriers within a conductor. Due to thermodynamics principles, when the temperature of the conductor of a PHEMT transistor increases, the random motion and velocity of the charged carriers increases [8]. This increase in movement causes an increase in noise voltage which can be calculated by

$$\overline{i_d^2} = 4kT \left( \frac{2}{3} g_m \right) \Delta f \quad (38)$$

where,

$\overline{i_d^2}$  = the noise current from drain to source in A,

$k$  = Boltzmann’s constant ( $1.38 \times 10^{-23}$  J/Kelvin),

$T$  = the absolute temperature in Kelvin ( $^{\circ}C + 273$ ),

$g_m$  = the device transconductance at the operating point in  $1/\Omega$ ,

$\Delta f$  = the bandwidth in Hz.

It is important to note that thermal noise is dependent upon the bandwidth of the system. When obtaining optimum noise performance, the bandwidth is of great

significance as it should never exceed the necessary requirements for the chosen system [12].

Shot noise, also known as Schottky noise, is produced by the random passage of electrons and holes across a potential barrier. “It is often thought that a dc current flow in any semiconductor material is constant at every instant [1].” In reality, however, there are fluctuations in the number of charged carriers that produce random current changes at any given instant. The noise created in a PHEMT transistor by these changes in current can be calculated according to:

$$\overline{i_g^2} = 2qI_G\Delta f \quad (39)$$

where,

$\overline{i_g^2}$  = the noise current at the gate in A,

$q$  = the electron charge ( $1.6 \times 10^{-19}$  C),

$I_G$  = the current applied to the gate in A,

$\Delta f$  = the bandwidth in Hz.

Since the preamplifier is designed with PHEMT transistors, which have dc gate currents of typically less than  $10^{-15}$  A, the addition of shot noise to the total noise budget will be insignificant [8].

Flicker noise, also known as one-over-f noise, is a noise source that has a spectral density that is proportional to  $1/f^n$ , where  $n \approx 1$  [12]. Due to PHEMT transistors conducting current near the surface of the silicon, the surface can act as a trap that captures and releases current carriers. Therefore, flicker noise can be large; it is calculated according to

$$\overline{i_d^2} = K \frac{I_D^a}{f} \Delta f \quad (40)$$

where,



$\overline{i_d^2}$  = the noise current from drain to source in A,  
 $I_D$  = the drain bias current in A,  
 $K$  = the constant for the given device,  
 $a$  = a constant between 0.5 and 2,  
 $\Delta f$  = the bandwidth in Hz.

The contributions of thermal and flicker noise constitute the entire noise budget generated in the preamplifier system which is only valid at low frequencies. Due to the preamplifier being designed to operate from 100MHz to 500MHz and PHEMT transistors having very small K values on the of  $10^{-25}$ , the contribution of flicker noise is insignificant. Thus, only thermal noise will be considered in all subsequent noise calculations [8].

## 4.2. Noise Figure and SNR

The noise of a system can be expressed in two different ways: either as noise figure (NF) or as signal to noise ratio (SNR). NF is the measurement of noise generated in active devices. SNR, on the other hand, is the measurement of noise ratios between the magnitudes of the transmitted signals against the magnitude of the background noise. Both NF and SNR are often expressed in terms of the logarithmic decibel scale (dB) as many signals have a wide dynamic range.

The NF is frequently used to measure quality of an amplifier and can be calculated by

$$NF = 10 \cdot \log_{10} F \quad (41)$$

where F is the noise factor. The noise factor can be calculated by

$$F = F_{\min} + \frac{4R_n}{Z_0} \frac{|\Gamma_S - \Gamma_{opt}|^2}{(1 - |\Gamma_S|^2)(1 + |\Gamma_{opt}|^2)} \quad (42)$$

Here quantities  $F_{\min}$ ,  $\Gamma_{opt}$ , and  $R_n/Z_0$  are specifications given by the manufacturer of the transistor. Again,  $F_{\min}$  is the minimum obtainable noise possible for the selected transistor, with  $\Gamma_{opt}$  and  $R_n/Z_0$  as the optimum reflection coefficient and equivalent noise resistance, respectively. This noise factor can then be expressed as the ratio of output noise power ( $P_{no}$ ) to input power ( $P_{ni}$ ):

$$F = \frac{P_{no}}{P_{ni}} \quad (43)$$

SNR is closely related to the concept of dynamic range. Dynamic range is the measurement of the ratio between noise and the greatest un-distorted signal in a transmission channel [15]. The SNR is generically defined as

$$SNR = 10 \cdot \log_{10} \left( \frac{P_{av}}{P_n} \right) \quad (44)$$

Equation (44) has  $P_{av}$  as the average power, and  $P_n$  as the noise power generated by the system. A signal that is clearly readable will have a large, positive SNR value. If the SNR value is small or approaching zero, the resulting signal will be unclear displaying evidence of the noise level greatly competing with the desired signal.

### **4.3. SNR in a Single Coil**

The SNR of a single coil system will be explained initially in order to examine the SNR of an array of coils. With the noise produced in a MRI system being generally dominated by thermal noise as explained earlier, the SNR of a coil can be calculated by using Equation (44). The time-average power  $P_{av}$  of a coil is defined as:

$$P_{av} = \frac{V_p^2}{2R_L} \quad (45)$$

where  $V_p$  is the peak voltage produced by the induced pulse and  $R_L$  is the coil resistance at resonance. The noise power  $P_n$  in the coil can be derived from the thermal equation expressed in terms of a MOS transistor as

$$P_n = \overline{i_d^2} R_L = 4kT \left( \frac{2}{3} g_m \right) \Delta f R_L = 4kT \left( \frac{1}{R_L} \right) \Delta f R_L = 4kT \Delta f \quad (46)$$

To obtain the SNR of a single coil, Equations (45) and (46) are then inserted into Equation (44), yielding

$$SNR = 10 \cdot \log_{10} \left( \frac{V_p^2}{2R_L \cdot 4kT \Delta f} \right) = 10 \cdot \log_{10} \left( \frac{V_p^2}{8R_L kT \Delta f} \right) \quad (47)$$

The resulting Equation (47) will then be the basis for subsequent SNR computations for single coil systems.

#### **4.4. SNR of an Array of Coils**

When using a single MRI coil, the receiver may not be able to cover the entire region of interest; in such cases the field of view (FOV) will be small. To increase the FOV an array of coils can be implemented, seen in Figure 4-1. Note that each coil has its own preamplifier and the benefits of this arrangement will be described later when discussing switched versus parallel acquisition arrays.

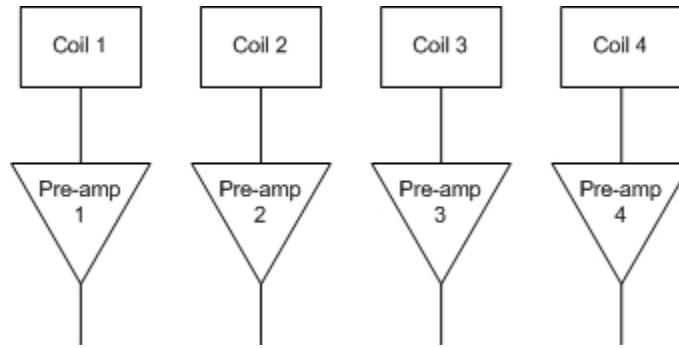


**Figure 4-1 - A linear array of four coils.**

In addition to the internally generated thermal noise that is inherent in any system, the SNR will also contain noise from the coupling of neighboring coils. This additional noise coupling must be minimized in order to obtain a reasonable SNR value.

Coupling is the transfer of portion of a signal from one coil to another as a result of mutual inductance  $M$  that exists between the coils. This event can be seen in Figure 4-2 shown below. At this point two coils will be used to demonstrate effective methods for reducing coupling.

To investigate coupling, each coil is modeled by its distributed equivalences of inductors  $L_C$ , capacitors  $C_C$  and resistors  $R_1$  and  $R_2$ . When resonance occurs, the capacitance and inductance of each coil cancels each other out resulting in a real impedance. This resistance, in addition to the coupling effect will then be used in the thermal equation to calculate the noise of a coupled coil [17].

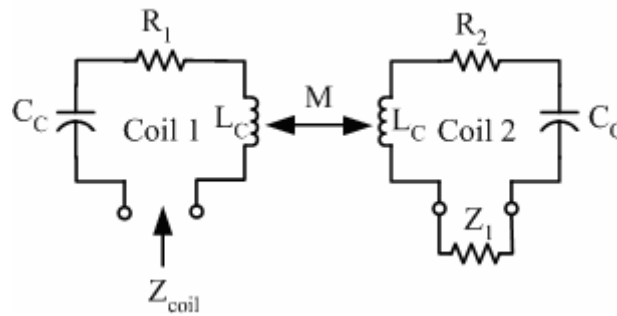


**Figure 4-2 - Inductive coupling between two coils.**

When looking into coil 1, the impedance  $Z_{coil}$  under resonance is equal to  $R_1$  if coil 2 does not exist. If the coupling of coil 2 is considered,  $Z_{coil}$  will no longer be equal to  $R_1$ . In solving for the coupling of coil 1 due to coil 2, two Kirchoff's voltage loops with mutual inductance  $M$  are created in accordance with Figure 4-2 as follows,

$$-Z_{coil}i_1 + \frac{1}{j\omega C_c}i_1 + R_1i_1 + j\omega L_c i_1 - Mi_2 = 0 \quad (48)$$

$$Z_1i_2 + \frac{1}{j\omega C_c}i_2 + R_2i_2 + j\omega L_c i_2 - Mi_1 = 0 \quad (49)$$

where  $i_1$  and  $i_2$  are the currents flowing in coil 1 and coil 2, respectively. Next, Equation (49) is solved for  $i_2$  and inserted into Equation (48) to solve for  $Z_{coil}i_1$

$$Z_{coil}i_1 = R_1i_1 + \frac{1}{j\omega C_c}i_1 + j\omega L_c i_1 + M \left( \frac{Mi_1}{Z_1 + R_2 + j\omega L_c + \frac{1}{j\omega C_c}} \right) \quad (50)$$

As stated previously, when resonance occurs the capacitive and inductive reactances of each coil cancels each other out resulting in a real impedance. When dividing by  $i_1$  and taking into account resonance, Equation (50) simplifying to

$$Z_{coil} = R_1 + \frac{M^2}{R_2 + Z_1} \quad (51)$$

where  $Z_1$  is the impedance seen by coil 2, typically the impedance of the connected preamplifier. The SNR of coil 1, which includes coupled noise from coil 2, can then be calculated as

$$SNR = \frac{1}{8} \frac{V_p^2}{Z_{coil} kT\Delta f} = \frac{1}{8} \frac{V_p^2}{R_1 kT\Delta f + kT\Delta f \left( \frac{M^2}{R_2 + Z_1} \right)} \quad (52)$$

It is important to note that the second term in the denominator of Equation (52) represents the noise power of the coupling between the coils. As  $Z_1$  grows larger, the second term approaches zero. This increase in  $Z_1$  causes the SNR of the two coils to approach the SNR of a single coil. From another perspective one can observe that as  $Z_1$  is increased, the current decreases causing a reduction in the coupling effect in coil 1. After decoupling of coil 2 from coil 1, one can then repeat the process by reducing the current in coil 1 in an effort to decouple coil 1 from 2. As described in Chapter 3, the high impedance of the preamplifier is then matched to the coil.

#### 4.5. Switched Versus Parallel Acquisition Arrays

Phased array systems are used to improve SNR without limiting the FOV. There are two classes of systems: switchable coil arrays and parallel acquisition coil arrays, each shown below in Figure 4-3 (a) and (b), respectively.

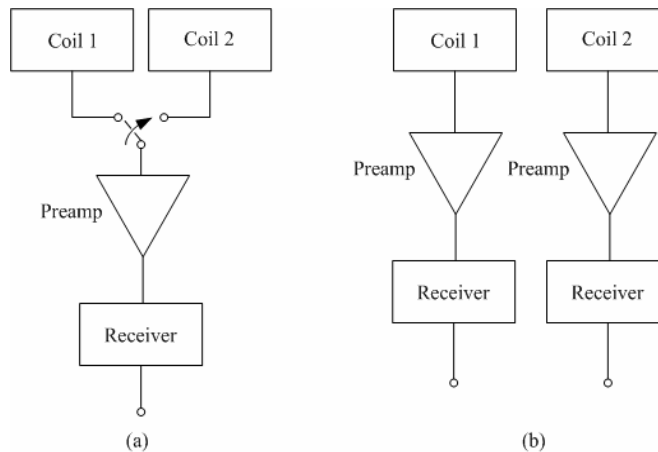


Figure 4-3 - (a) Switchable Array, (b) parallel Acquisition Array

A switchable coil array operates in the same manner as a single coil system, which has only one receiver. The advantage of a switchable coil array is related to the fact that the user can select the optimal coil configuration for examining the area of interest and a single data set will be collected from that coil [29]. A switchable coil array system can inexpensively be added to an existing single coil system since only one receiver preamplifier is required.

In a parallel acquisition array, the coils operate simultaneously and independently collecting data for each coil's FOV. This method is more expensive due to the cost of additional receivers. It also poses a technical challenge of reducing the coupling between coils. The solution to this decoupling issue is the design of the high input impedance preamplifier which is the goal of this thesis.

#### **4.6. Noise Figure of an Amplifier**

When an amplifier is designed with multiple stages, the NF of each stage contributes to the total noise. In each stage the noise factor can be calculated in the same manner as in Equation (42).

In analyzing and calculating the noise figure of a cascaded amplifier, Equation (53) can be used

$$F_{total} = F_1 + \frac{F_2 - 1}{G_1} + \frac{F_3 - 1}{G_1 G_2} + \frac{F_4 - 1}{G_1 G_2 G_3} \dots \dots \quad (53)$$

$$NF_{total} = 10 \cdot \log_{10} F_{total}$$

where  $F_n$  ( $n = 1,2,3\dots$ ) is the noise factor of each stage and  $G_n$  is the numerical gain of each stage (not in dB). Figure 4-4 gives an example of a dual stage amplifier with NF and gain for each stage, respectively.

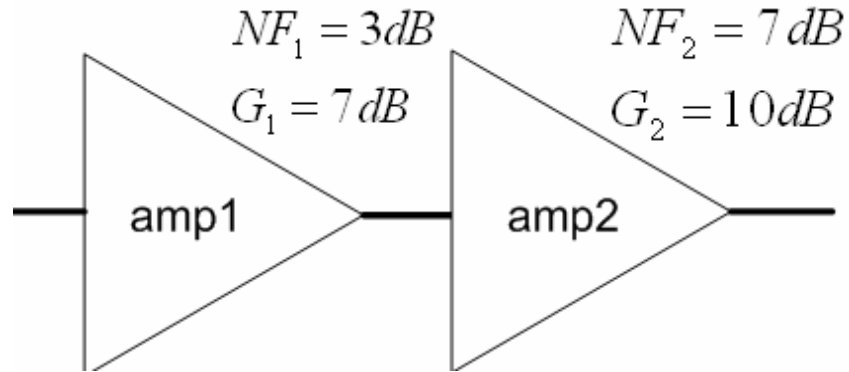


**Figure 4-4 - Example of a dual stage amplifier.**

In calculating the overall NF of the system, the first step is to convert the given noise figures and gains of each stage into numerical ratios. This would yield  $F_1 = 2$ ,  $F_2 = 5$ ,  $G_1 = 5$ , and  $G_2 = 10$  which would then be inserted into Equation (53) to produce Equation (54):

$$F_{total} = 2 + \frac{5-1}{5} = 2.8 \quad (54)$$

or as a total noise figure

$$NF_{total} = 10 \cdot \log_{10} 2.8 = 4.47dB \quad (55)$$



## 5. Single Stage Preamplifier Design

Prior to designing a dual stage preamplifier, a single stage demonstration (demo) board with different biasing configurations was considered. To ensure the most efficient design using the ATF-551M4 transistor, two biasing networks were investigated. A resistive network was considered which consists of a simple voltage divider feedback and an active network which consists of a PNP transistor feedback. The chosen active biasing network is used in the dual stage preamplifier design as mentioned in Chapter 3. There are a number of reasons why this biasing network was chosen. Through the simulation and measured results of the demo boards this will become apparent.

### 5.1. The Demonstration Boards

Demo board 1 shown in Figure 5-1 was simulated and built to investigate the performance of the ATF-551M4 transistor with resistive biasing. As seen in Figure 5-1, R1 establishes the  $V_{ds}$  and  $I_{ds}$  requirements to operate the ATF-551M4 transistor at 2.7V and 15mA respectively.

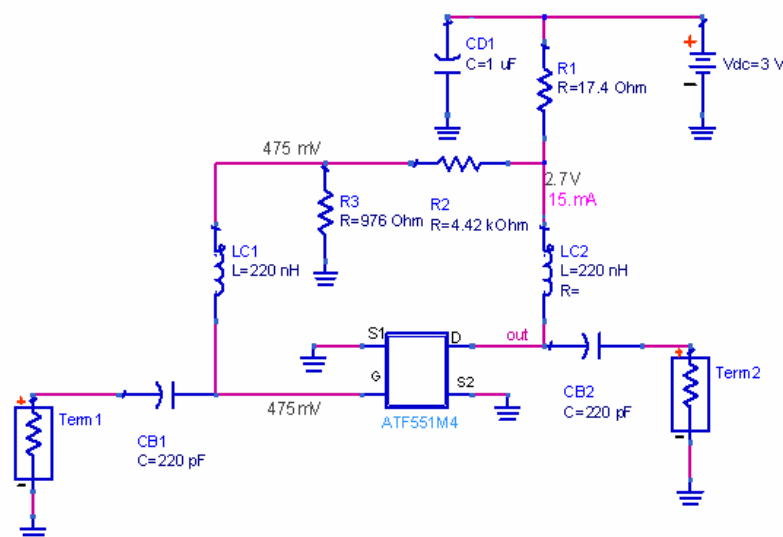


Figure 5-1 – Resistive biasing of ATF-551M4 transistor (Demo Board 1).

In Figure 5-1, R2 and R3 produce a voltage divider feedback which provides the input bias voltage of approximately 0.47 to 0.49V. LC1 and LC2 are used as RF chokes and CB1 and CB2 are used as DC blocks. Lastly, CD1 is used to help reduce noise that may be generated from the DC source.

Demo board 2 shown in Figure 5-2 below consists of the same active biasing circuit described in Chapter 3.

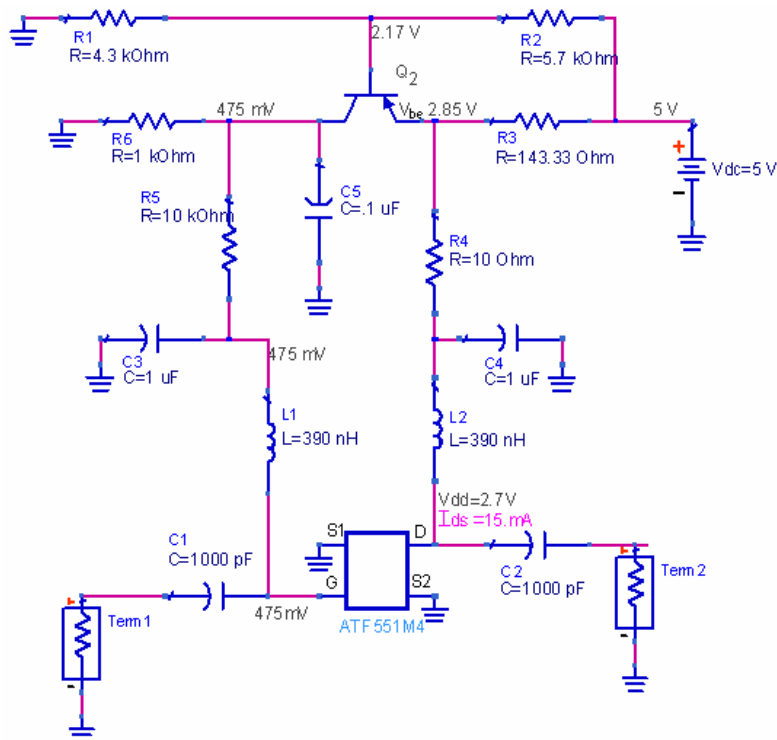


Figure 5-2 - Active biasing of ATF-551M4 transistor (Demo Board 2).

With a deeper understanding of how these demo boards were designed, the simulations and measured results can be investigated in greater detail. The key results of importance within this section are those which support or refute the decision to use a certain biasing network. All measured data obtained from the demo boards will be summarized in Appendix A.

## 5.2. ADS Simulations of Demo boards

To simulate the design of the demo boards and the dual stage preamplifier a simulation tool called Advanced Design System (ADS) designed by Agilent will be used. A comparison of the simulated results between the two biasing networks concludes that the ATF-551M4 transistor allows for best performance and meets the goals of this thesis.

First, we note that the demo boards were not designed to be unconditionally stable. In referring to Figure 5-3, the demo boards are stable for testing due to the input and output impedances being  $50\Omega$  which is the middle of the Smith Chart. For the dual stage preamplifier design, unconditional stability will be considered due to the fact that it is unknown exactly what impedance the preamplifier will see when used in the MRI process.

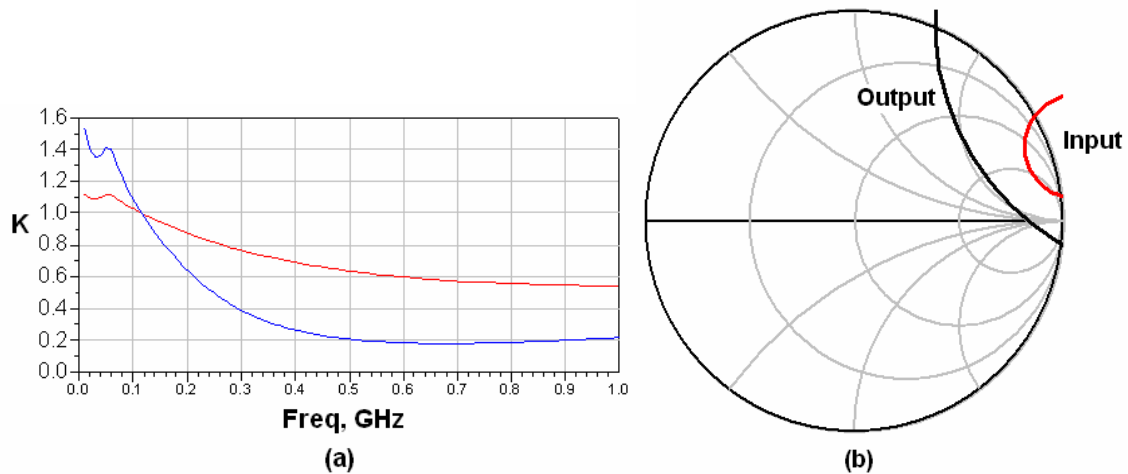


Figure 5-3 - (a) Stability plotted over frequency,  
(b) Smith Chart plot of stability for input and out Impedances.

The noise figures of the resistive and active biased demo boards are shown in Figure 5-4 and Figure 5-5, respectively. A comparison of the two networks shows the active biasing board to have an approximate NF of  $0.4dB$  which is  $0.2dB$  lower than that of the resistive biasing board. The minimum NF of the active biased board is also much lower

than that of the resistive, implying that in combination of a matching network a better noise figure can be obtained.

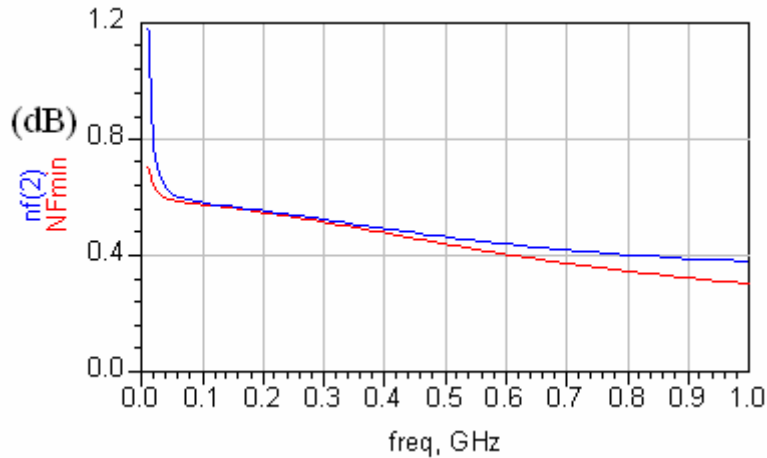


Figure 5-4 – The simulated NF of demo board 1.

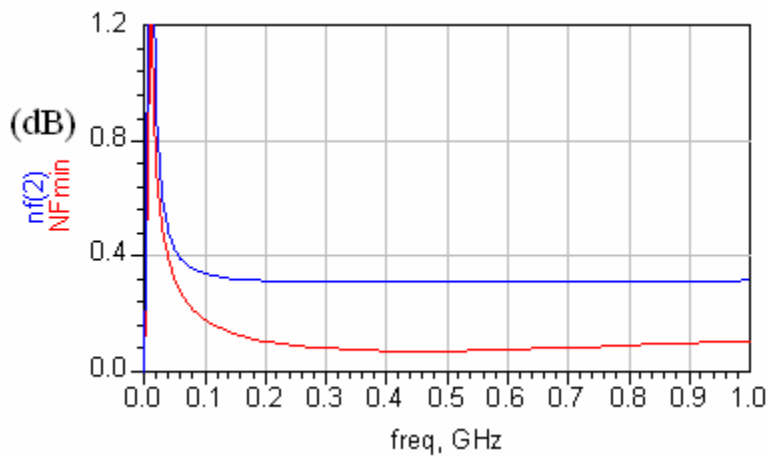


Figure 5-5 - The simulated NF of demo board 2.

Figure 5-6 and Figure 5-7 display the forward gain  $S_{21}$  in dB of the resistive and active biased boards, respectively. Note that the resistive biased board provides more gain than that of the active biased board. This is of no consequence; however, as the future design of building a dual stage preamplifier with active biasing will meet the minimum requirement of 30dB. All things considered the active biasing board with its low NF value seems to be the best choice to meet the goals of this thesis.

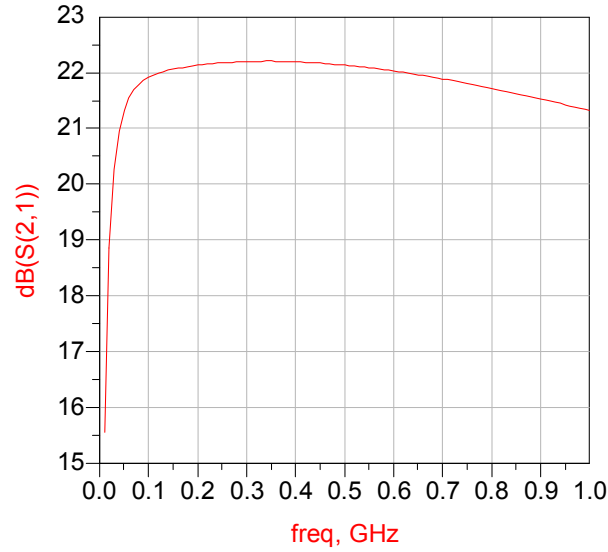


Figure 5-6 – Simulated gain of demo board 1.

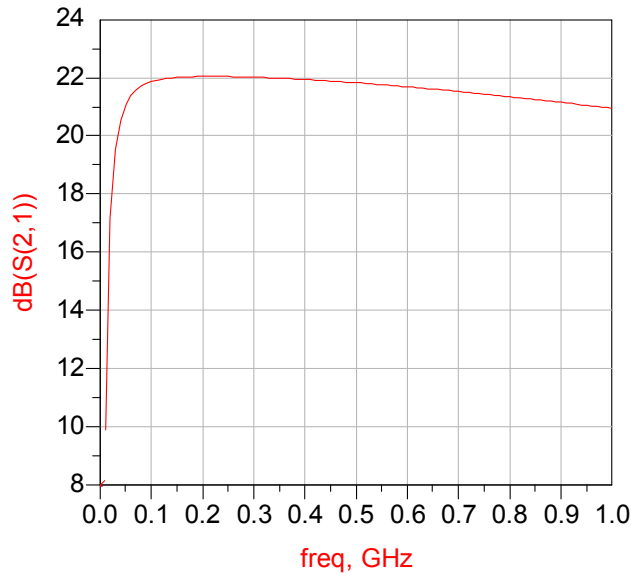
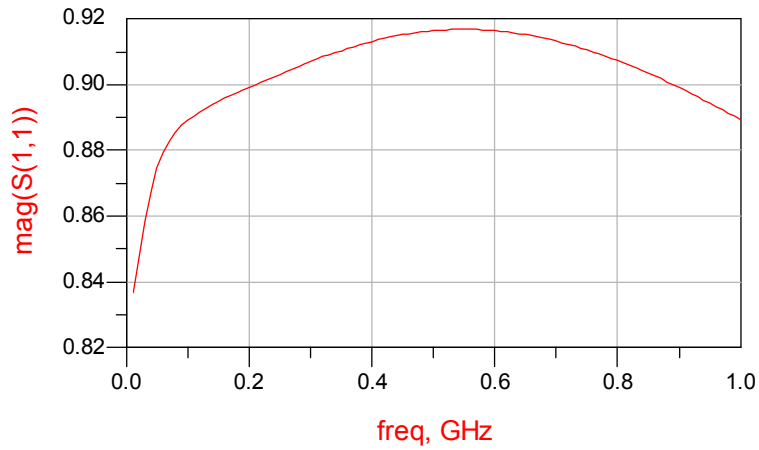
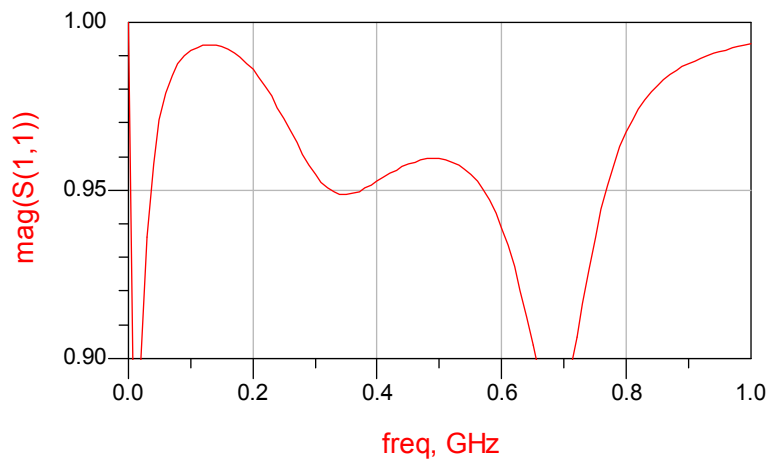


Figure 5-7 – Simulated gain of demo board 2.

Figure 5-8 and Figure 5-9 display the input reflection coefficient  $S_{11}$  of both the resistive and active biased boards. Examining these responses, it can be concluded that the input reflection coefficient of the active biased board is a factor of 0.03 to 0.05 higher over the desired bandwidth. This difference is small, but can dramatically change the performance of the decoupling of coils, thus leading us to conclude that the active biased board is the better choice.



**Figure 5-8 – Simulated  $S_{11}$  of demo board 1.**



**Figure 5-9 - Simulated  $S_{11}$  of demo board 2.**

The numerous simulations provide ample evidence that the active biasing design would provide the best performance required to obtain the goals of this thesis. It is important, however, to investigate the tested results of the demo boards before a final decision is made.

### 5.3. Test Results of Demo Boards

Both the active and resistive demo boards were built and tested to verify the simulated performance. The resistive biased board seen in Figure 5-10 (a) was provided by Agilent as a test board. The active biasing board in Figure 5-10 (b) is the dual stage board designed for this thesis, but with only one stage being used. All data measured and recorded was collected from two Agilent Technology systems located at Analog Devices in Wilmington, Mass.

The Agilent E8357A PNA series network analyzer which has a range of 300 KHz to 6 GHz, and the Agilent N4416A S-parameter test set were used to collect all S-parameter values. All noise measurements were performed in a noise test room using the Agilent N8973A NFA series Noise Figure Analyzer which has a range of 10 MHz to 3 GHz. Both systems then exported all collected data into Excel sheets.

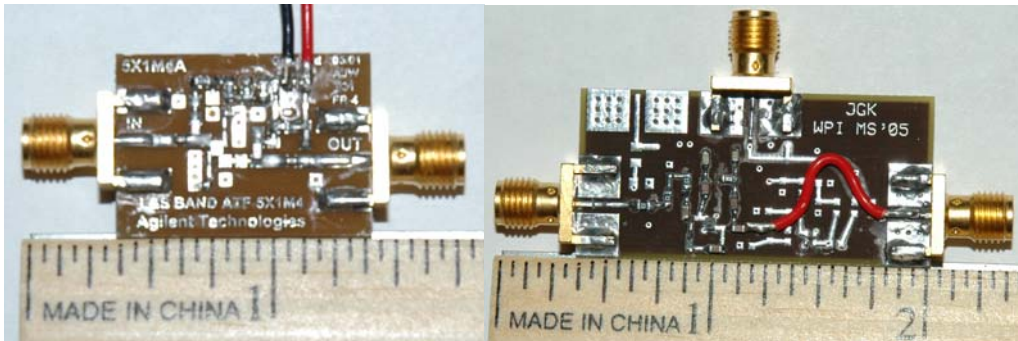


Figure 5-10 – (a) Constructed demo board 1, (b) constructed demo board 2.

Figure 5-11 and Figure 5-12 are the measured noise figures of the resistive and active biased boards, respectively. Upon careful investigation, the NF of the active biased board is much lower than that of the resistive biased board, thus agreeing with the simulated ADS results.

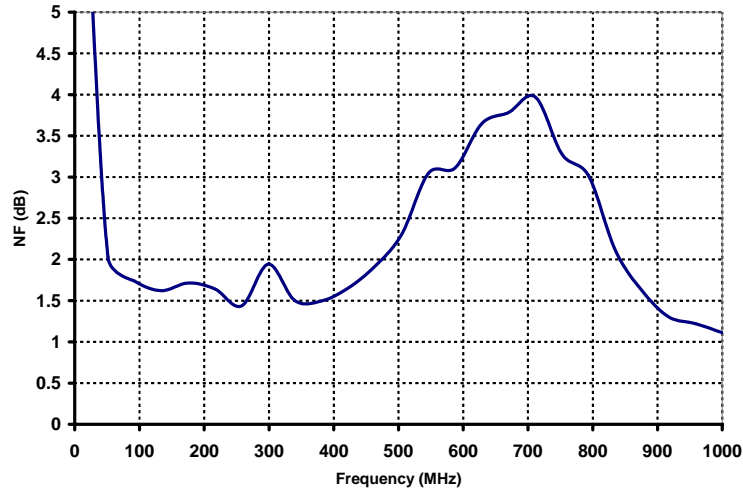


Figure 5-11 – Measured NF of demo board 1.

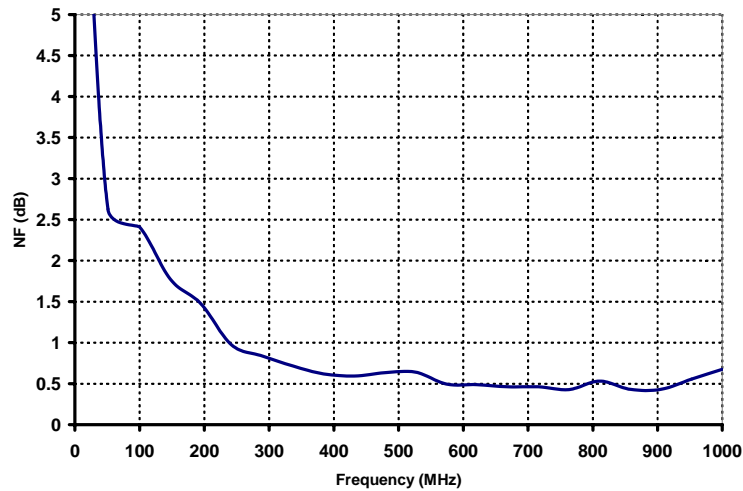
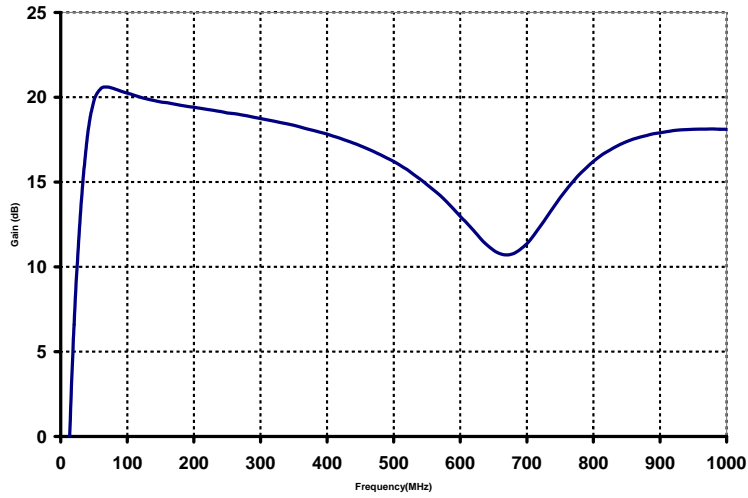


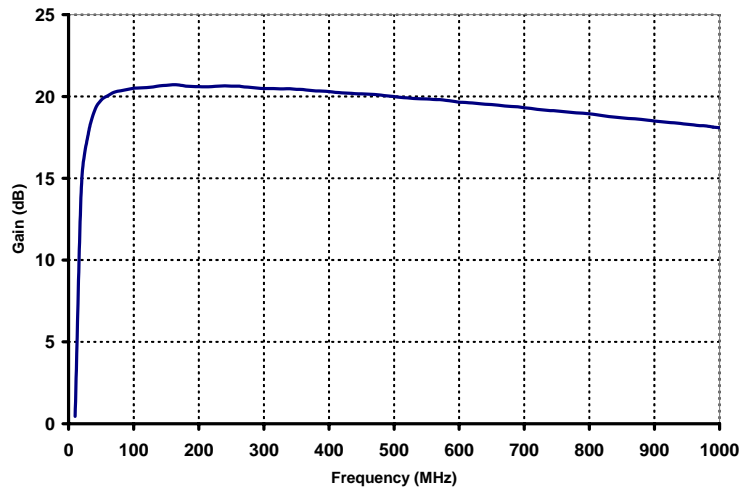
Figure 5-12 – Measured NF of demo board 2.

Figure 5-13 and Figure 5-14 are the measured forward gain  $S_{21}$  in dB of the resistive and active biased boards, respectively. When investigating these measured results, the active biased board has a higher gain over the desired bandwidth than the resistive biased board. This difference in gain might be due to the slight difference in the resistor values which set up the biasing network.





**Figure 5-13 – Measured  $S_{21}$  gain of demo board 1.**



**Figure 5-14 – Measured  $S_{21}$  gain of demo board 2.**

Figure 5-15 and Figure 5-16 are the measured resistive and active biased boards, respectively. Again, these two measured results agree with the simulated results adding more evidence that the active biased board is the more appropriate choice.

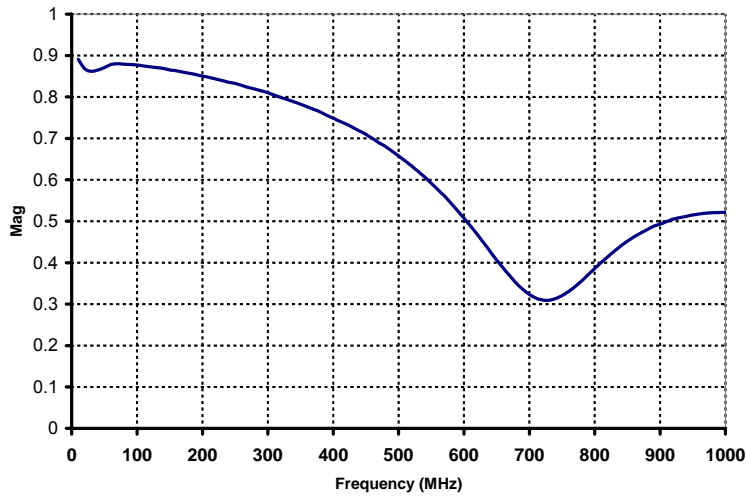


Figure 5-15 – Measured  $S_{11}$  of demo board 1.

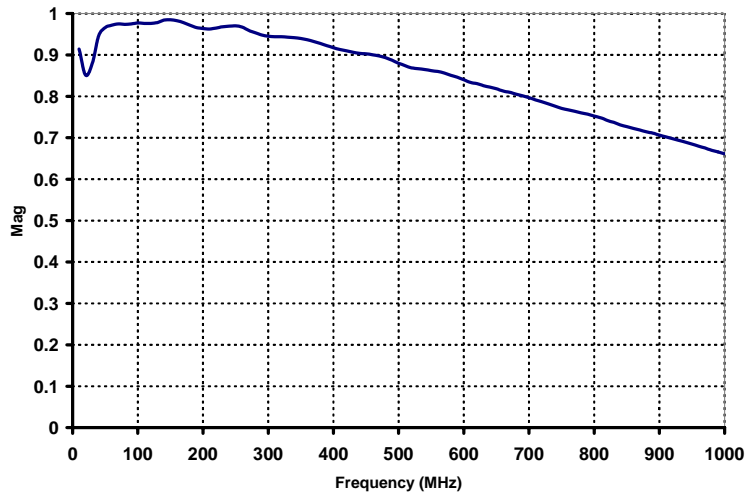


Figure 5-16 – Measured  $S_{11}$  of demo board 2.

After viewing the simulated and measure results and comparing the resistive and active biased boards, it can be concluded that that active biasing is a better choice for the dual stage design. With the active biasing board the input reflection coefficient is higher, the gain is sufficient and the NF is much lower than that of the resistive board.

## 6. Dual stage Preamplifier Design

The completion of two demo boards allowed us to investigate the performance of the ATF-551M4 transistor under different biasing configurations. The biasing configuration proven most effective will be incorporated into a dual stage preamplifier in order to meet the requirements of this thesis. The design of the dual stage preamplifier was simplified by designing and testing sections of the preamplifier separately. A step by step process was then implemented to connect and test one section at a time until the entire preamplifier was assembled. This design process is outlined below.

### 6.1. Design and Simulation

Experience proves that designing a preamplifier in its entirety is not advisable as it makes the debugging process quite complicated. For this reason the first stage of the preamplifier will be investigated initially and only upon proven success will the second stage be connected and examined. To simplify the figures illustrating this design process, block diagrams will be used to represent the biasing networks of the first and second stages.

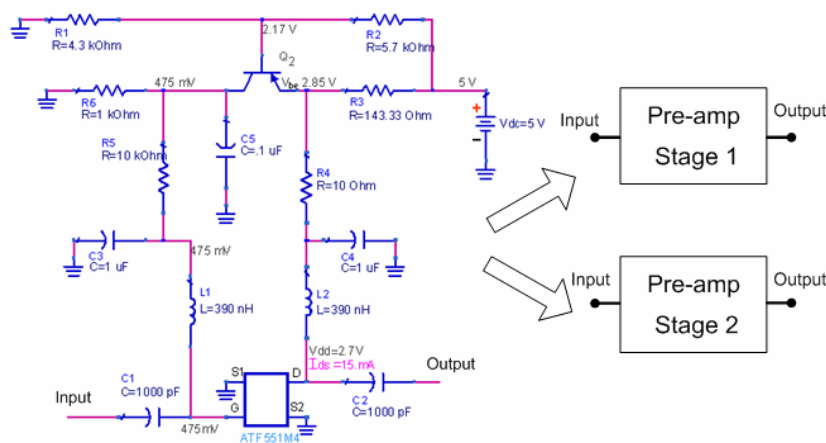


Figure 6-1 - Equivalent block diagram of first stage and second stage.

The first major factor to consider when designing the first stage is unconditional stability, as it determines the ability of the preamplifier to work successfully under all source and termination loads. If the first stage of the preamplifier proves to be unconditionally stable the second stage should also prove stable. For this reason only stability circles of the first stage will be investigated. To investigate this stability a program was written in MATLAB to plot the input and output stability circles shown in Figure 6-2. The code is displayed in Appendix C.

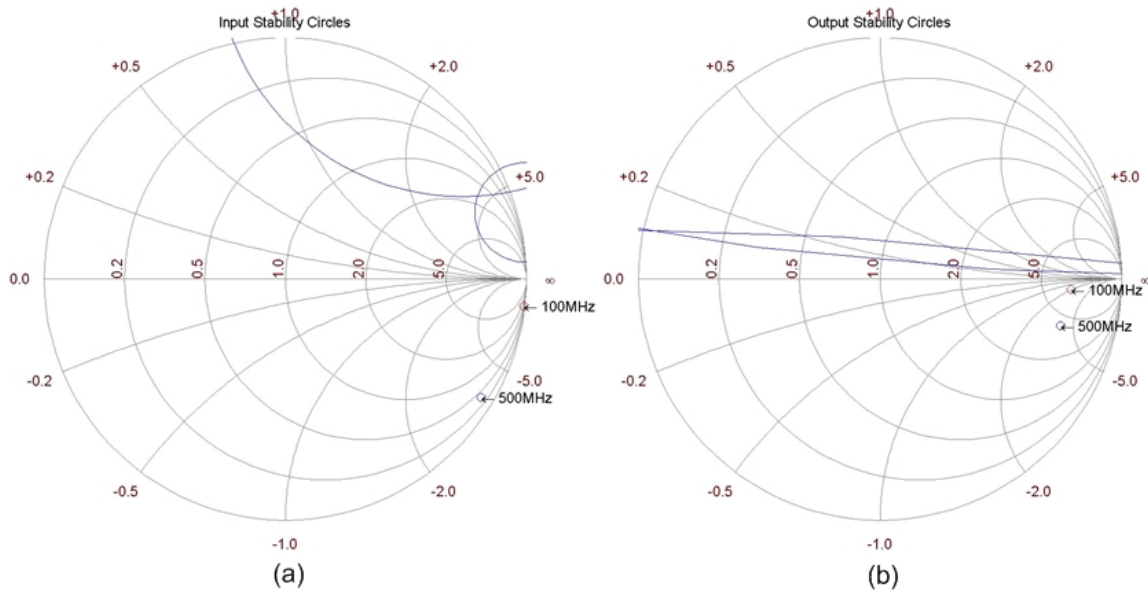
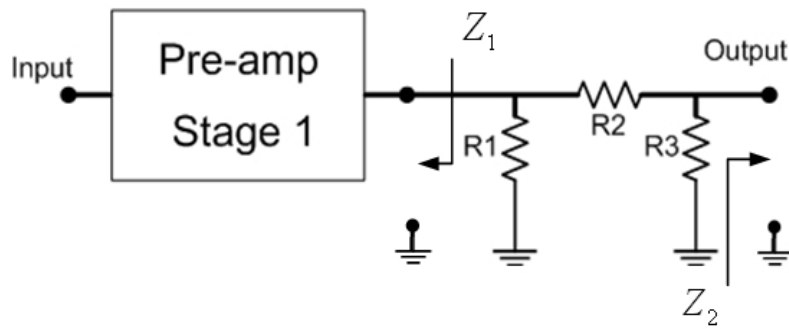


Figure 6-2 - (a) Input stability circles, (b) output stability circles.

Input and output circles were plotted at 100MHz and 500 MHz to illustrate the limiting frequencies in the preamplifiers frequency range. To ensure the first stage is unconditionally stable, both of the circles in the input and output stability plots must reside entirely outside of the Smith Chart. We refer to the Rollett stability factor  $k$ , explained previously, and restated in Equation (56)

$$k = \frac{1 + |D_S|^2 - |S_{11}|^2 - |S_{22}|^2}{2|S_{12}||S_{21}|} \quad (56)$$

when analyzing stability of the active device. If the overall gain  $S_{21}$  is decreased, and there is matching on the output ( $S_{22} = 0$ ), then the stability factor  $k$  can become greater than 1 which would indicate unconditional stability. This unconditional stability can be accomplished by the application of an attenuator on the output of the first stage as seen in Figure 6-3.



**Figure 6-3 - Pi attenuator deployment to create unconditional stability.**

When incorporating this attenuation created by the pi attenuator into the MATLAB code, an attenuation of 11.8dB successfully pushes all input and output circles outside of the Smith Chart seen in Figure 6-4.

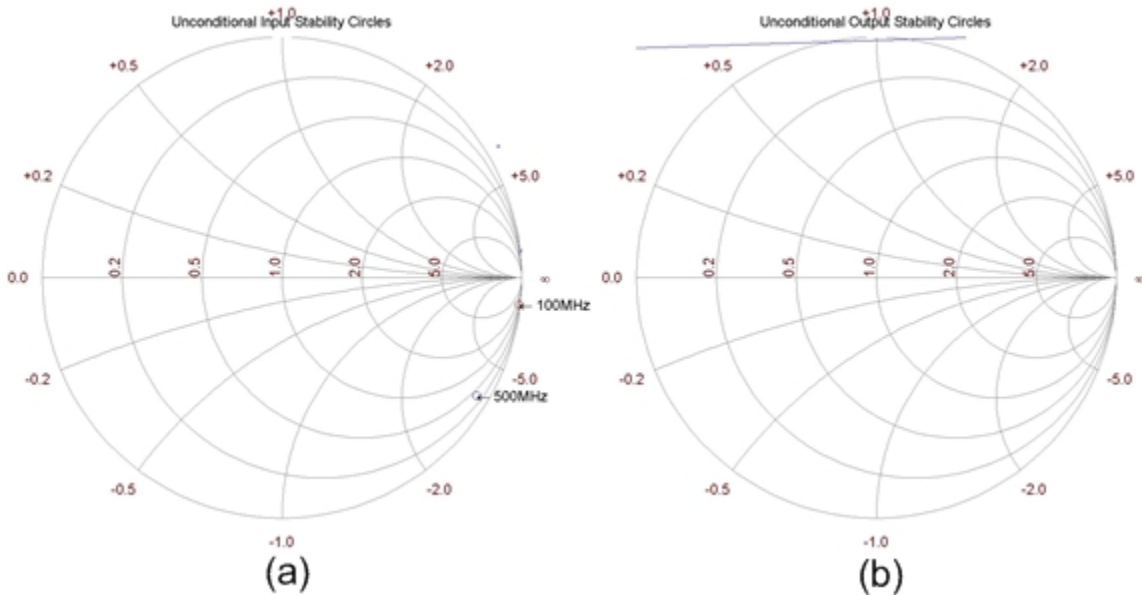


**Figure 6-4 - (a) Unconditional stability at the input, (b) unconditional stability at the output.**

With the attenuation determined, the resistors R1, R2 and R3 can be calculated so that an attenuation of 11.8dB is obtained. These values can be calculated using Equations (57), (58), and (59),

$$R_1 = \frac{1}{\frac{A+1}{Z_1(A-1)} - \frac{1}{R_2}} \quad (57)$$

$$R_2 = \frac{1}{2}(A-1)\sqrt{\frac{Z_1 Z_2}{A}} \quad (58)$$

$$R_3 = \frac{1}{\frac{A+1}{Z_2(A-1)} - \frac{1}{R_2}} \quad (59)$$

where  $Z_1$  and  $Z_2$  are the impedances of the lines connected to the attenuator on the left and right respectively [26]. These lines are equal to  $50\Omega$  and  $A$  is the attenuation factor calculated from Equation (60) where  $A_{dB}$  is the attenuation in dB which equals 11.8dB [26].

$$A = 10^{\frac{-A_{dB}}{10}} \quad (60)$$

Through calculation, resistors R1, R2 and R3 are calculated to be  $84.5\Omega$ ,  $90.8\Omega$  and  $84.5\Omega$ , respectively.

With the first stage proving unconditionally stable, the second stage can be connected as shown in Figure 6-5.

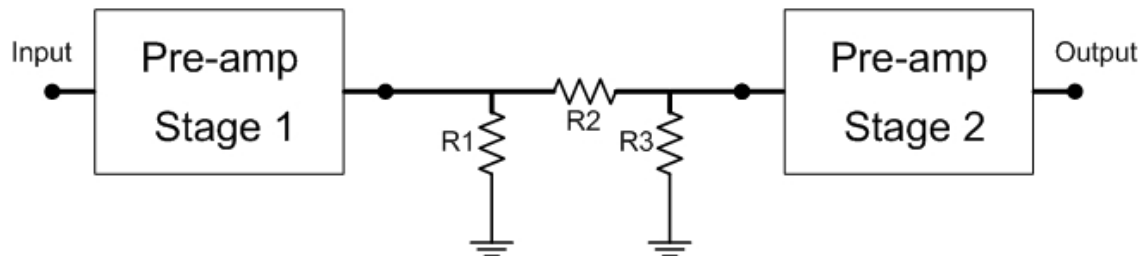
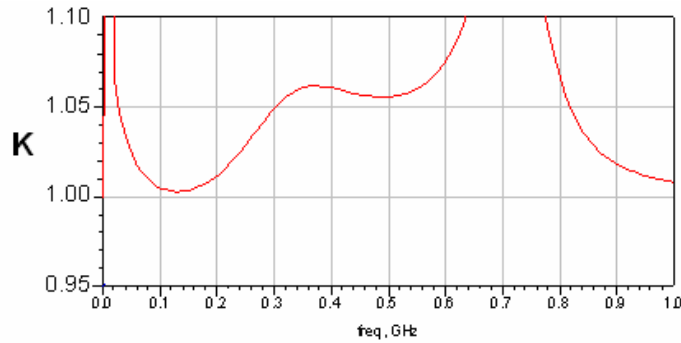


Figure 6-5 - Designed dual stage preamplifier with no matching on the input or output.

Due to the complexity of developing a code in MATLAB to display the unconditional stability of the two connected stages, a simulation performed in ADS can be considered, see Figure 6-6. Note that the dual stage configuration is indeed unconditionally stable with  $k$  being greater than 1.



**Figure 6-6 – Overall stability of dual stage preamplifier.**

Upon further investigation, it was discovered that through the tuning features in ADS the value of attenuation could be decreased to 10.5dB. This decrease in attenuation allows for an increase in gain of 1.3dB. The new attenuation value is then used to calculate the new values for  $R_1$ ,  $R_2$  and  $R_3$  which now are to be  $93\Omega$ ,  $77\Omega$  and  $93\Omega$ , respectively.

Once the entire preamplifier is proven to be unconditionally stable, it becomes necessary to create matching networks on the input and output to ensure power flow [14]. This can be utilized by using the bilateral representation of the dual stage preamplifier seen in Figure 6-7.

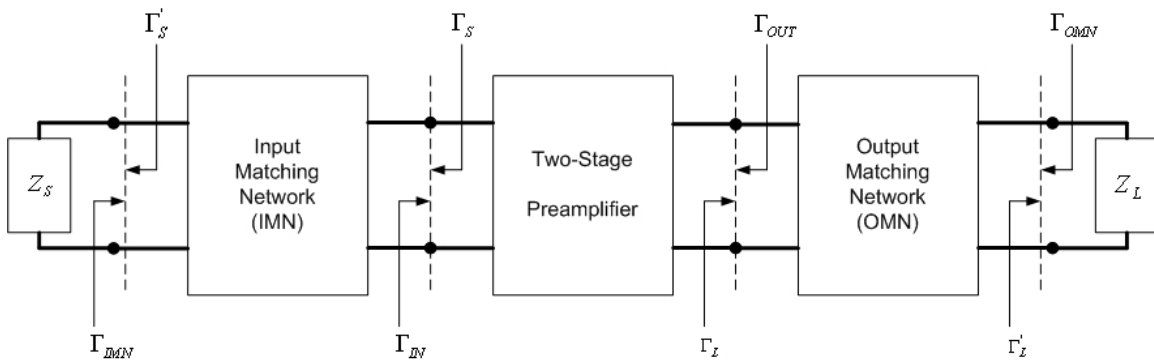


**Figure 6-7 - Bilateral matching representation.**

The first matching network to be addressed is the one which is placed on the input of the preamplifier. Since this particular preamplifier has a bandwidth ranging from 100MHz to 500MHz, a width-bandwidth, low Q, matching network must be considered. As stated in Chapter 3, the input matching network is matched to the point where minimum noise and sufficient gain can be achieved. Figure 6-8 are the ADS simulations of noise and gain circles which will be used to find this optimal point.

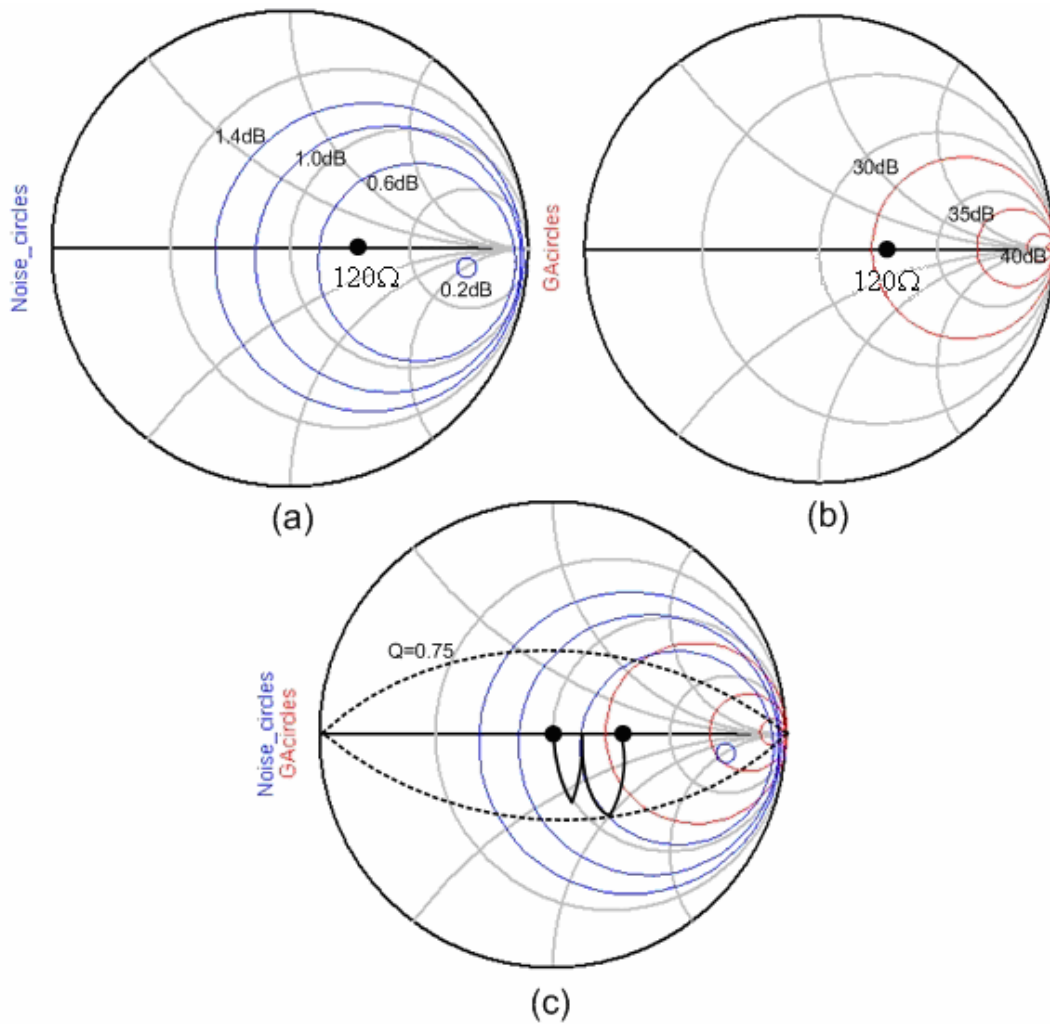


**Figure 6-8 - (a) Noise circles, (b) gain circles, and (c) noise and gain circles with the wide bandwidth ( $Q=0.75$ ) matching network.**



At a point of approximately  $120\Omega$ , shown in Figure 6-8 (a) and (b), the noise and gain values are in the circles of  $0.6dB$  and  $30dB$  respectively. These values suggest that this point will be a good point to match.

After finding the optimal matching point the quality factor  $Q$  is determined for the bandwidth of  $100MHz$  to  $500 MHz$ ,

$$Q = \frac{f_c}{BW^{3dB}} = \frac{300MHz}{500MHz - 100MHz} = 0.75 \quad (61)$$

Using Figure 6-8 (c) as a reference the  $Q$  circle of  $Q = 0.75$  is plotted including the noise and gain circles and the determined low  $Q$  matching network is adopted. Note that there is no rotation into the upper half of the Smith Chart. Through trial and error using different  $L$  and  $C$  combinations, it was found that no inductors can be placed in shunt to ground as it significantly decreases the high input reflection coefficient. This decrease is caused by non-ideal quality factors of the inductors. When solving for the values of inductors and capacitors, the methods described in Chapter 3 will be utilized.

Figure 6-9, shown below, is the template for the designed matching network. In designing the matching network the solving for the virtual resistor with  $Q = 0.75$  from  $R_p$  is computed first. Then the  $Q$  from the virtual resistor  $R_v$  to  $R_s$  is calculated. As long as the  $Q$  from the  $R_v$  to  $R_s$  is  $Q \leq 0.75$ , the network bandwidth will be met.

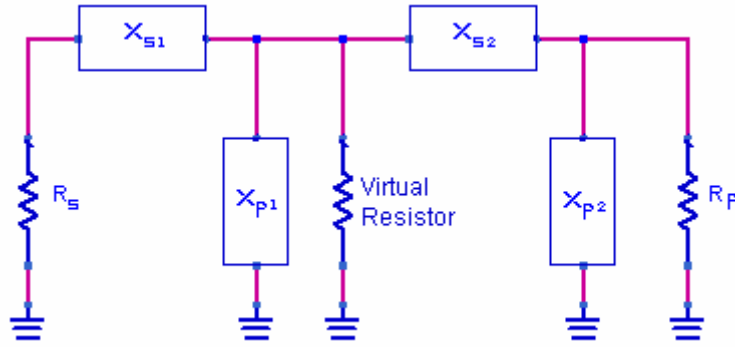


**Figure 6-9 - Matching network for input of dual stage preamplifier.**

By using Equation (62), the virtual resistor  $R_v$  can be calculated

$$Q = \sqrt{\frac{R_P}{R_V} - 1} ; \quad 0.75 = \sqrt{\frac{120\Omega}{R_V} - 1} ; \quad R_V = 76.8\Omega \quad (62)$$

The  $Q$  from  $R_v$  to  $R_s$  is then calculated to ensure that the bandwidth requirement is met.

This can be seen in Equation (63). If the  $Q$  had not met the requirement of 0.75 or below, another L network would need to be added to the matching network.

$$Q = \sqrt{\frac{R_V}{R_S} - 1} = \sqrt{\frac{76.8\Omega}{50\Omega} - 1} = 0.73 \quad (63)$$

From Equations (62) and (63) the calculations of the bandwidth will be met and the values for the network can be calculated. It is important to remember that the low  $Q$  network is analyzed by breaking it down into two simple L networks as explained in Chapter 3. All calculations are then as follows.

$$Q_S = \frac{X_{S1}}{R_S}, \quad 0.73 = \frac{X_{S1}}{50} \quad \text{or} \quad X_{S1} = 36.5 \quad (64)$$

$$LM1 = \frac{X_{S1}}{2\pi \cdot f_c} = \frac{36.5}{2\pi \cdot 300\text{MHz}} = 19.36\text{nH}$$

The calculated inductance shown in Equation (64) is the series component that will take the place of  $X_{S1}$ .

$$Q_P = \frac{R_V}{X_{P1}}, \quad 0.73 = \frac{76.8}{X_{P1}} \quad \text{or} \quad X_{P1} = 105.3 \quad (65)$$

$$CM1 = \frac{1}{X_{P1} \cdot 2\pi \cdot f_C} = \frac{1}{105.3 \cdot 2\pi \cdot 300\text{MHz}} = 5.03\text{pF}$$

The calculated capacitance shown in Equation (65) is the shunt component that will take the place of  $X_{P1}$ . Note that the  $Q$  used for this section of the L network is the calculated value of 0.73 from Equation (63) and that  $f_C$  is the center frequency of the network.

$$Q_S = \frac{X_{S2}}{R_V}, \quad 0.75 = \frac{X_{S2}}{76.8} \quad \text{or} \quad X_{S2} = 57.6 \quad (66)$$

$$LM2 = \frac{X_{S2}}{2\pi \cdot f_C} = \frac{57.6}{2\pi \cdot 300\text{MHz}} = 30.5\text{nH}$$

This calculated inductance shown in Equation (66) is the series component to take the place of  $X_{S2}$ .

$$Q_P = \frac{R_P}{X_{P2}}, \quad 0.75 = \frac{120}{X_{P2}} \quad \text{or} \quad X_{P2} = 160.0 \quad (67)$$

$$CM2 = \frac{1}{X_{P2} \cdot 2\pi \cdot f_C} = \frac{1}{160.0 \cdot 2\pi \cdot 300\text{MHz}} = 3.3\text{pF}$$

This calculated capacitance shown in Equation (67) is the shunt component to take the place of  $X_{P2}$ . Note that the  $Q$  used for this section of the L network is the calculated value of 0.75 which was chosen for the bandwidth requirement. After all components are in place, the designed low-Q matching network is completed and shown in Figure 6-10.

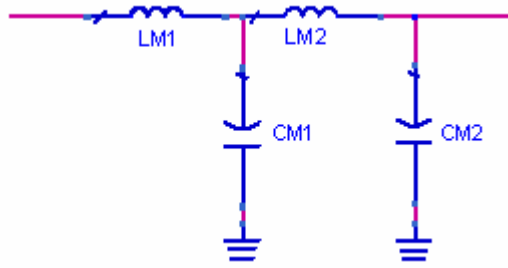


**Figure 6-10 - The designed input matching network.**

After completing the input matching network ADS simulations were utilized to investigate the performance of the wide bandwidth matching network. Figure 6-11 illustrates the plotted NF and minimum NF from 10 MHz to 1GHz. Note that the bandwidth is not only met, but is exceeded with extra bandwidth of up to 700 MHz and the noise level is below the requirement of 0.8dB.

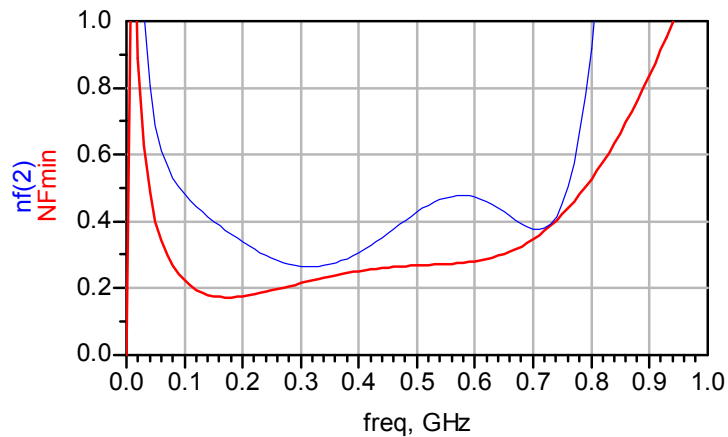


**Figure 6-11 - Simulated noise figure and minimum noise figure.**

Once the noise requirement is met, the input reflection coefficient can be considered, seen in Figure 6-12. Note that the reflection is above 0.90 over the bandwidth of 100MHz to 500MHz to meet the high reflection requirement which will be sufficient for decoupling.

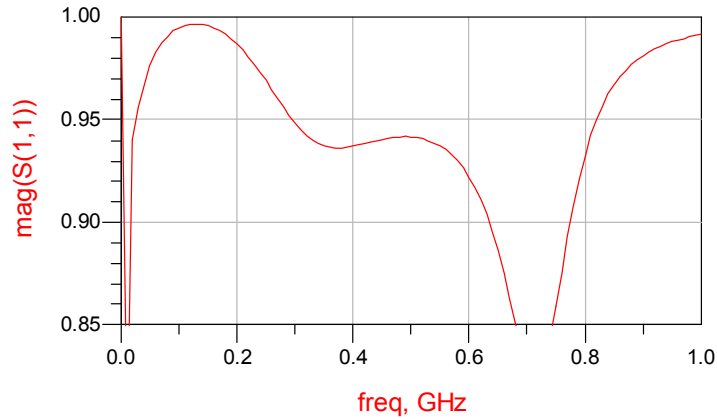


**Figure 6-12 - Input reflection coefficient with wide bandwidth matching network.**

Now that the input matching network is designed and simulated, the output matching network is determined. Again, due to the bandwidth requirement, a low-Q network is essential. After two stages of gain, a small amount of gain can be sacrificed and a resistive network can be constructed as seen in Figure 6-13 (a). This network was designed by the needed transitions on the Smith Chart at the center frequency of 300MHz, seen in Figure 6-13 (b). This transition results in a resistance of  $75\Omega$  and an inductance of  $2.2nH$ . It is noted that this is a lossy network with a loss on the order of 1.5dB. Figure 6-13 (c) is the ADS simulation depicting the matching to the output.

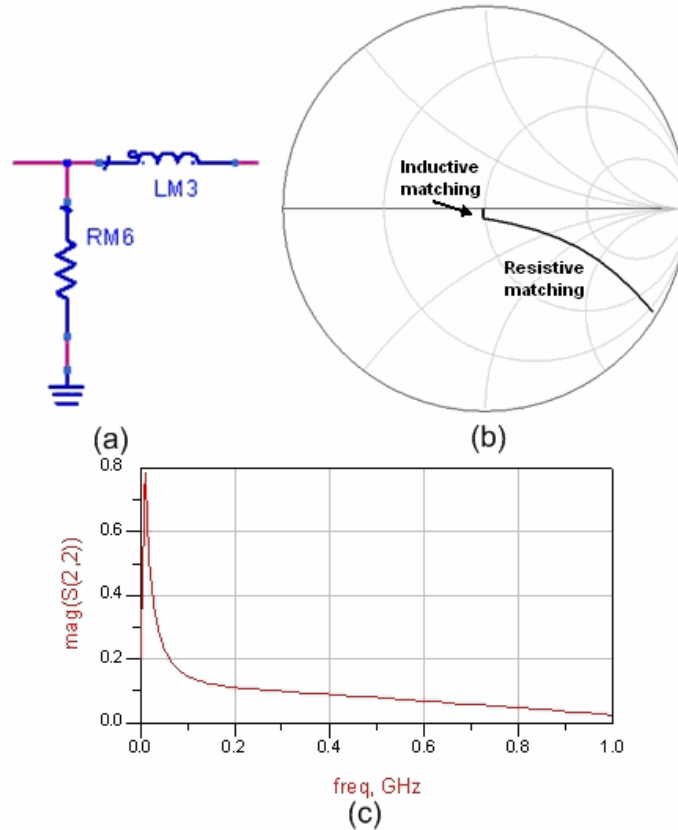


**Figure 6-13 - (a) Output matching network, (b) the Smith Chart rotation made by the network, (c) output reflection coefficient  $S_{22}$ .**

After the input and output matching networks are designed, the gain of the entire dual stage preamplifier was simulated and is seen in Figure 6-14. Note that over the entire bandwidth the gain is above the required 30dB gain specification.

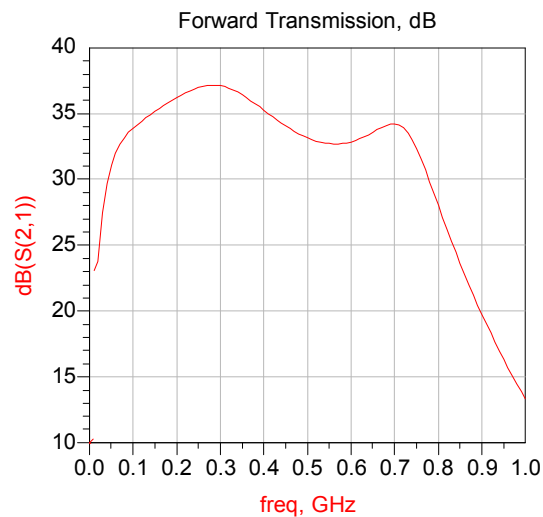


**Figure 6-14 - Entire gain of dual stage preamplifier.**

Finally with the complete amplifier design the entire schematic of the dual stage preamplifier is displayed in Figure 6-15. All component values shown in this schematic are listed in Table 1. It is important to note that although the detuning network is attached to the input, it does not affect the input matching network. This is due in part to the size of the components compared to those in the matching network at the frequency of operation and partly due to the detune not being on at the time of operation. As discussed in Chapter 2, the detune circuit is the MRI hardware that allows for the RF pulse to be sent to stimulate the atoms.

With all ADS simulations meeting the dual stage preamplifier requirements the next logical step is to design a layout and construct a dual stage board.

**Table 1- Component values for dual stage preamplifier.**

Components	Values
LD1, LD2	0.56uH
LM1	22nH
LM2	27nH
LM3	2.2nH
LF1, LF2, LF3, LF4	390nH
CD1, CD2	1000pF
CB1, CB2, CB3, CB4	1000pF
C1, C2, C3, C4	1uF
C5, C6	0.1uF

Components	Values
RL1, RR1	4.3K $\Omega$
RL2, RR2	5.7K $\Omega$
RL3, RR3	143 $\Omega$
RL4, RR4	10 $\Omega$
RL5, RR5	10K $\Omega$
RL6, RR6	1.0K $\Omega$
RM2, RM4	93 $\Omega$
RM3	77 $\Omega$
RM6	75 $\Omega$
RM1, RM5	0 $\Omega$

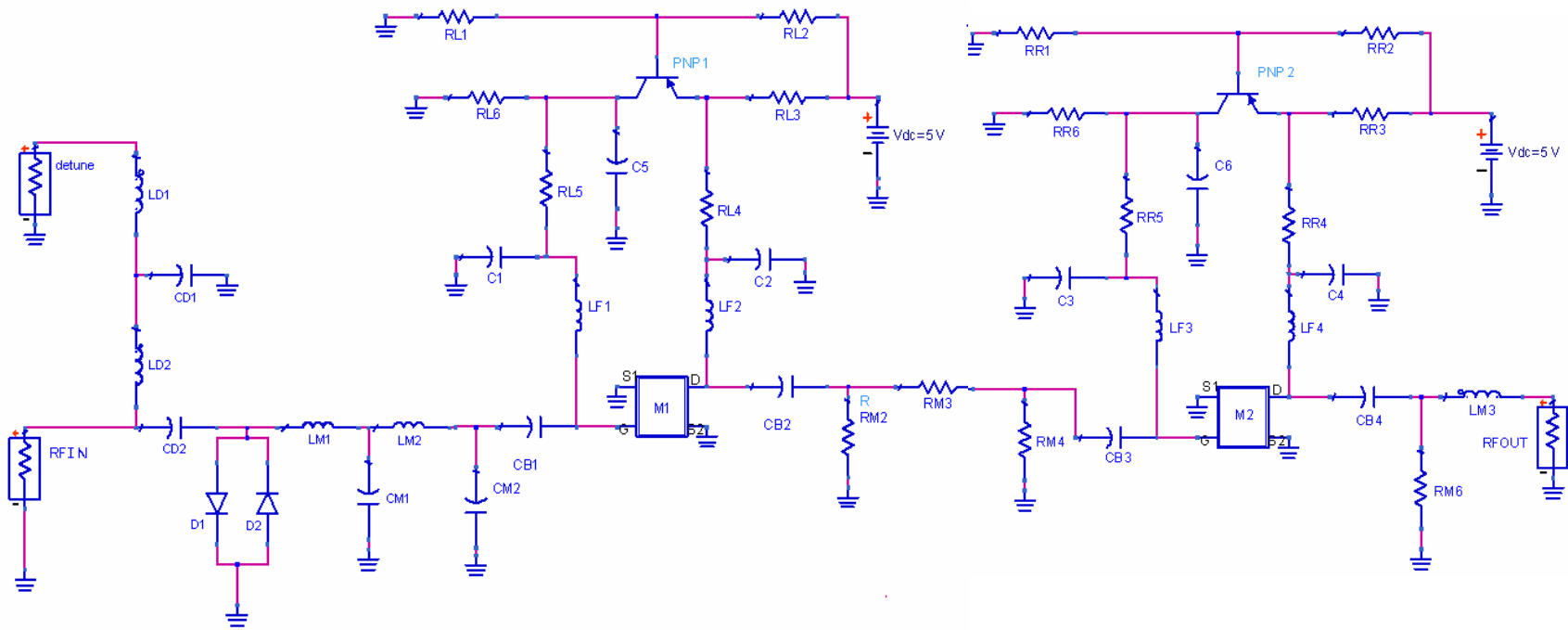


Figure 6-15 - Entire dual stage preamplifier schematic with detuning network attached.



## **6.2. Layout and Construction**

To meet the requirements of this thesis the dual stage preamplifier must be built as small as possible. For this reason, all components are in *0603* packages with the very small ATF-551M4 transistors as the center points of design. The ATF-551M4 transistor is the primary component in this preamplifier design and as such the layout of each stage was built around these transistors. A four layer FR-4 board was used to meet the low noise figure requirements as it provides more isolation of noise than that of two layer boards. The production of the boards was completed by ExpressPCB. This company also provided the necessary software to create the PCB layouts.

In order to reduce the size of the board, the RF components were separated from the DC biasing components. This need for separation resulted in all RF components being located on the top of the board, as seen in Figure 6-16. Consequently all DC biasing components are then placed on the bottom of the board and fed through by vias in the proper locations to connect to the top layer. The layout of the bottom layer can be seen in Figure 6-17.

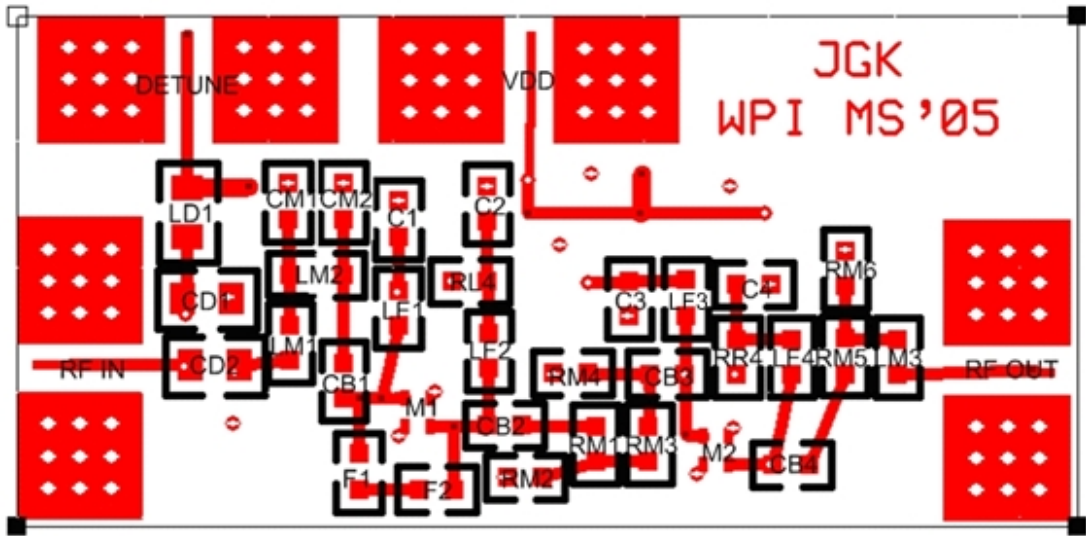


Figure 6-16 - Dual stage preamplifier- top layer.

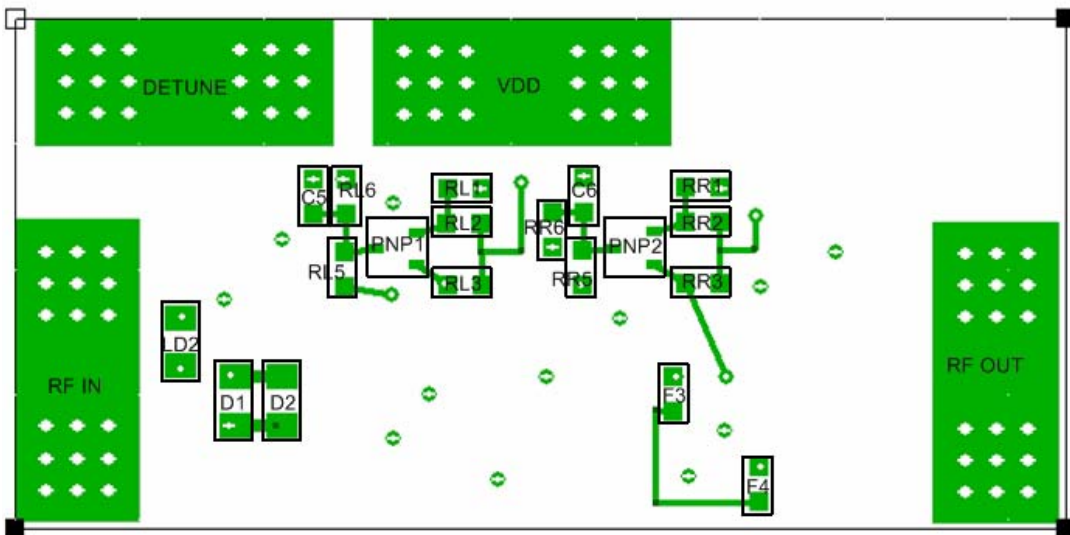
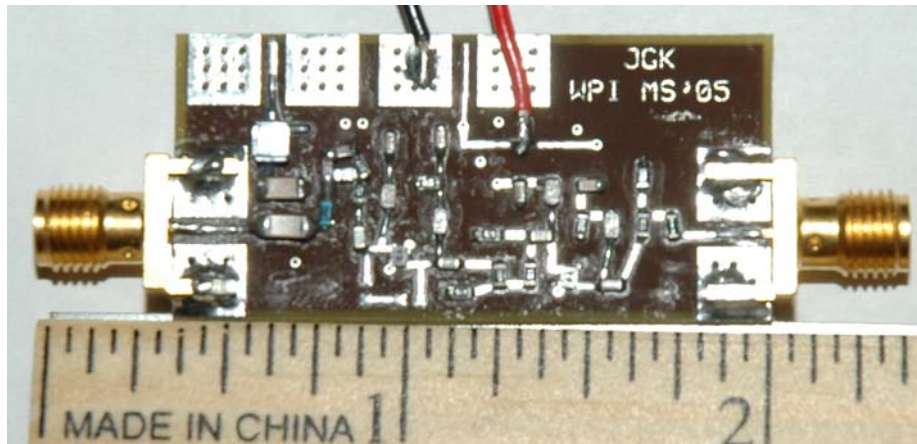


Figure 6-17 - Dual stage preamplifier- bottom layer.

To keep the overall size of the board to a minimum and reduce all parasitic capacitance and inductance all components were placed as close together as possible. All inductor positioning was also considered to ensure that there was no mutual induction created between them. In the case that two inductors had to be positioned close to each other, considerations were taken to place them at  $90^\circ$  to ensure no mutual induction.

One of the dual stage preamplifiers built can be seen in Figure 6-18.

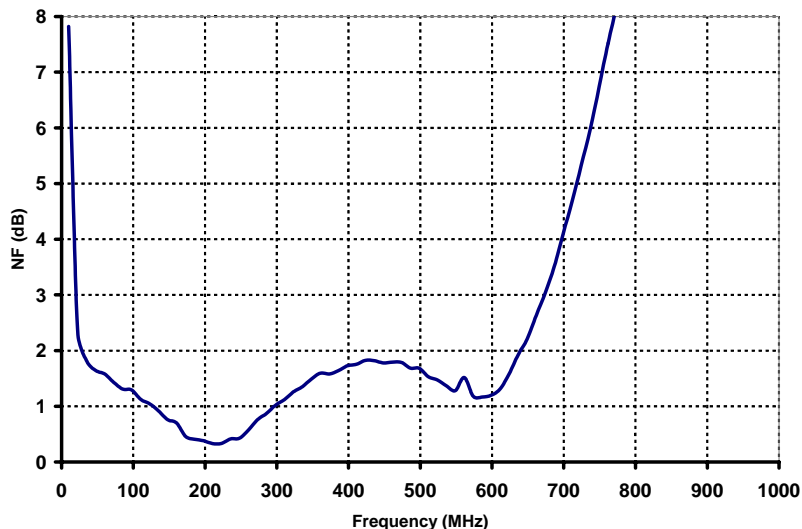


**Figure 6-18 - Constructed dual stage preamplifier.**

### ***6.3. Tested Results of the Dual stage Preamplifier***

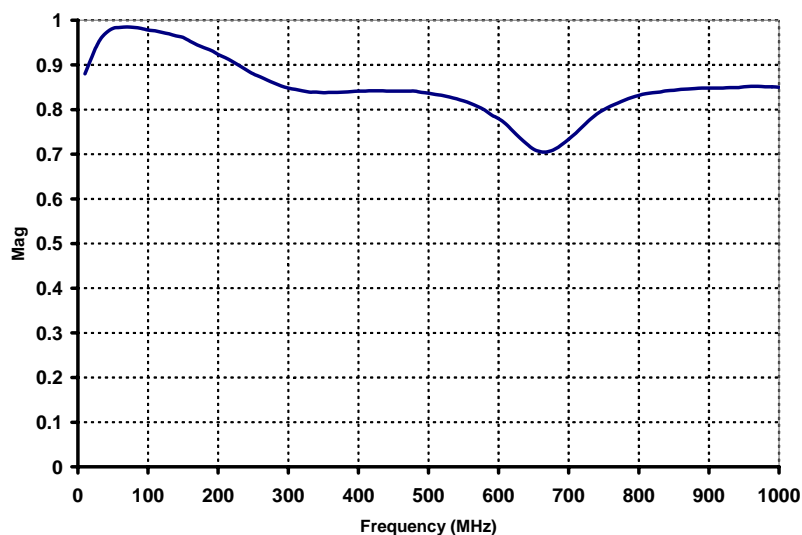
Once all four dual stage preamplifiers were built, data collection was conducted on each board. To maintain a consistent environment, data collected from each board was gathered using the same equipment. Only data collected from board 1 will be investigated here; all data collected on the other boards will be summarized in Appendix B.

The measured noise from board 1 can be seen in Figure 6-19 below. Further investigation shows the noise from board 1 is very similar to the noise simulated in ADS. The only major difference is that the noise is 0.5dB higher than simulated results at 100MHz and 500MHz and is 0.3dB at 300MHz which is lower. This divergence from simulated results may be due to the nonideal low quality Q of the inductors in the input matching network. A possible solution to this may be to use inductors possibly in 1210 packages or larger as they tend to carry a higher quality Q than the small inductors in 0603 packages.



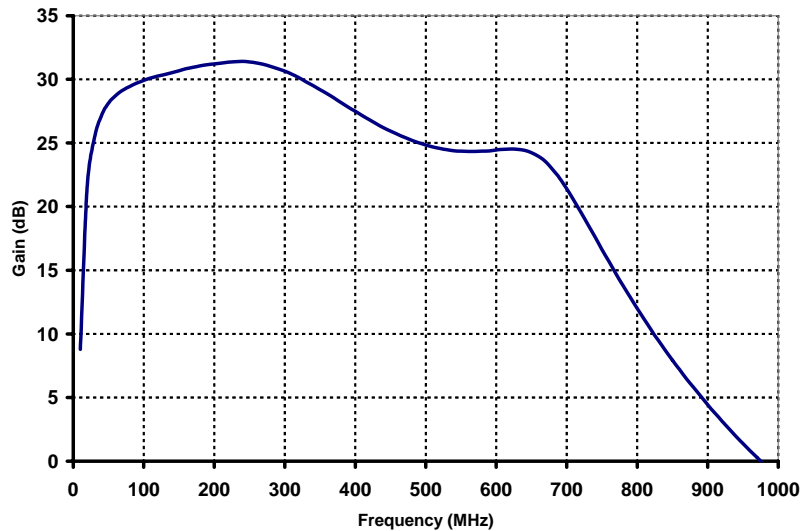
**Figure 6-19 – Measured noise of preamplifier.**

Figure 6-20 is a plot of the magnitude of the input reflection coefficient  $S_{11}$ . Upon investigation, this matches up with the simulated ADS plot of the magnitude of  $S_{11}$ . Here also, there is a slight discrepancy from 200 to 500MHz. It can be seen that the input reflection coefficient is not as high as the simulated value of 0.95. This once again might be due to the effect of the inductors in the input matching network not having a high enough quality factor Q.



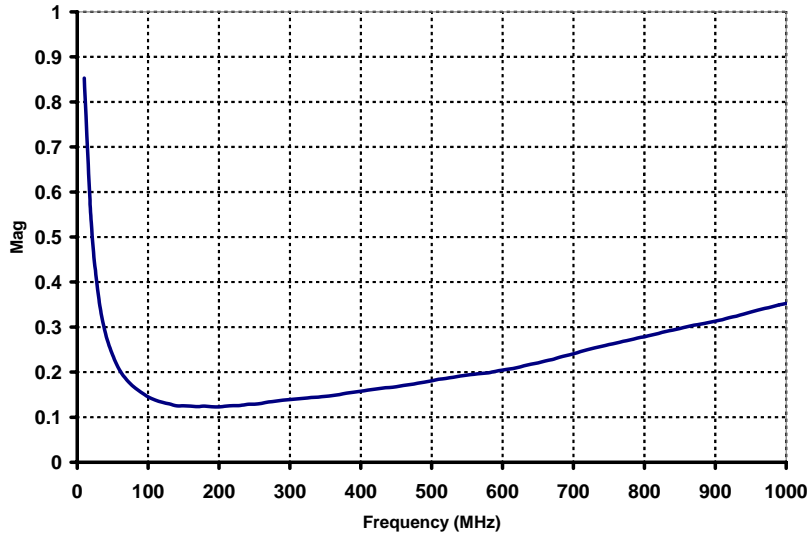
**Figure 6-20 – Measured magnitude of  $S_{11}$ .**

Figure 6-21 below is the measured forward gain of board 1. By investigation this closely resembles the simulated ADS results of  $S_{21}$ . Note that the gain is 5 dB lower than that of the simulations which might be due to the imperfect biasing of each transistor. Due to resistors having a tolerance of  $\pm 5\%$  the network biasing might be off which could affect each stage by a gain 2dB each.



**Figure 6-21 – The measured gain  $S_{21}$  in dB.**

Seen in Figure 6-22, the measured  $S_{22}$  is very close to an optimal match over the entire bandwidth. In comparison to the ADS simulation this matches up very well. It does slowly increase up to higher frequencies. This may be due to the inductor on the output, but this is not a problem.



**Figure 6-22 – Measured output reflection coefficient  $S_{22}$ .**

After reviewing all of the collected data, the dual stage amplifier still provides sufficient gain at low noise levels with a high reflection coefficient. The next logical step is to test the preamplifier in an MRI system to observe if the high input reflection coefficient concept works in decoupling the coils and to investigate if the gain and noise are truly sufficient. To do this only two preamplifiers will be used and a package design was then created and can be seen below in Figure 6-23. It is noted that the third board seen contains a voltage regulator which will provide a solid 5.0V to both preamplifiers.

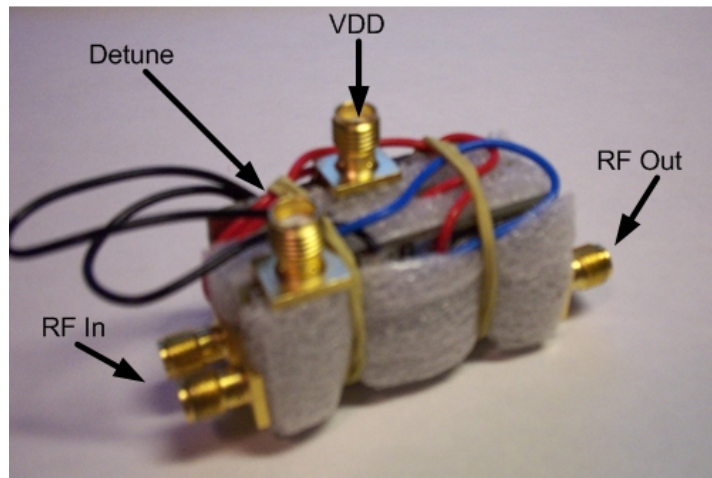


**Figure 6-23 - Two preamplifiers packaged for testing in the MRI system.**

## 7. Testing of Decoupling Concept with Dual stage Preamp

Upon completion of the dual stage preamplifier, the testing in an MRI system was needed to investigate its performance. The testing of the preamplifier will be done in a 4.7T system which is 200MHz. If the dual stage preamplifier enables the decoupling of two coils in an MRI system the main goal of this thesis is would be met. Two coils were built and attached to the preamplifier to investigate this decoupling concept. Figure 7-1, shows the typical design of the necessary circuits needed to connect the coil to the preamplifier. As described in Chapter 3, the phase shifter will be a 50Ω cable with a length of  $3\lambda/4$ ; it will shift the high impedance of the preamplifier to a low impedance (a short). The matching network will then match the 50Ω cable to the coil.

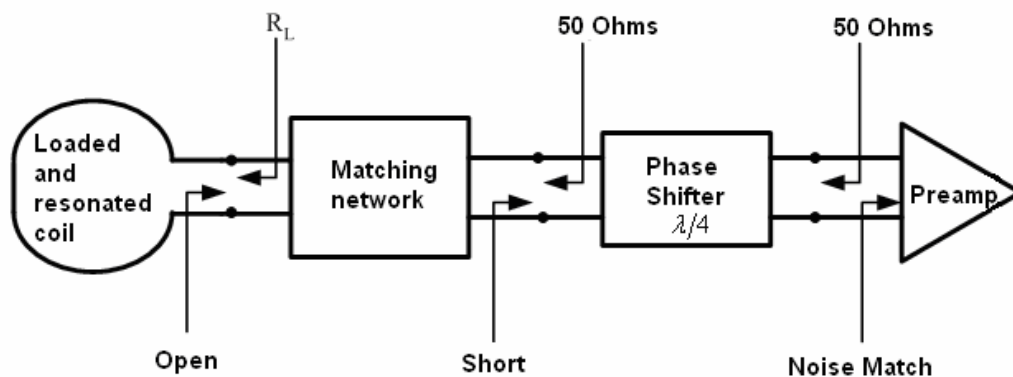


Figure 7-1 - System diagram of the coil connected to the preamplifier.

## 7.1. Construction of Two Coils

In constructing the two coils for testing, a Reykowski based design was used with the addition of a  $\lambda/4$  bazooka balun which will provide a shield current block [22]. Displayed in Figure 7-2 is the chosen matching network to the coil with exception of the balun.

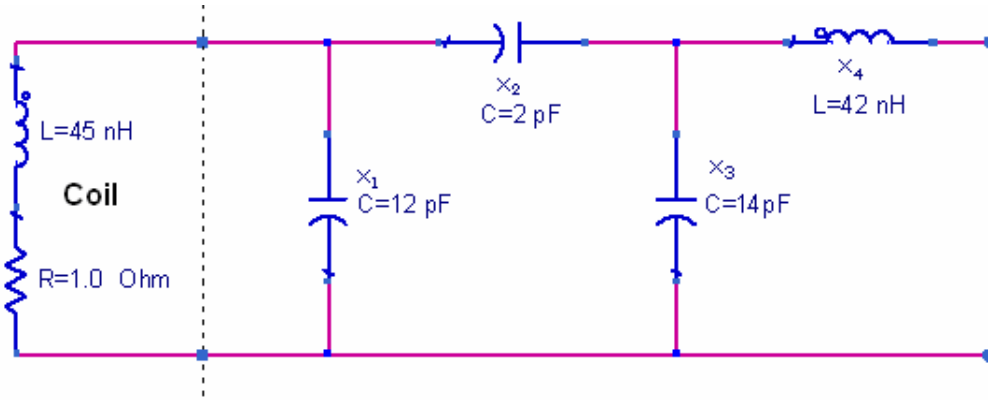


Figure 7-2 - The matching network required to connect the coil to the cable.

To calculate the component values, Equations (68) through (70) are used as intermediate equations, with  $Z_{Amp} \approx 0$  being the transformed impedance seen by the matching network and  $Z_0$  being the characteristic impedance of the cable. Also noted is the resistance and reactance of the coil  $R$  and  $X_L$ , respectively. Equation (71) is used to calculate the reactance of the inductor  $L_1 = 42nH$  at the test frequency of 200MHz. This inductance controls all other calculated values of the matching network [22].

$$A = X_L Z_0 + R \cdot X_{Amp} = 2.827 \times 10^3 \quad (68)$$

$$B = -\sqrt{R \cdot Z_0 (X_{Amp}^2 + Z_0^2)} = -375.994 \quad (69)$$

$$C = R \cdot Z_0 - X_L X_{Amp} = 56.549 \quad (70)$$

$$X_4 = \omega \cdot L_1 \quad X_4 = 51.648 \quad (71)$$



Equation (72) is used to calculate the value of  $C_1$  from the reactance component  $X_1$ . In the matching network  $C_1$  controls the appropriate resonance frequency of the coil. To achieve fine tuning  $C_1$  will be a tunable capacitor with a range of 4.5 to 20pF.

$$X_1 = A \cdot \frac{(X_4 A - Z_0 C)}{(Z_0 X_4 A - Z_0^2 C + B \cdot A + B^2)} \quad (72)$$

$$C_1 = \frac{1}{\omega X_1} = 12 pF$$

Equation (73) is used to calculate the value of  $C_2$  from the reactance component  $X_2$ . In the matching network  $C_2$  controls the actual matching in the circuit from the coil to the cable. Again, to achieve fine tuning;  $C_2$  will be a tunable capacitor with a range of 2 to 6pF.

$$X_2 = \frac{-(X_4 A - Z_0 C)}{B} \quad (73)$$

$$C_2 = \frac{1}{\omega X_2} = 2 pF$$

Equation (74) is used to calculate the value of  $C_3$  from the reactance component  $X_3$ .  $C_3$  controls the phase correction needed to tune the coil. In order to fine tune,  $C_3$  will be a tunable capacitor with a range of 4.5 to 20pF.

$$X_3 = \frac{(X_4 A - Z_0 C)}{(A + B)} \quad (74)$$

$$C_3 = \frac{1}{\omega X_3} = 14 pF$$

After the network is calculated the balun can be attached to the output. The balun is built by using a tri-coaxial cable to connect the matching network to the preamplifier. A tri-coaxial has the same properties of a regular coax cable but with an additional outer shield. The strategy used for building the bazooka balun was to shorten the outer to the inner shield at a length slightly less than  $\lambda/4$ . In addition, a tunable capacitor was placed

on the other end between the inner and outer shielding which allowed for a fine tuning of exactly  $\lambda/4$ . This can be seen in Figure 7-3.

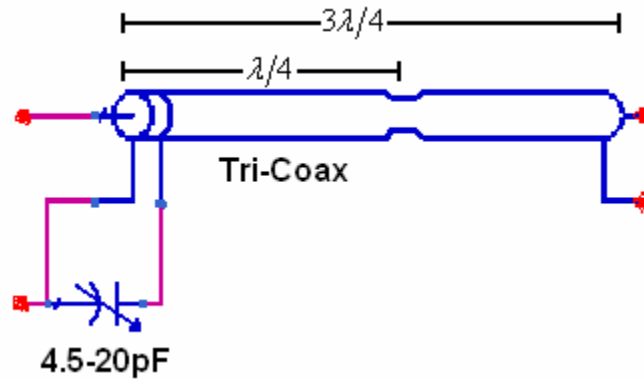


**Figure 7-3 - Balun constructed from tri-coaxial cable.**

With the matching network and balun designed a layout of the coil boards can be constructed. Seen in Figure 7-4 is the ExpressPCB layout of the coil. Note that there are addition components  $CL1$ ,  $CL2$ ,  $D1$ , as well as  $L2$  and  $L3$  used as RF chokes. These components are necessary to achieve a detuning of the coil. This network provides a dc pulse to the coil causing  $CL1$  and  $CL2$  being the only real difference in the matching network. Due to a needed cut in the coil for detuning, the addition of the capacitors  $CL1 = 27\text{ pF}$  and  $CL2 = 12\text{ pF}$  in series is equal to approximately  $8\text{ pF}$ . With fine tuning, a tunable capacitor  $C1$  ranging from  $4.5\text{--}20\text{ pF}$  is put in parallel with  $CL2$  to create the needed  $12\text{ pF}$  for the tuned resonance of  $200\text{ MHz}$ .

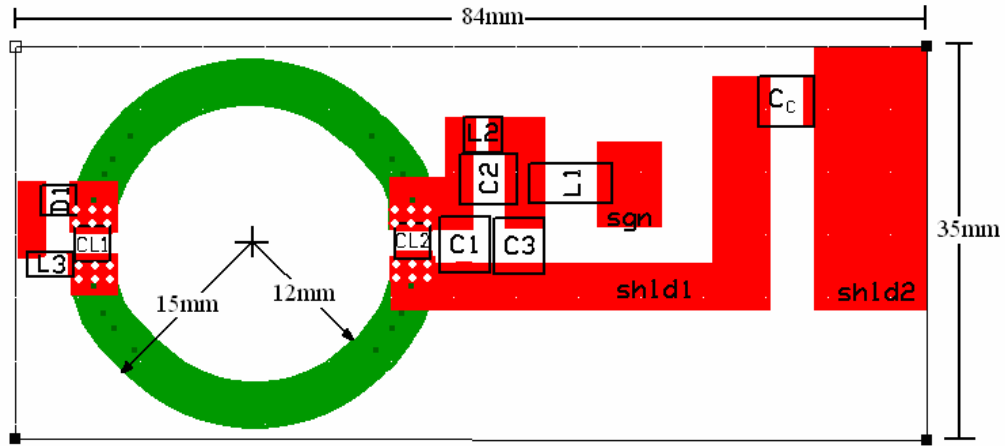


**Figure 7-4 - Layout of coil on bottom layer, with matching network with addition detuning components on top layer.**

Figure 7-5 displays the constructed coil, while Figure 7-6 is shows the coil along with the  $\lambda/4$  balun.

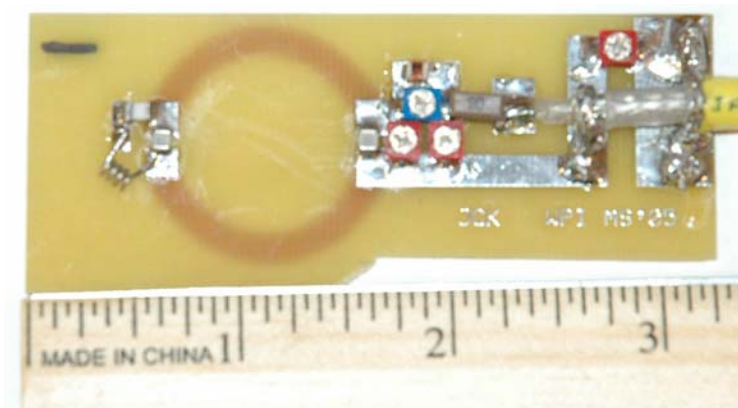


**Figure 7-5 - Constructed coil.**

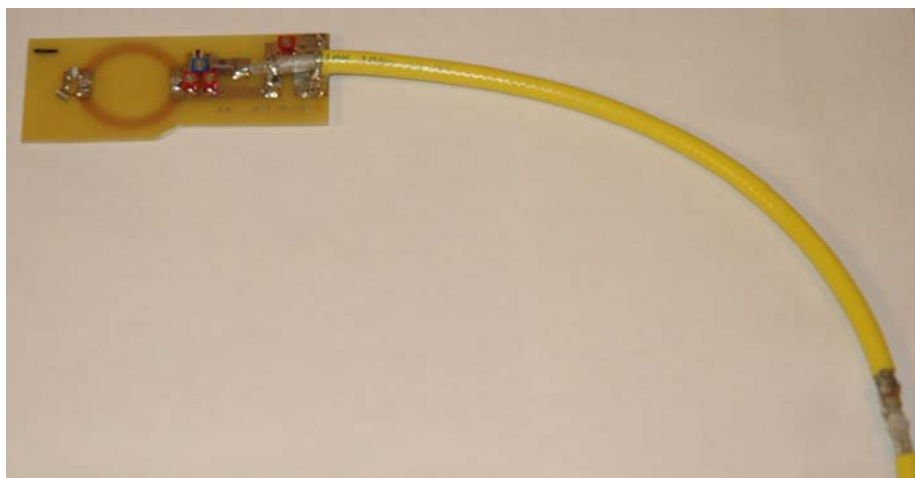


**Figure 7-6 - Constructed board with balun.**

With the completion of the two coils, each coil will need to be tuned to the test frequency of 200MHz. In addition to tuning the resonance of the coil, the phase and the matching will be fine tuned to ensure that the optimal operation is obtained.

## 7.2. Tuning of Coils

The tuning of the coils was first done on a test bench to resolve major tuning issues before conducting the tuning in the magnet room. Figure 7-7 depicts the test setup using ports 1 and 2 of a network analyzer. Two probes are placed on either side of the coil. Probe 1 was used to measure the input reflection coefficient  $S_{11}$ , while probe 2 was used to measure the forward gain  $S_{21}$ .

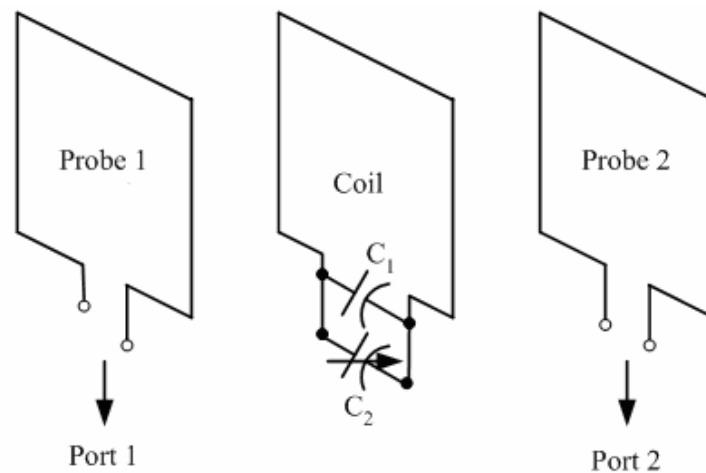
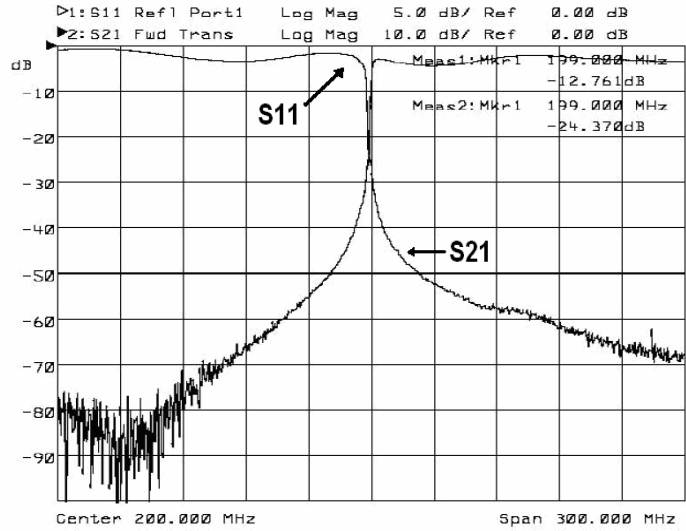


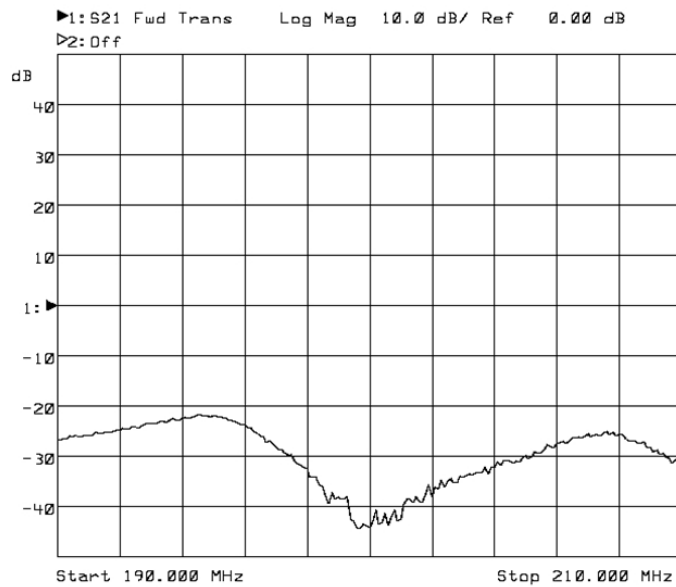
Figure 7-7 - The Tuning setup for each coil.

Figure 7-8 is the measured  $S_{11}$  and  $S_{21}$  after tuning the coil. Note that the coil is tuned to the test frequency of 200MHz and that the gain  $S_{21}$  is maximized at the desired resonance frequency. The same tuning was performed with the second coil.



**Figure 7-8 – Measured resonance at 200MHz and forward gain  $S_{21}$ .**

The phase of each coil is then tuned to the minimum and can be seen in Figure 7-9. This minimum is desired in order to control the ability of the coils to decouple from one another.



**Figure 7-9 - Matching of phase to a minimum.**

After the tuning was performed for each coil, both coils were attached to a phantom. Seen in Figure 7-10 is the splitting of the resonances when coil 1 is connected to the network analyzer and coil 2 is connected to a  $50\Omega$  load.

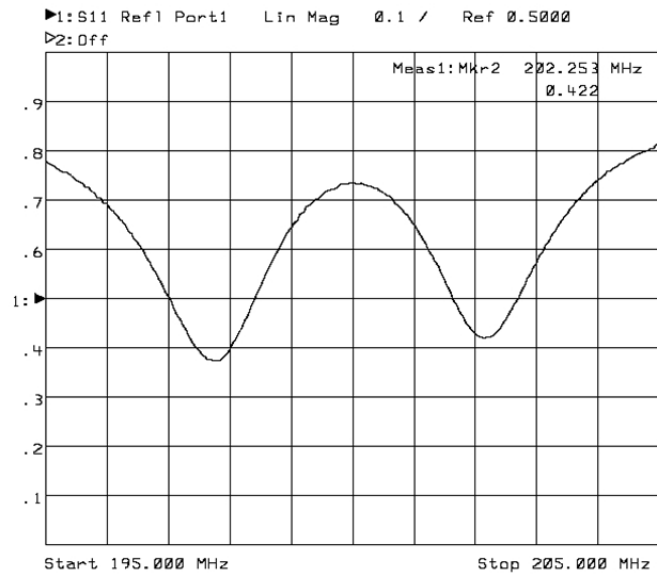


**Figure 7-10 – The resonance splitting when coil 2 is connected to a 50Ω load.**

When the second coil is connected to the preamplifier instead of the 50Ω load, the preamplifier does in fact decouple the two coils due to the reflection coefficient (depicted as  $S_{11}$  trace in Figure 7-11) approaching zero. The next logical step is to conduct simulations for each coil with mutual inductance and to investigate how well the coils should decouple when placed into a MRI system.

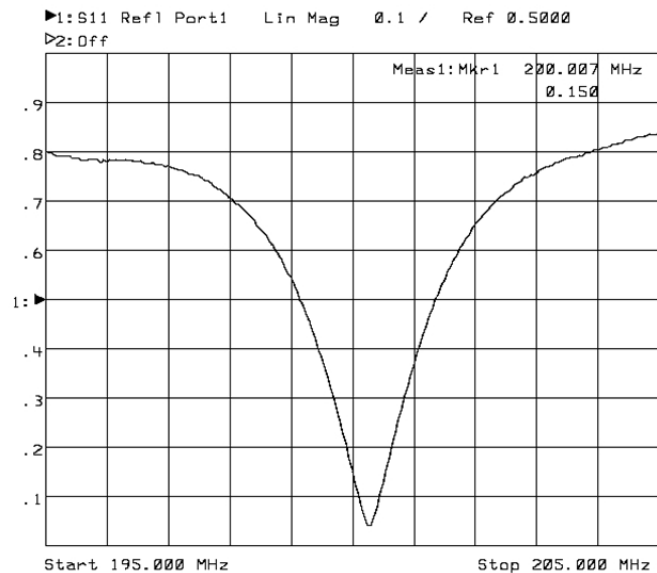


**Figure 7-11 - Resonance seen by coil 1 when coil 2 is decoupled by the high impedance load of the preamplifier.**

### 7.3. Simulation Check

A simulation of the two coils with mutual inductance was investigated to obtain some preliminary results of what exactly will be measured in the magnet room. Seen in Figure 7-12, is the simulation layout of the two coils. Note that the cable is taken into account and  $L4$  and  $L5$  are  $41nH$ . Just like on the bench, the simulation will need to be tuned, which makes  $L4$  and  $L5$  in Figure 7-12 the bases of tuning for all other components. The coil is also simulated with an inductance of  $45nH$  and a capacitance of  $27pF$ .

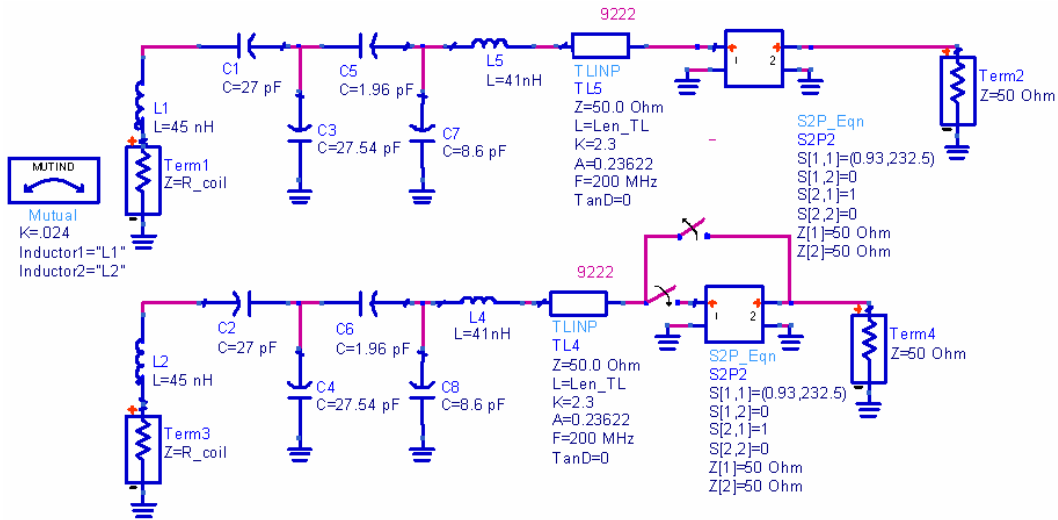
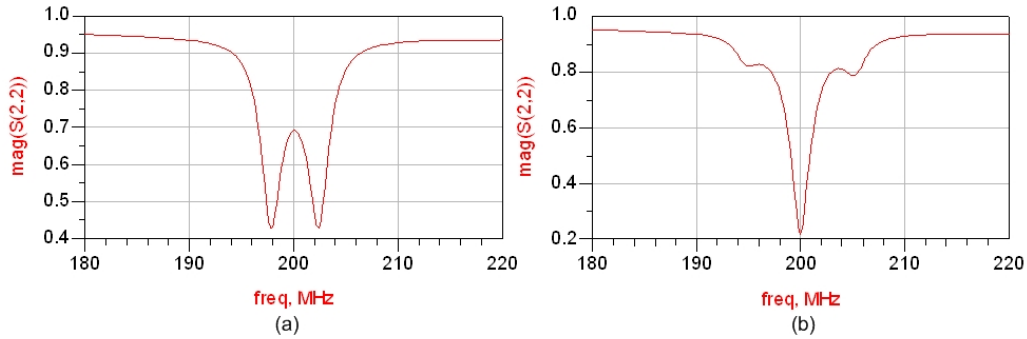


Figure 7-12 - Test simulation of coils connected to the  $50\ \Omega$  load or preamplifier.

In the same fashion as done on the bench, the tuning of each coil is carried out in the simulation by excluding the mutual inductance between each coil and fine tuning the resonance, matching, and phase. Next, the proper amount of mutual inductance needs to be calculated to recreate the same results obtained from the bench testing. Using Equation (75) and the measured splitting of the resonance from Figure 7-10, the mutual inductance factor  $k$  can be calculated [17].

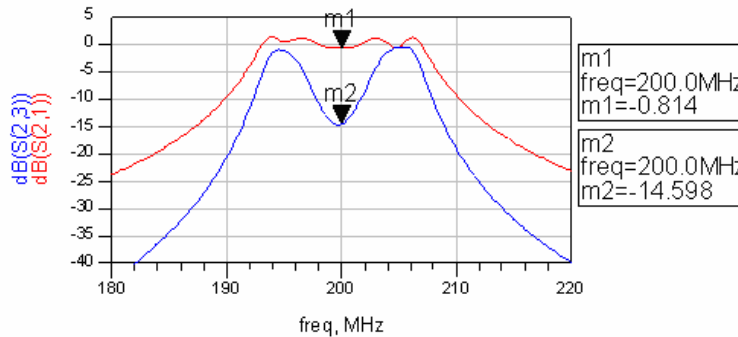
$$k = \frac{f_2^2 - f_1^2}{f_2^2 + f_1^2} = \frac{202.25^2 - 197.75^2}{202.25^2 + 197.75^2} = 0.024 \quad (75)$$

Figure 7-13 (a) and (b) are then generated. These figures represent the splitting and single resonance, respectively, when either a  $50\Omega$  load or the preamplifier are connected to coil 2.



**Figure 7-13 - (a) Splitting of resonance when coil 2 is connected to  $50\Omega$ , (b) one resonance when coil 2 is connected to the preamplifier.**

To investigate the degree of isolation between coil 1 and coil 2  $S_{21}$ , which is the received signal at port 2 when the source is at port 1 (coil 1), and  $S_{23}$ , which is the received signal at port 2 when the source is at port 3 (coil 2), are compared in Figure 7-14. Note that  $S_{23}$  is 14dB less than  $S_{21}$  thus concluding that the preamplifier is indeed decoupling the two coils.



**Figure 7-14 - The simulated isolation between coil 1 and coil 2.**

When comparing these simulated plots and the measure plots on the bench, it can be concluded that the preamplifier does in fact decouple the coils with the mutual inductance created by the measure splitting in resonance. Once decoupling was verified on the bench, the system was then ready to be tested in an MRI facility.



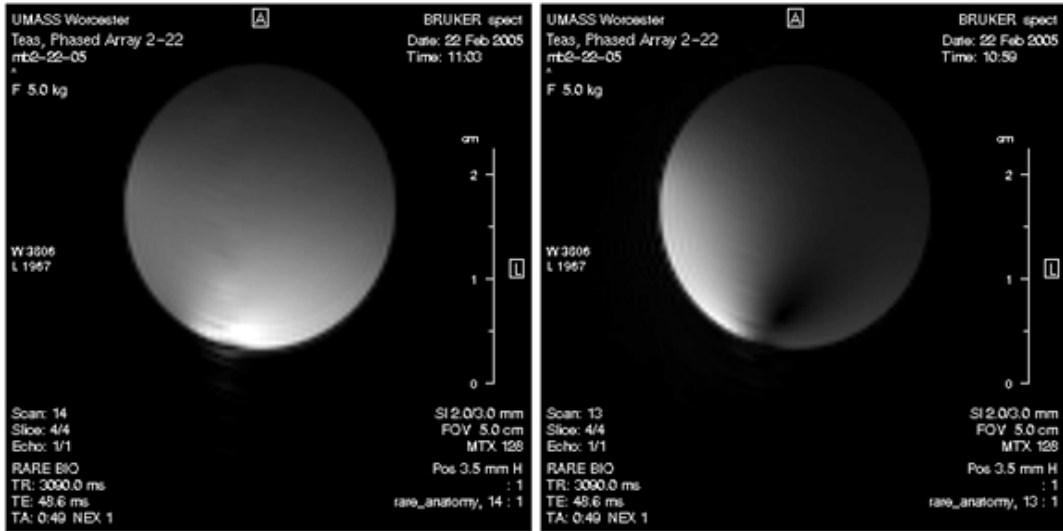
## 7.4. The Magnet Test

After the bench testing and simulated results were investigated, the entire setup was taken to the CCNI facility at UMASS Worcester. The 4.7T MR scanner by Bruker Biospin at CCNI is a single receiver facility where all images are created from one receiver amplifier. As a result, the testing of the coil array system was conducted one coil at a time. The two images produced from each coil were then added by computer image processing to investigate the performance of the combined image created by a two-channel system. For all tests performed the follow setup was used and summarized in Table 2. It is noted that the echo time is 48.6ms which is uncommonly long. Through the testing of the system in the MRI facility a problem occurred with imaging using short echo times. It was later concluded that the preamplifier was requiring a long recovery time from the initial RF pulse of the imaging process. This pulse was charging up capacitor  $CI$  and in a  $RC$  time constant fashion  $CI$  was dissipating through  $RL5$ ; a process that took about 10ms. The echo time was then set to 48.6ms to ensure sufficient time for the preamplifier to recover. This extended echo time lead to the formation of high quality images.

**Table 2 - Test setup parameters.**

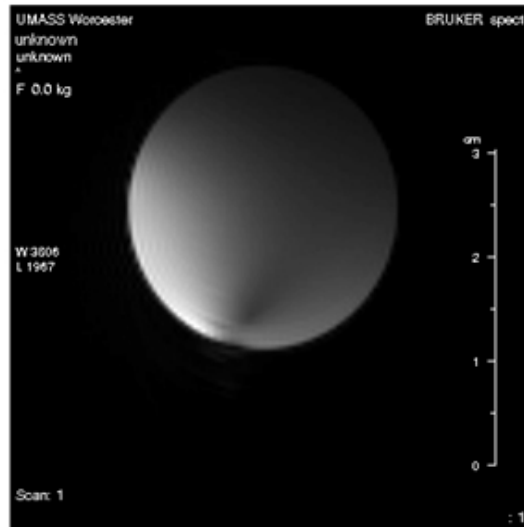
Phantom	Mineral Water
Pulse Sequence	Rare Bio
Matrix Dimension	128
Recovery Time (TR)	3090.0ms
Echo Time (TE)	48.6ms
Field of View (FOV)	5.0cm
Slice Thickness	2.0mm

Figure 7-15 (a) and (b) display the axial slices of the phantom from coil 1 and coil 2, respectively. It is noted that this data was collected when the dual stage preamplifier was used to decouple the coils and the CCNI preamplifier was connected in series. The coils were also placed on the bottom of the phantom in order to avoid imaging an air bubble that was in the sample. From inspection, the intensity of the measure signal is best in the region where the coil is closest to the phantom, hence the brighter image. This occurrence is caused by the increased sensitivity near the coil. As one moves away from the coil, the sensitivity reduces. It can also be seen that as the distance from the coil increases, the image intensity decreases thus becoming darker. Figure 7-15 (c) was then produced by computer processing where both measured images from both coils were added. This image reveals what could be measured in a two channel receiver system. All signal and noise strengths for this test are listed in Table 3.



(a)

(b)



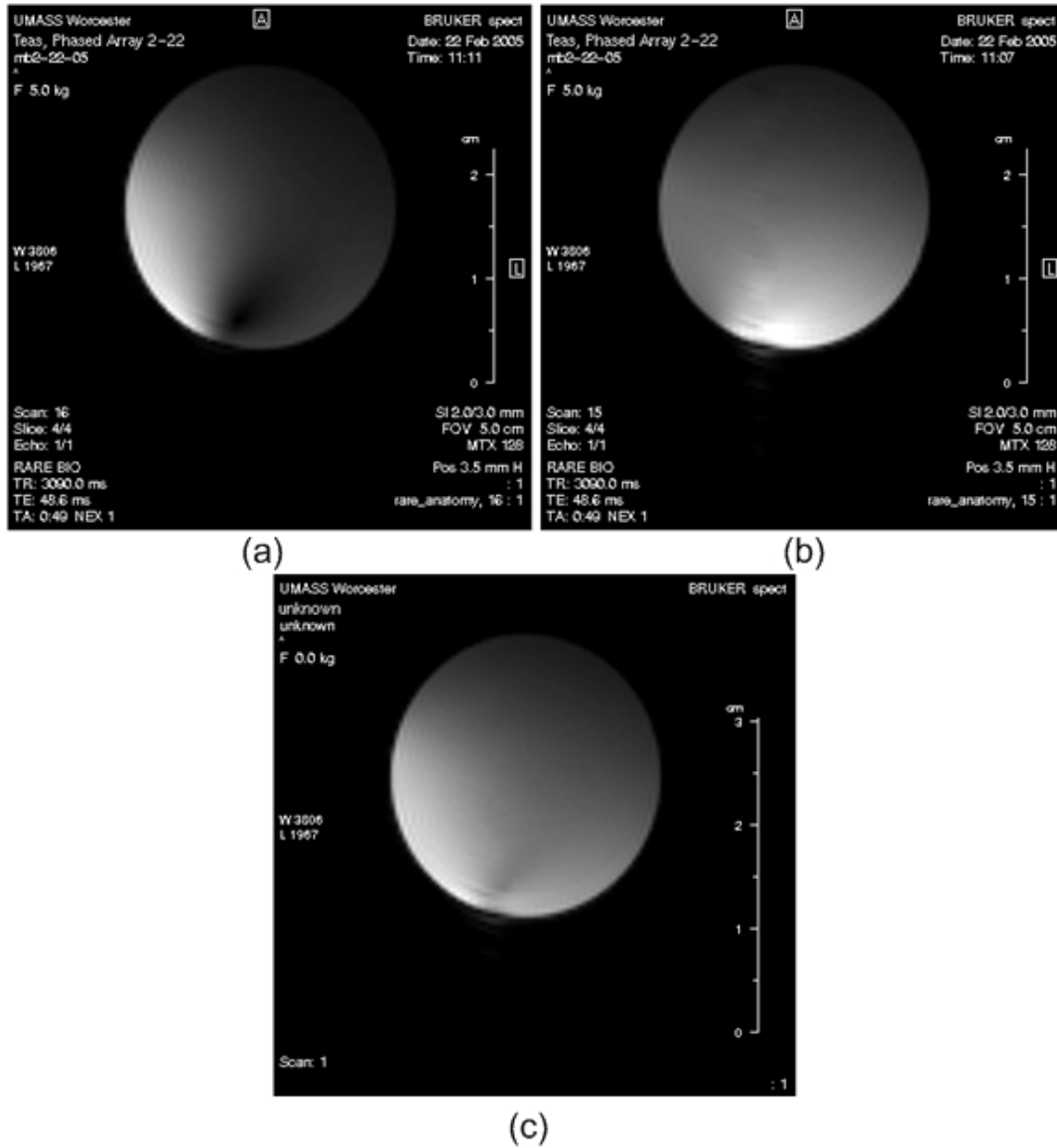
(c)

Figure 7-15 - Image acquired during test with CCNI preamplifier and designed preamplifier in series- (a) image acquired from right coil (b) image acquired from left coil and (c) the addition of both images.

Table 3 - Data collection of coils with CCNI preamplifier in series with designed preamplifier.

	Signal	Noise	SNR
Left coil	1.43E+06	9.32E+03	153.43
Right coil	5.39E+05	2.13E+03	253.05
Both coils	6.55E+05	1.15E+04	56.96

After reviewing the measured data, the CCNI preamplifier was removed so that only the designed dual stage preamplifier is in use. The images produced can be seen in Figure 7-16 and the measured signal and noise strengths are listed in Table 4.



**Figure 7-16 – Image acquired during test with designed preamplifier–  
 (a) image acquired from left coil (b) image acquired from right coil and  
 (c) the addition of both images.**

**Table 4 - Data collected from coils with designed preamplifier decoupling**

	Signal	Noise	SNR
Left coil	1.75E+05	2.91E+03	60.14
Right coil	6.77E+05	2.62E+03	258.40
Both coils	5.69E+06	5.54E+04	102.71

By inspection it can be seen that the images are of the same quality. When comparing the data collected in Table 3 and Table 4, however, the SNR is much better when using the designed dual stage preamplifier on its own.

To ensure that the preamplifier was indeed decoupling the two coils, a wobble test was conducted with coil 2 connected to a  $50\Omega$  load. As seen in Figure 7-17, the bench test and wobble test of the resonance splitting are very close. It is noted that the frequency span of the wobble test is 10 MHz and by inspection the splitting is around 4 to 4.5 MHz.

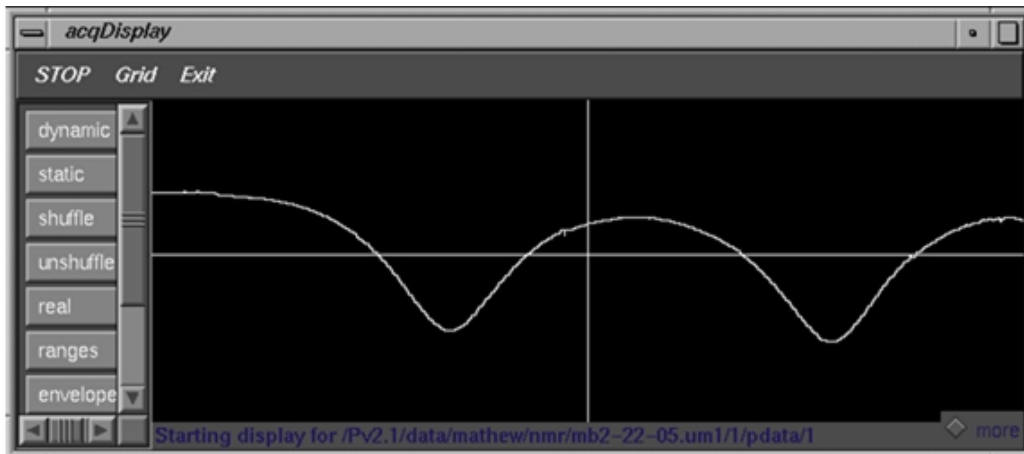


**Figure 7-17 - The resonance splitting in the magnet with  $50\Omega$  load connected to coil 2, note the X-axis is frequency and the Y-axis is the magnitude of the resonance.**

## 8. Conclusion

The development and testing of the prototype two-channel preamplifier has been successfully completed. This thesis provides an approach and a particular method for the design of the preamplifiers; it has outlined a generic methodology in an effort to aid in the future design of preamplifiers. This thesis details the steps of choosing the best operational transistor for the system specifications and ensuring that the transistor is unconditional stable at the frequency of operation. Secondly, the design of proper matching networks at the input and output of the transistor is explained to ensure that optimal performance will be obtained. The measured results collected from this analysis suggest that the designed preamplifier unit is sufficient and can be used in a multi-phased array system. Although this preamplifier satisfied all the requirements originally set forth in this thesis, changes could be administered to improve its performance in a phased array system.

### 8.1. Further Research

The two surface coils in conjunction with the dual stage preamplifier presented in this thesis are the basic building blocks for creating a phased array receiver system. Nevertheless, they are simple prototypes and some considerations need to be addressed to further improve their capabilities.

- Testing has shown that due to low quality inductors it appears counterproductive to use an input matching network to lower the noise figure. Thus, in future designs with this transistor, no input matching should be done and sufficient noise figures of around 0.7dB over the enter bandwidth can be obtained.

- The capacitance of  $C1$  and resistor  $R5$  could be reduced which would cause the preamplifier to have little or no recovery time. This could also be resolved by adding another resistor in series with the gate bias circuit between  $R5$  and  $L1$ . This resistor would be about  $50\Omega$  and another RF capacitor would need to be placed in between this new resistor and  $L1$  to ground. This and the reduction of  $R5$  would eliminate the recovery time issue and provide a low-frequency termination for the transistor to improve stability. If the echo time was then decreased, this could increase the quality of the received images due to the  $T_2$  relaxation decreasing exponentially.
- All inductors in the preamplifier could be potentially enlarged to 1210 sizes or larger. This increase in physical size would result in the inductors having higher quality factors, thus increasing the performance of the preamplifier.
- Further development in the coil design and layouts may increase the level of decoupling of the preamplifier. In addition, a different tri-coax cable with lower electric loss could be used to increase the signal strength.
- The last recommendation would be to upgrade the current configuration from a two-channel to a four-channel system in conjunction with redesigned coils.

## References

- [1] Bowick, Chris. *RF Circuit Design*. Oxford: Elsevier's Science 1982, pp. 66-74, 133-138.
- [2] de Zwart, Jacco A. "Optimization of a High Sensitivity MRI Receive Coil for Parallel Human Brain Imaging." Advanced MRI, LFMI, NINDS and LCE, 2002.
- [3] Gottlieb, Irving M. *RF Power Design Techniques*. New York: McGraw-Hill Inc, 1993.
- [4] Harter, Alponse. "LNA Matching Techniques for Optimizing Noise Figures." [www.rfdesign.com](http://www.rfdesign.com), 2003.
- [5] Hashemi, Ray H, William G. Bradley. *MRI, The Basics*. Baltimore: Williams & Wilkins, 1997.
- [6] Hornak, Joseph P. "The Basics of MRI." Rochester Institute of Technology, 2004. [www.cis.rit.edu/htbooks/mri/](http://www.cis.rit.edu/htbooks/mri/)
- [7] Howard, Andy. "Efficiently Simulating the Third Order Intercept Point of a Direct-conversion Receiver." [www.rfdesign.com/mag/radio\\_efficiently\\_simulating\\_thirdorder/](http://www.rfdesign.com/mag/radio_efficiently_simulating_thirdorder/)
- [8] Hurst, Gray, Lewis Meyer. *Analysis and Design of Analog Integrated Circuits*. 4<sup>th</sup> ed. New York: John Wiley & Sons, 2001, pp.758-760.
- [9] Jin, Jian-Ming. *Electromagnetic Analysis and Design in Magnetic Resonance Imaging*. Boca Raton: CRC Press, 1999.
- [10] Jin, Jian-Ming. "Electromagnetics in Magnetic Resonance Imaging." IEEE Antennas and Propagation Magazine, 1998, vol. 40, pp.7-21.
- [11] Keller, Paul J. "Basic Principles of Magnetic Resonance Imaging." Milwaukee: GE Medical Systems, 1991.
- [12] Leach, W, Marshall Jr. "Dr. Leach's Noise Potpourri." School of Electrical and Computer Engineering, Georgia Institute of Technology, 1999-2004. Ch.2&9.
- [13] Lee, Ray F, Randy O. Giaquinto, Christopher J. Hardy. "Coupling and Decoupling Theory and Its Application to the MRI Phased Array." Magnetic Resonance in Medicine, 2002, vol. 48, pp.203-213.
- [14] Ludwig, Reinhold, Pavel Bretchko. *RF Circuit Design*. New Jersey: Prentice Hall, 2000, pp. 470-476.



- [15] Macovski, Albert. "Noise in MRI." *Magnetic Resonance in Medicine*, 1996, vol. 36, pp.494-497.
- [16] Macchiarella, Giuseppe, Alessandro Raggi, Elipidio Di Lorenzo. "Design Criteria for Multistage Microwave Amplifiers with Match Requirements at Input and Output." *IEEE Transactions on Microwave Theory and Techniques*, 1993, vol.41, pp.1294-1298.
- [17] Nisnon, James W, Susan A. Riedel. *Electric Circuits*. New Jersey: Prentice Hall, 2001.
- [18] Ogan, Ocali, Ergin Atalar. "Ultimate Intrinsic Signal-to-Noise Ratio in MRI." *Magnetic Resonance in Medicine*, 1998, vol. 39, pp.462-473.
- [19] Pozar, David M. *Microwave Engineering*. 2<sup>nd</sup> ed. New York: John Wiley & Sons, 1998, pp. 612-618.
- [20] Puglia, K.V. "Electromagnetic Simulation of Some Common Balun Structures." *IEEE Microwave Magazine*. Sep 2002, pp.56-60.
- [21] Quick, Harald H, Mark E. Ladd, Gesine G. Zimmermann-Paul, Peter Erhart, Eugen Hofmann, Gustav K. Von Schulthess, Jorg F. Debatin. "Single-Loop Coil Concepts for Intravascular Magnetic Resonance Imaging." *Magnetic Resonance in Medicine*, 1999, vol.41, pp.751-758.
- [22] Reykowski, Arne, Steven M Wright, Jay R. Porter. "Design of Matching Networks for Low Noise Preamplifier." *Magnetic Resonance in Medicine*, 1995, vol.33, pp.848-852.
- [23] Sedra, Adel S, Kenneth C. Smith. *Microelectronic Circuits*. Oxford University Press. 1998.
- [24] Sorgenfrei, Birgit L. "Optimizing MRI Signal-to-Noise Ratio for Quadrature Unmatched RF Coils: Two Preamplifiers are Better than One." *Magnetic Resonance in Medicine*, 1996, vol.36, pp.104-110.
- [25] Ulaby, Fawwaz T. *Applied Electromagnetics*. New Jersey: Prentice Hall, 2001.
- [26] Vizmuller, Peter. *RF Design Guide: Systems, Circuits, and Equations*. Norwood: Artech House, 1995, pp.250-252.
- [27] Wosik, Jarek, L. M. Xie, M. Strikovski, M. Kamel, K. Nesteruk, M. Bilgen, P. A. Narayana. "High-Tc Superconducting RF Receiver Coil Arrays for Enhanced Field-of-View in an MRI System." *ISSO UHCL/UH*, 2000, pp.90-94.

- [28] Wright, Steven M. "Full-Wave Analysis of Planar Radiofrequency Coils and Coil Arrays with Assumed Current Distribution." Department of Electrical Engineering, Texas A&M University.
- [29] Wright, Steven M. "Phased Array Coils in MRS." Department of Electrical Engineering, Texas A&M University.
- [30] Wright, Steven M. "RF Coil Arrays for Magnetic Resonance Imaging." Engineering in Medicine and Biology, IEEE 1990, vol. 12, pp. 47-48.
- [31] Zhang, Pengfei. "Nonlinearity Test for a Fully Integrated Direct-Conversion Receiver." Microwave Journal, Oct. 2004, pp.94-112.

# Appendix A

## Simulated Results on the Resistive Biased Board

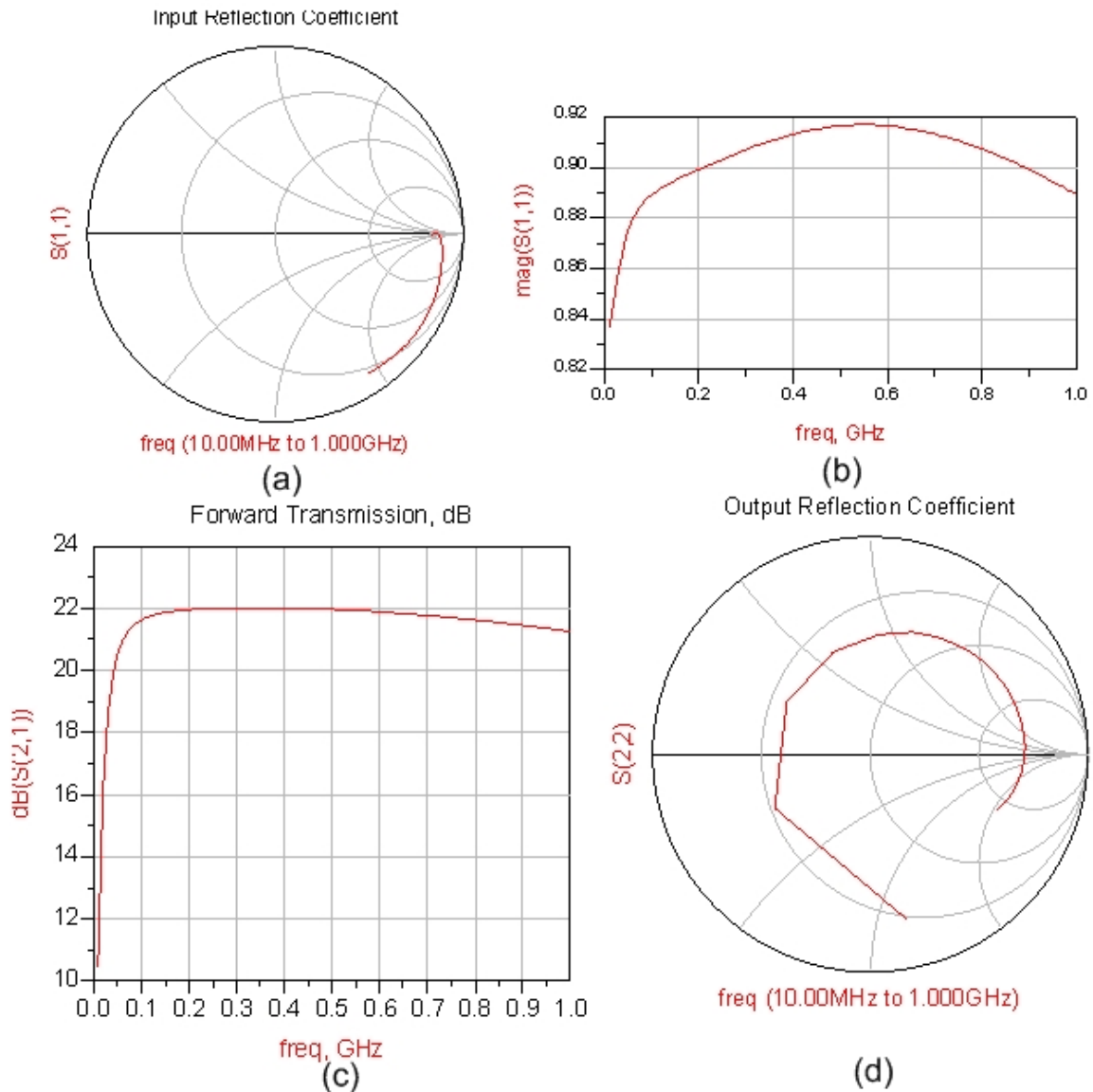


**Figure A-1 - Simulated Results-** (a)  $S_{11}$  displayed in the Smith Chart, (b)  $S_{11}$  in a magnitude scale,  $S_{21}$  in a dB scale, and (d)  $S_{22}$  displayed in the Smith Chart.

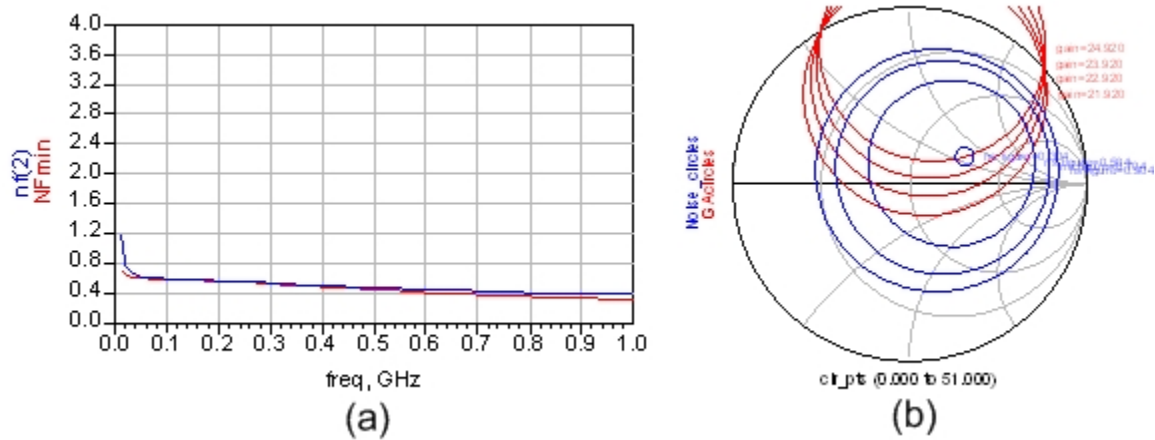


Figure A-2 - Simulated Results- (a) Noise figure in dB, and (b) Noise and gain circles in the Smith Chart.

## Measured Results on the Resistive Biased Board

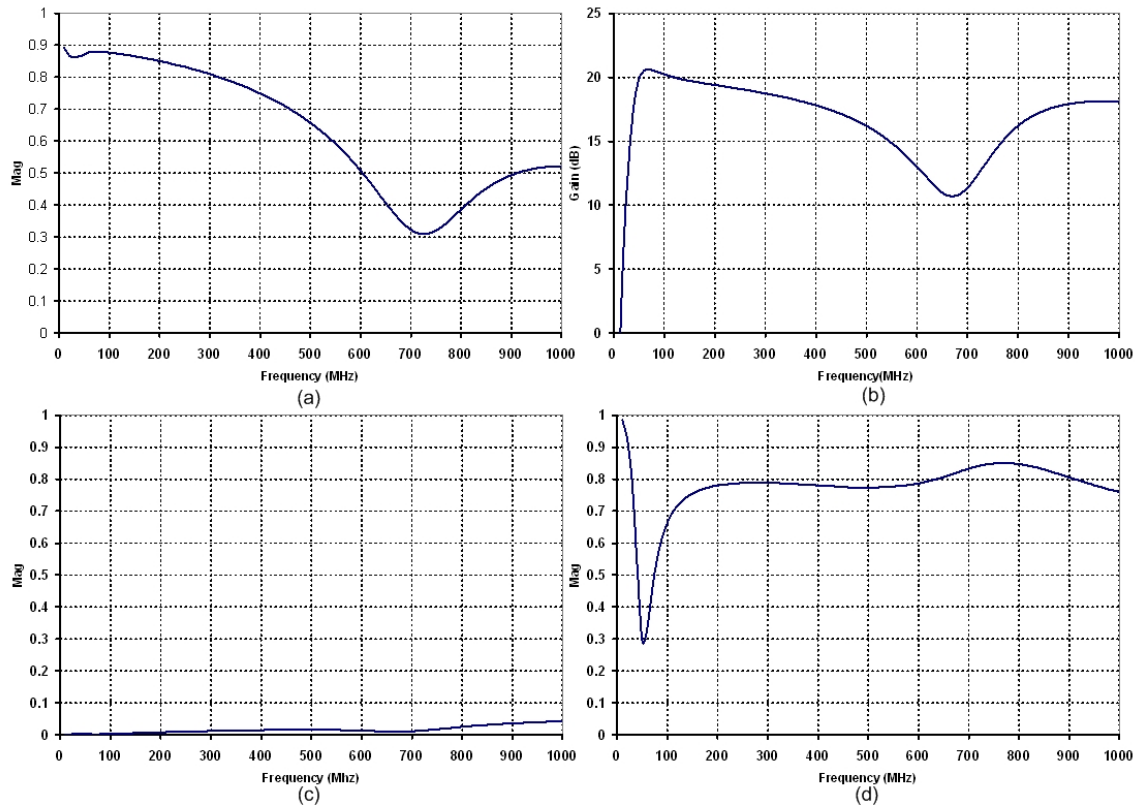
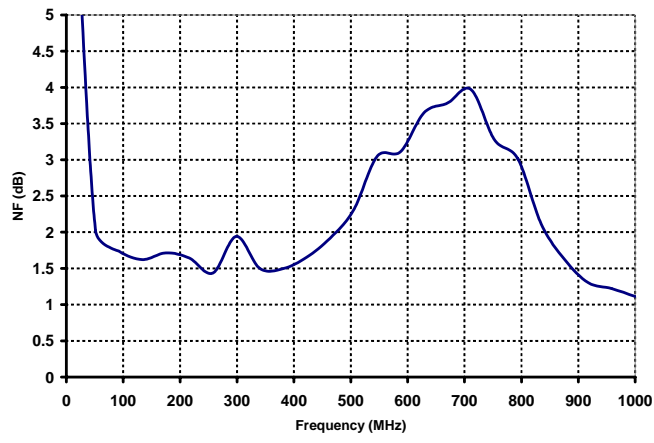
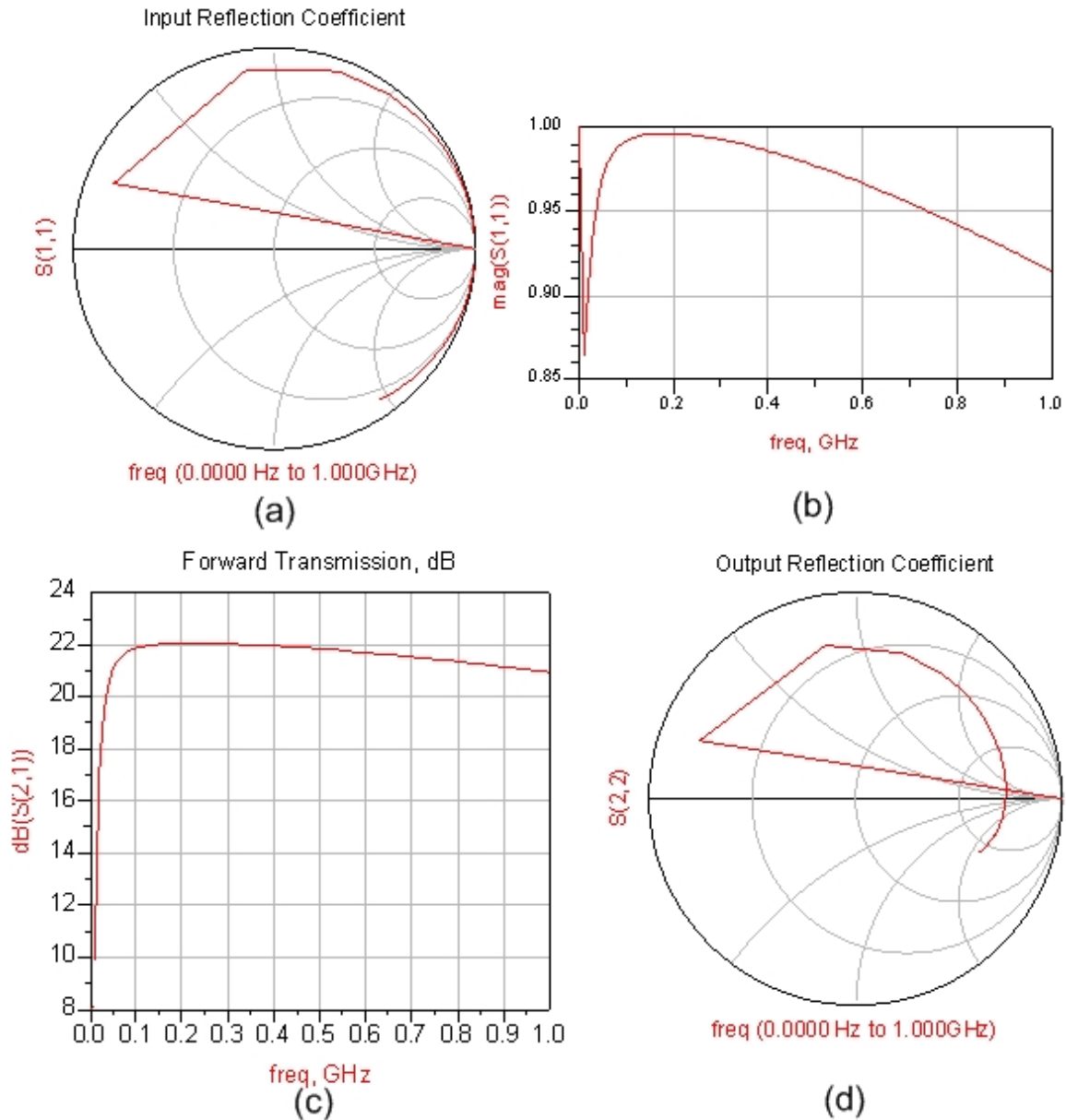


Figure A-3 - (a) S11, (b) S21, (c), S12 and (d) S22.



**Figure A-4 - Measured noise figure.**

## Simulated Results on the Active Biased Board



**Figure A-5 - Simulated Results-** (a)  $S_{11}$  displayed in the Smith Chart, (b)  $S_{11}$  in a magnitude scale,  $S_{21}$  in a dB scale, and (d)  $S_{22}$  displayed in the Smith Chart.

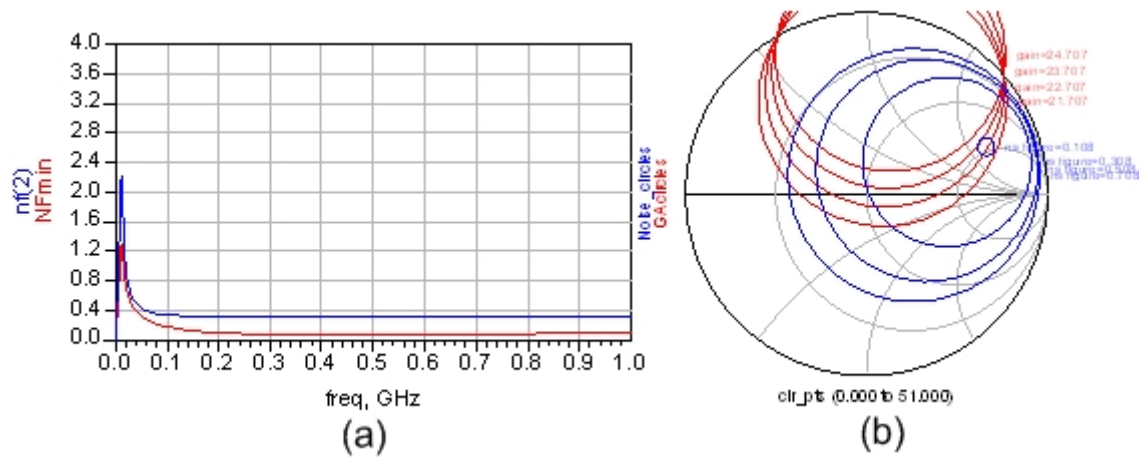


Figure A-6 - Simulated Results- (a) Noise figure in dB, and (b) Noise and gain circles in the Smith Chart.

## Measured Results on the Active Biased Board

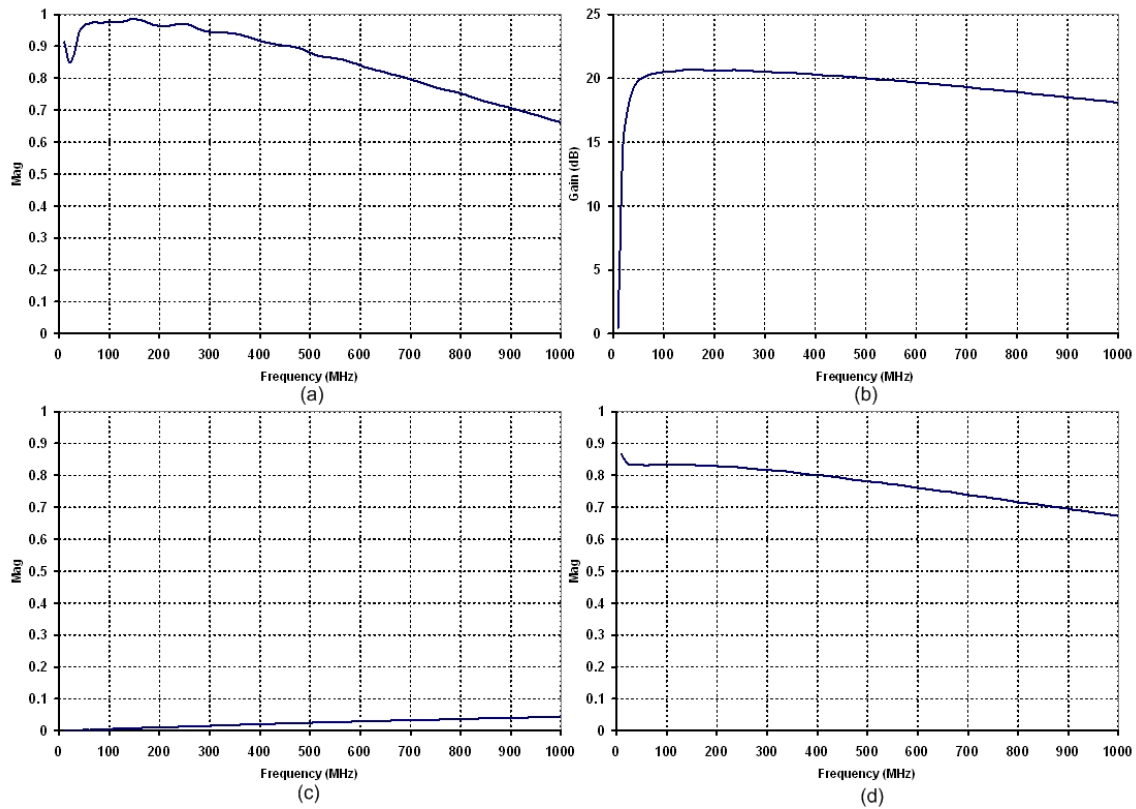


Figure A-7- (a) S11, (b) S21, (c), S12 and (d) S22.

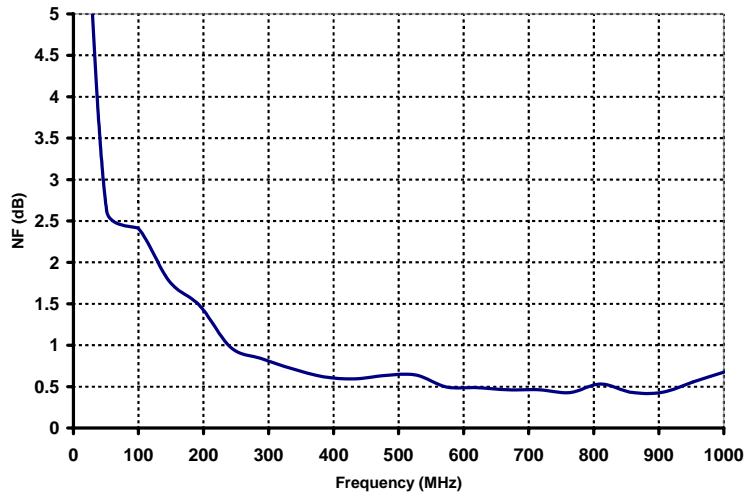


Figure A-8 - Measure noise figure.



# Appendix B

## Simulated Results on dual stage Boards

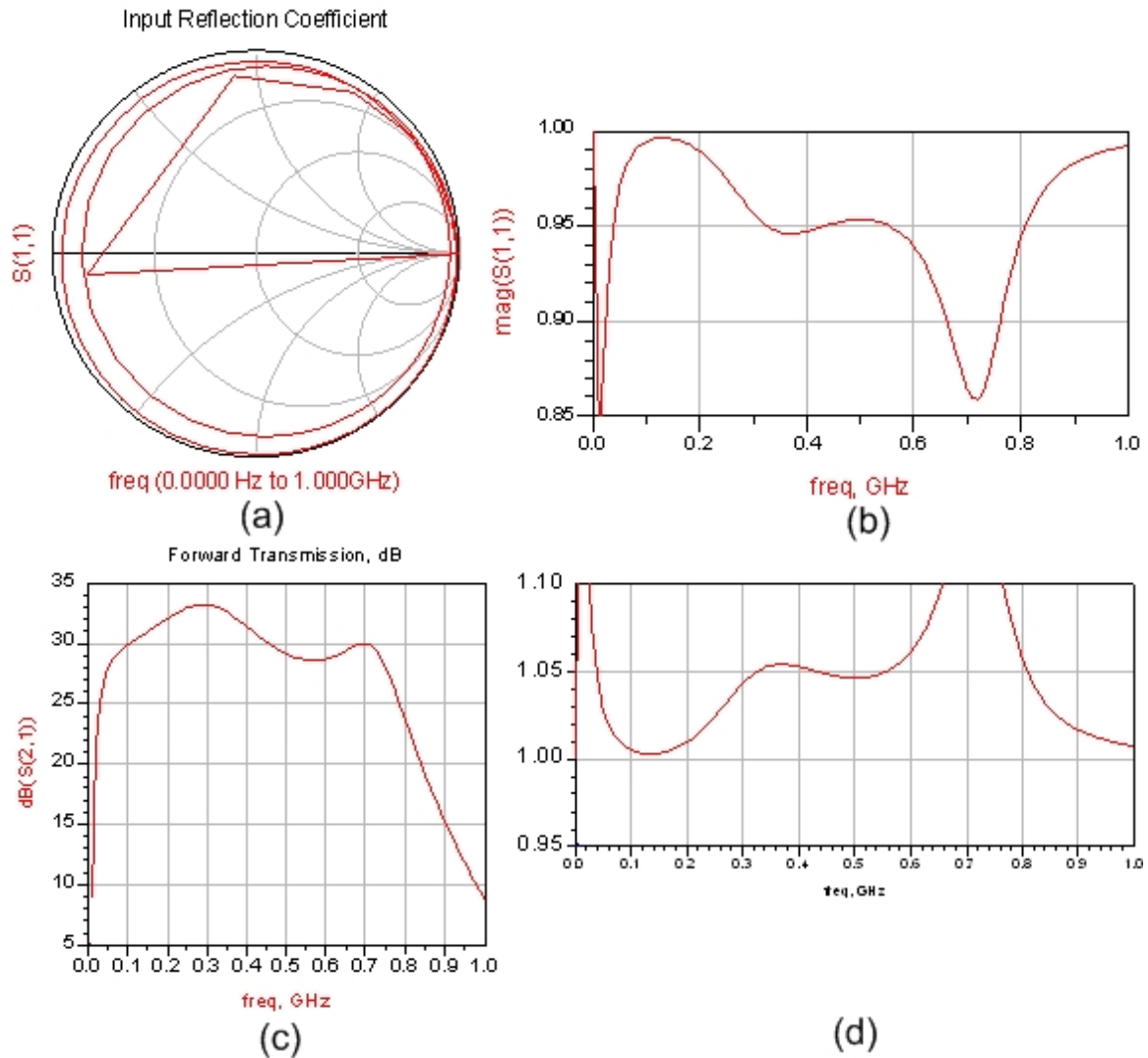
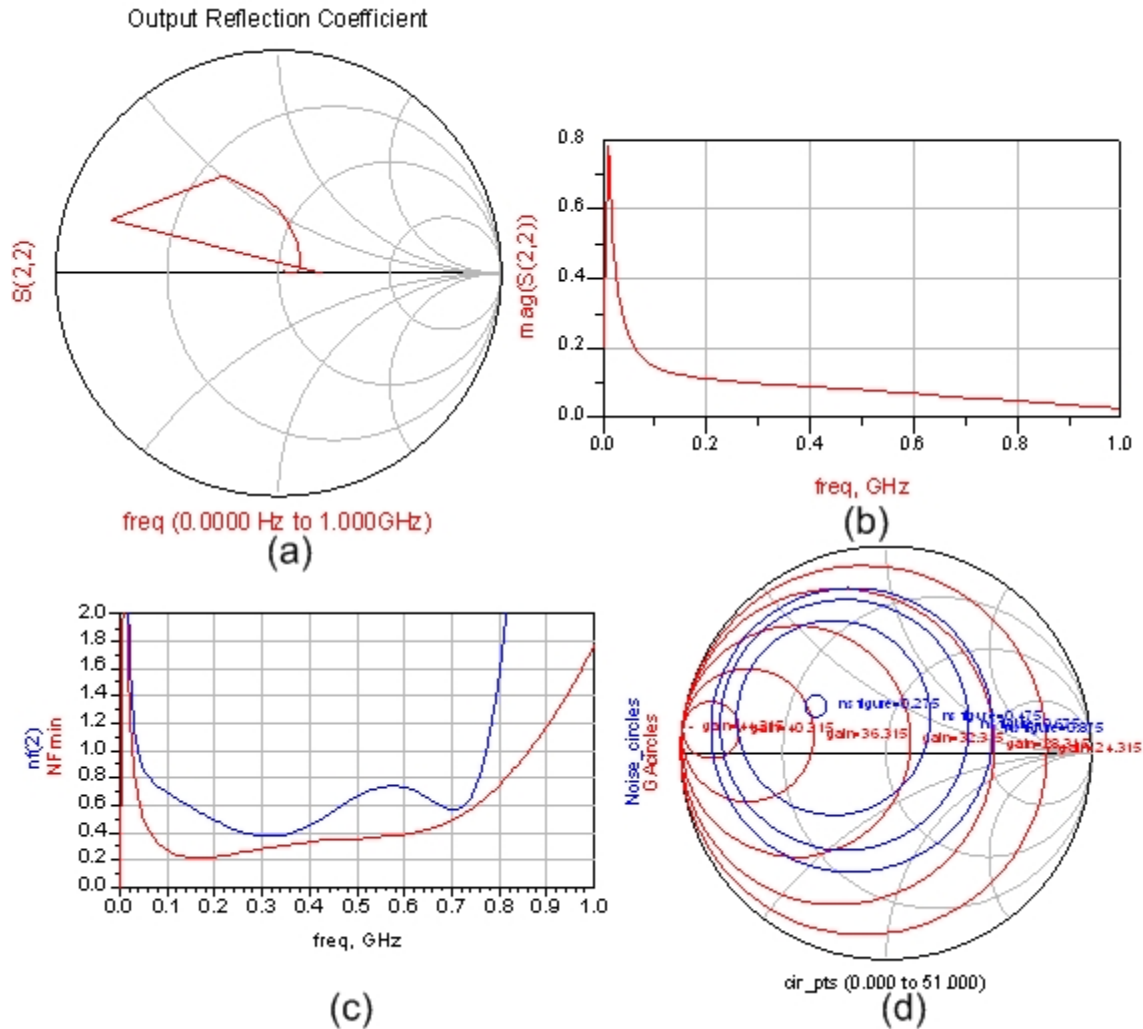


Figure B-1 - Simulated Results- (a)  $S_{11}$  displayed in the Smith Chart, (b)  $S_{11}$  in a magnitude scale,  $S_{21}$  in a dB scale, and (d) Stability over the frequency range above 1.



**Figure B-2 - Simulated Results- (a) S22 displayed in the Smith chart, (b) S22 plotted over frequency, (c) Noise figure in dB, and (d) Noise and gain circles in the Smith Chart.**

# Measured Results on the Dual stage Boards

Four dual stage boards were built with all data collected on each board seen below.

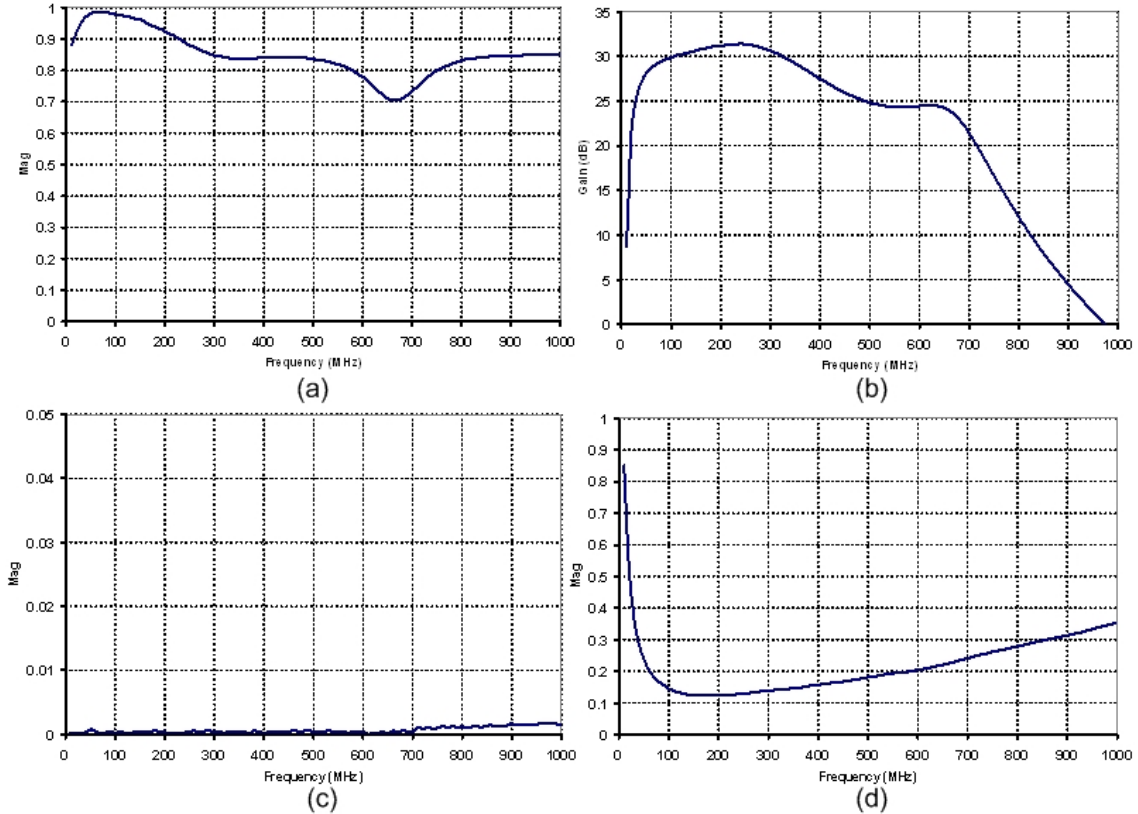


Figure B-3 – Measured results on board 1- (a) S11, (b) S21, (c), S12 and (d) S22.

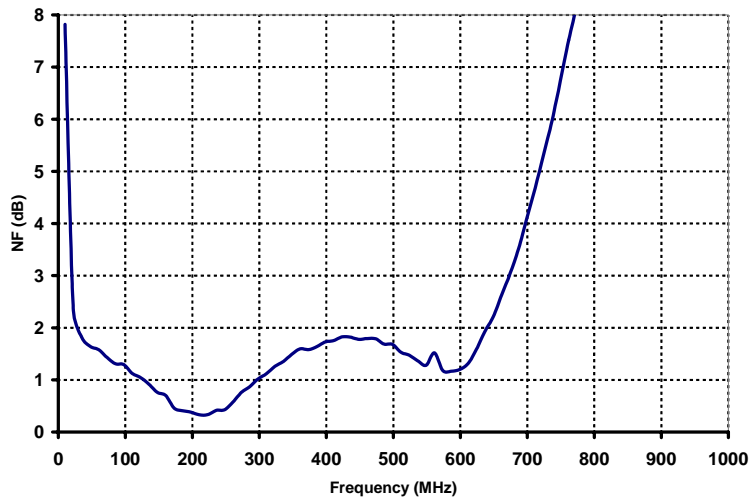


Figure B-4 - Measured noise figure on board 1.

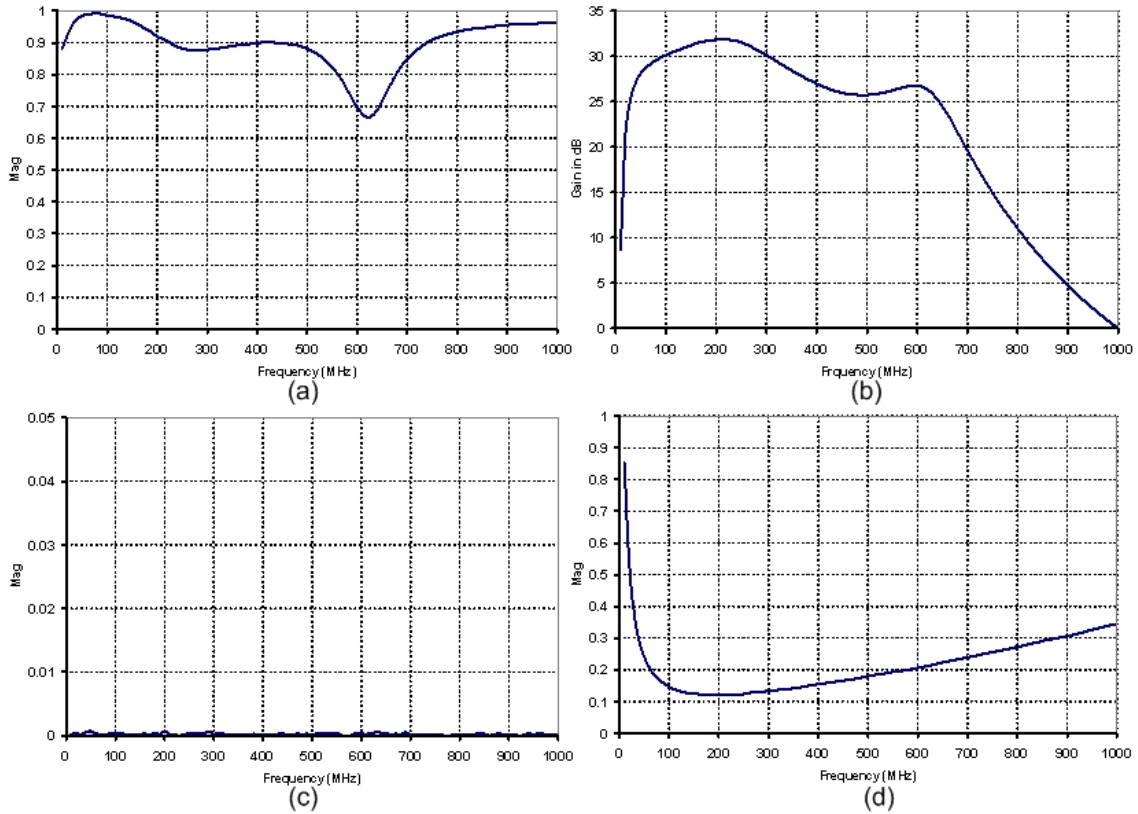


Figure B-5 – Measured results on board 2- (a) S11, (b) S21, (c), S12 and (d) S22.

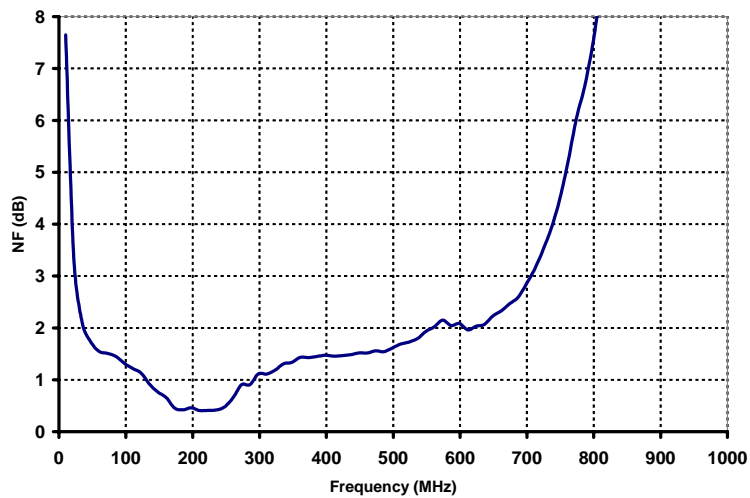
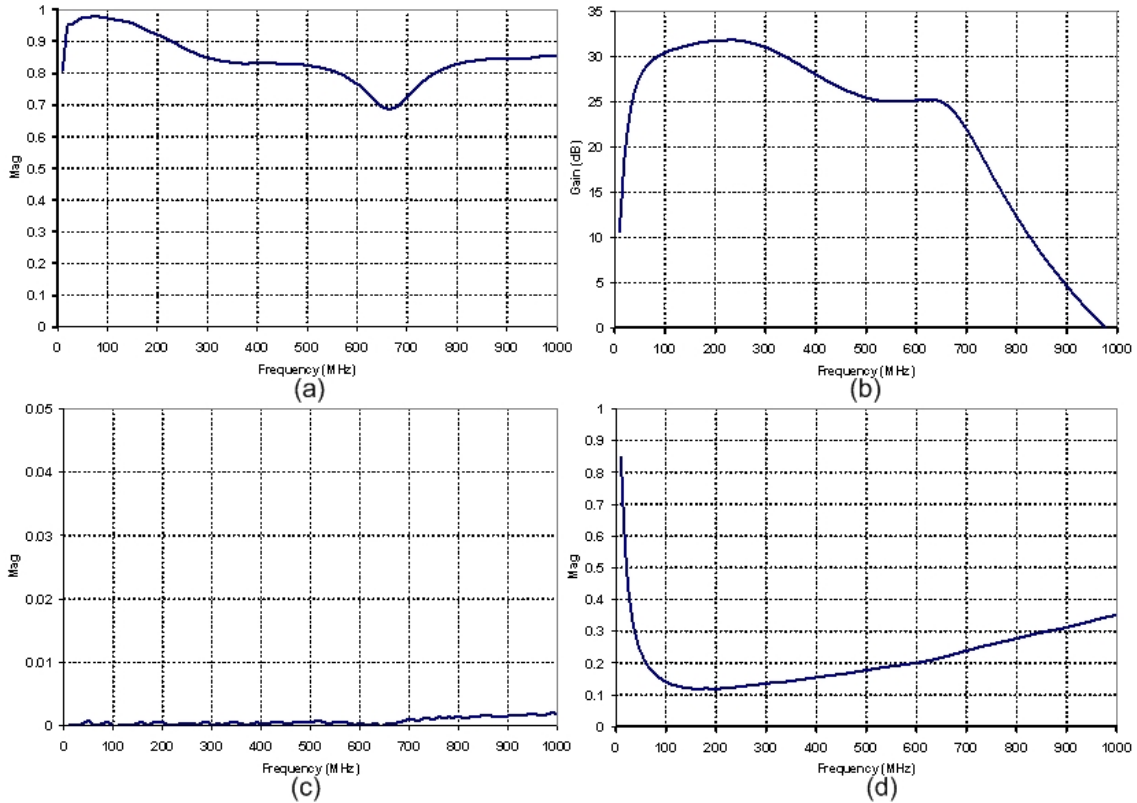
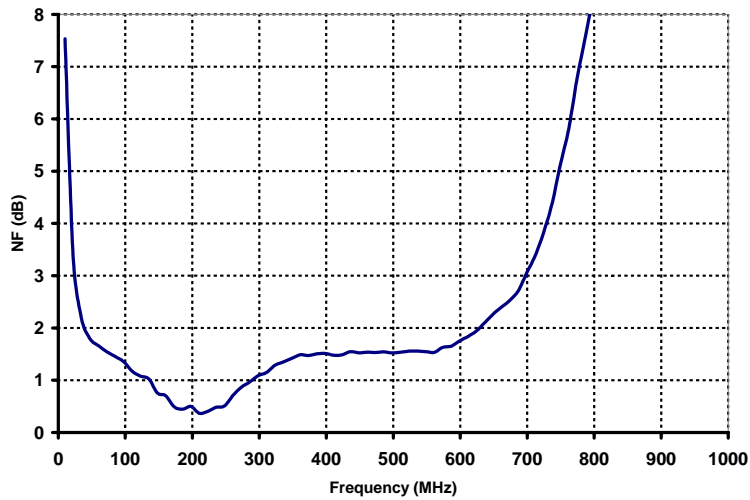


Figure B-6 - Measured noise figure on board 2.



**Figure B-7 – Measured results on board 3- (a) S11, (b) S21, (c), S12 and (d) S22.**



**Figure B-8 - Measured noise figure on board 3.**

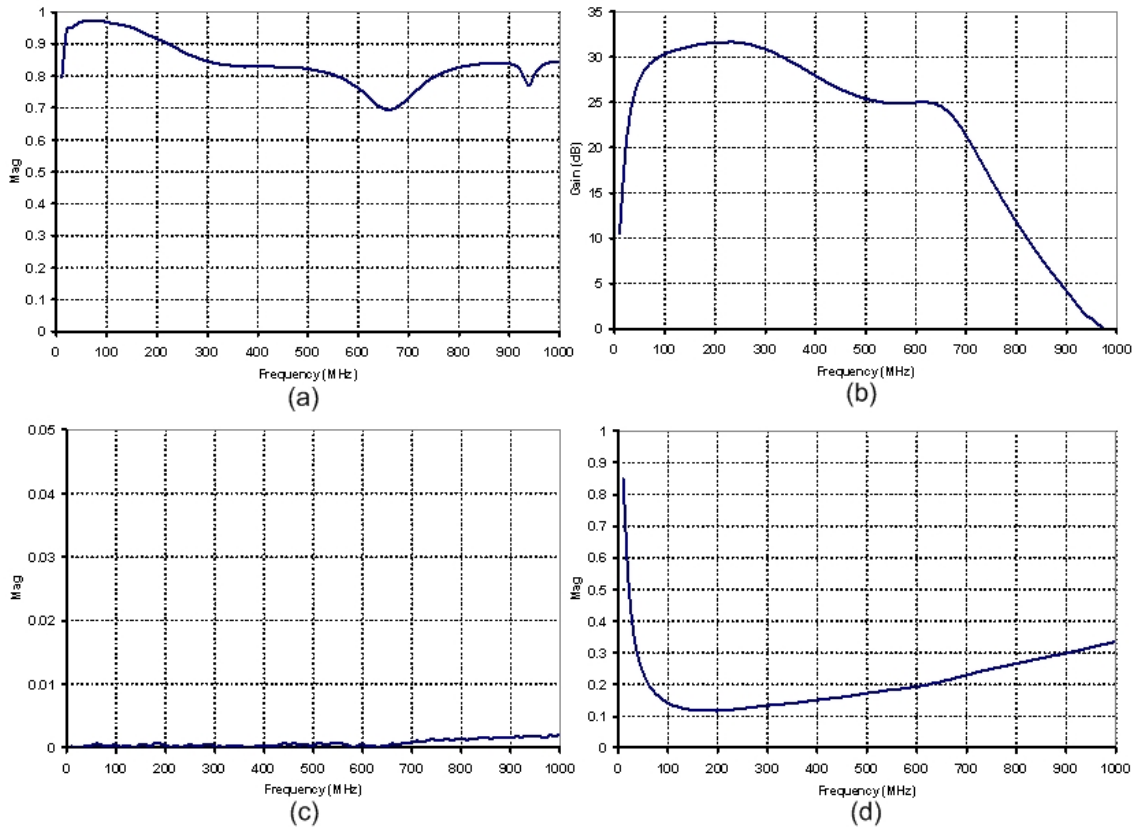


Figure B-9 – Measured results on board 4- (a) S11, (b) S21, (c), S12 and (d) S22.

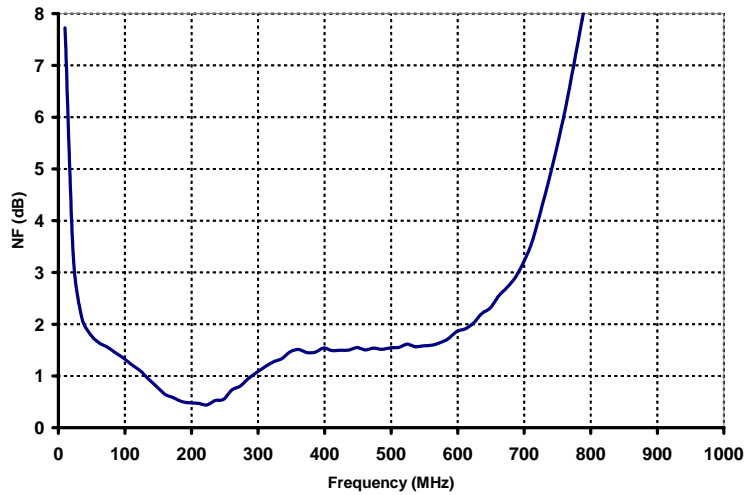


Figure B-10 - Measured noise figure on board 4.

## Appendix C

```
%John Kauffman
%ECE, WPI
%Summer 2004

%With the Amplifier being designed to have a bandwidth of 400MHz which is
%from 100-500MHz, Stability circles must be made and looked at all at once
%to make sure the system is stable. Also RF toolbox is needed to plot
%smith chart graphs.

global Z0;
global ZL;

set_Z0(50);
close all;
%-----
%Entering in all S-param from the data sheet on the ADF-551M4

%S parameters at 100MHz
S11_100M = 0.988 - 0.112*j;
S21_100M = -12.52 + 0.963*j;
S12_100M = 0.000376 + 0.005988*j;
S22_100M = 0.791 - 0.04426*j;

%S parameters at 500MHz
S11_500M = 0.811 - 0.491*j;
S21_500M = -10.88 + 4.644*j;
S12_500M = 0.008464 + 0.02458*j;
S22_500M = 0.745 - 0.195*j;

%-----

%Calculating Ds for all frequencies
%100MHz
Ds_100M = S11_100M*S22_100M - S12_100M*S21_100M;

%500MHz
Ds_500M = S11_500M*S22_500M - S12_500M*S21_500M;

%-----

%conj() is the command for complex conjugate

%Now finding the locations and radaii of the input and output stability
circles
%INPUT CIRCLES

%100MHz
C1_100M = S11_100M - (Ds_100M*conj(S22_100M));
%center location
rs1_100M = conj(C1_100M)/((abs(S11_100M))^2 - (abs(Ds_100M))^2);
%radius
ps1_100M = abs((S12_100M*S21_100M)/((abs(S11_100M))^2-(abs(Ds_100M))^2));

%500MHz
C1_500M = S11_500M - (Ds_500M*conj(S22_500M));
%center location
rs1_500M = conj(C1_500M)/((abs(S11_500M))^2 - (abs(Ds_500M))^2);
%radius
ps1_500M = abs((S12_500M*S21_500M)/((abs(S11_500M))^2-(abs(Ds_500M))^2));
```

```

%OUTPUT CIRCLES

%100MHz
C2_100M = S22_100M - (Ds_100M*conj(S11_100M));
%center location
rs2_100M = conj(C2_100M)/((abs(S22_100M))^2 - (abs(Ds_100M))^2);
%radius
ps2_100M = abs((S12_100M*S21_100M)/((abs(S22_100M))^2-(abs(Ds_100M))^2));

%500MHz
C2_500M = S22_500M - (Ds_500M*conj(S11_500M));
%center location
rs2_500M = conj(C2_500M)/((abs(S22_500M))^2 - (abs(Ds_500M))^2);
%radius
ps2_500M = abs((S12_500M*S21_500M)/((abs(S22_500M))^2-(abs(Ds_500M))^2));

%-----
%Plotting Input and Output Stability circles
angle= (0:0.01:1)*2*pi;

% Input smith chart
smith_chart;
hold on;
plot( real(rs1_100M)+ps1_100M*cos(angle),imag(rs1_100M)+ps1_100M*sin*
(angle));
plot( real(rs1_500M)+ps1_500M*cos(angle),imag(rs1_500M)+ps1_500M*sin*
(angle));
plot(real(S11_100M), imag(S11_100M),'ro');
text(real(S11_100M), imag(S11_100M),'\leftarrow 100MHz');
plot(real(S11_500M), imag(S11_500M),'bo');
text(real(S11_500M), imag(S11_500M),'\leftarrow 500MHz');
title('Input Stability Circles');
hold off;

%Output smith chart
smith_chart;
hold on;
plot( real(rs2_100M)+ps2_100M*cos(angle),imag(rs2_100M)+ps2_100M*sin*
(angle));
plot( real(rs2_500M)+ps2_500M*cos(angle),imag(rs2_500M)+ps2_500M*sin*
(angle));
plot(real(S22_100M), imag(S22_100M),'ro');
text(real(S22_100M), imag(S22_100M),'\leftarrow 100MHz');
plot(real(S22_500M), imag(S22_500M),'bo');
text(real(S22_500M), imag(S22_500M),'\leftarrow 500MHz');
title('Output Stability Circles');
hold off;

%Applying Attenuator to push input and output stability circles out of
%Smith Chart.

Atten= 11.68; % in dB

[theta,ruo] = cart2pol(real(S21_100M),imag(S21_100M));
ruo = ruo-Atten;

```



```

[X,Y] = pol2cart(theta,ruo);
S21_100M= X+Y*i;
[theta,ruo] = cart2pol(real(S21_500M),imag(S21_500M));
ruo = ruo-Atten;
[X,Y] = pol2cart(theta,ruo);
S21_500M= X+Y*i;

S22_100M=0;
S22_500M=0;

%-----

%Calculating Ds for all frequencies
%100MHz
Ds_100M = S11_100M*S22_100M - S12_100M*S21_100M;

%500MHz
Ds_500M = S11_500M*S22_500M - S12_500M*S21_500M;

%-----

%conj() is the command for complex conjugate

%Now finding the locations and radaii of the input and output stability*
circles
%INPUT CIRCLES

%100MHz
C1_100M = S11_100M - (Ds_100M*conj(S22_100M));
%center location
rs1_100M = conj(C1_100M)/((abs(S11_100M))^2 - (abs(Ds_100M))^2);
%radius
ps1_100M = abs((S12_100M*S21_100M)/((abs(S11_100M))^2-(abs(Ds_100M))^2));

%500MHz
C1_500M = S11_500M - (Ds_500M*conj(S22_500M));
%center location
rs1_500M = conj(C1_500M)/((abs(S11_500M))^2 - (abs(Ds_500M))^2);
%radius
ps1_500M = abs((S12_500M*S21_500M)/((abs(S11_500M))^2-(abs(Ds_500M))^2));

%OUTPUT CIRCLES

%100MHz
C2_100M = S22_100M - (Ds_100M*conj(S11_100M));
%center location
rs2_100M = conj(C2_100M)/((abs(S22_100M))^2 - (abs(Ds_100M))^2);
%radius
ps2_100M = abs((S12_100M*S21_100M)/((abs(S22_100M))^2-(abs(Ds_100M))^2));

%500MHz
C2_500M = S22_500M - (Ds_500M*conj(S11_500M));
%center location
rs2_500M = conj(C2_500M)/((abs(S22_500M))^2 - (abs(Ds_500M))^2);
%radius
ps2_500M = abs((S12_500M*S21_500M)/((abs(S22_500M))^2-(abs(Ds_500M))^2));

%-----

```

```

%Plotting Input and Output Stability circles
angle= (0:0.01:1)*2*pi;

% Input smith chart
smith_chart;
hold on;
plot( real(rs1_100M)+ps1_100M*cos(angle),imag(rs1_100M)+ps1_100M*sin
(angle));
plot( real(rs1_500M)+ps1_500M*cos(angle),imag(rs1_500M)+ps1_500M*sin
(angle));
plot(real(S11_100M), imag(S11_100M),'ro');
text(real(S11_100M), imag(S11_100M),'\leftarrow 100MHz');
plot(real(S11_500M), imag(S11_500M),'bo');
text(real(S11_500M), imag(S11_500M),'\leftarrow 500MHz');
title('Unconditional Input Stability Circles');
hold off;

%Output smith chart
smith_chart;
hold on;
plot( real(rs2_100M)+ps2_100M*cos(angle),imag(rs2_100M)+ps2_100M*sin
(angle));
plot( real(rs2_500M)+ps2_500M*cos(angle),imag(rs2_500M)+ps2_500M*sin
(angle));
title('Unconditional Output Stability Circles');
hold off;

```

# Appendix D



## Agilent ATF-551M4 Low Noise Enhancement Mode Pseudomorphic HEMT in a Miniature Leadless Package Data Sheet

### Description

Agilent Technologies' ATF-551M4 is a high dynamic range, super low noise, single supply E-pHEMT GaAs FET housed in a thin miniature leadless package.

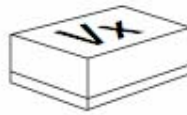
The combination of small device size, super low noise (under 1 dB Fmin from 2 to 6 GHz), high linearity and low power makes the ATF-551M4 ideal for LNA or hybrid module designs in wireless receiver in the 450 MHz to 10 GHz frequency band.

Applications include Cellular/PCS/WCDMA handsets and data modem cards, fixed wireless infrastructure in the 2.4, 3.5 GHz and UNII frequency bands, as well as 2.4 GHz 802.11b, 5 GHz 802.11a and HIPERLAN/2 Wireless LAN PC-cards.

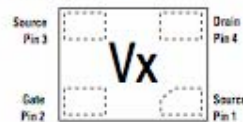
### Note:

1. Agilent's enhancement mode E-pHEMT devices are the first commercially available single-supply GaAs transistors that do not need a negative gate bias voltage for operation. They can help simplify the design and reduce the cost of receivers and transmitters in many applications in the 450 MHz to 10 GHz frequency range.

### MiniPak 1.4 mm x 1.2 mm Package



### Pin Connections and Package Marking



### Note:

Top View: Package marking provides orientation, product identification and date code.

"V" = Device Type Code

"x" = Date code character. A different character is assigned for each month and year.

### Features

- Very low noise figure and high linearity
- Single Supply Enhancement Mode Technology<sup>1)</sup> optimized for 3V operation
- Excellent uniformity in product specifications
- 400 micron gate width
- Thin miniature package 1.4 mm x 1.2 mm x 0.7 mm
- Tape-and-reel packaging option available

### Specifications

- 2 GHz; 2.7V, 10 mA (typ.)
- 24.1 dBm output 3<sup>rd</sup> order intercept
- 14.6 dBm output power at 1 dB gain compression
- 0.5 dB noise figure
- 17.5 dB associated gain

### Applications

- Low Noise Amplifier for:
  - Cellular/PCS/WCDMA handsets and modem cards
  - 2.4 GHz, 3.5 GHz and UNII fixed wireless infrastructure
  - 2.4 GHz 802.11b Wireless LAN
  - 5 GHz 802.11a and HIPERLAN Wireless LAN
- General purpose discrete E-pHEMT for other ultra low noise applications



### ATF-551M4 Absolute Maximum Ratings<sup>(1)</sup>

Symbol	Parameter	Units	Absolute Maximum
$V_{DS}$	Drain-Source Voltage <sup>(2)</sup>	V	5
$V_{GS}$	Gate-Source Voltage <sup>(2)</sup>	V	-5 to 1
$V_{GD}$	Gate Drain Voltage <sup>(2)</sup>	V	-5 to 1
$I_{DS}$	Drain Current <sup>(2)</sup>	mA	100
$I_{GS}$	Gate Current <sup>(2)</sup>	mA	1
$P_{Diss}$	Total Power Dissipation <sup>(3)</sup>	mW	270
$P_{in,max}$	RF Input Power	dBm	+10
$T_{Ch}$	Channel Temperature	°C	150
$T_{Stg}$	Storage Temperature	°C	-65 to 150
$\theta_{JC}$	Thermal Resistance <sup>(4)</sup>	°C/W	240

#### Notes:

1. Operation of this device above any one of these parameters may cause permanent damage.
2. Assumes DC quiescent conditions.
3. Source lead temperature is 25°C. Derate 6 mW/°C for  $T_C > 40^\circ\text{C}$ .
4. Thermal resistance measured using 150°C Liquid Crystal Measurement method.
5. Device can safely handle +10 dBm RF Input Power provided  $I_{DS}$  is limited to 1 mA.  $I_{DS}$  at  $P_{in}$  drive RF level is bias circuit dependent. See applications section for additional information.

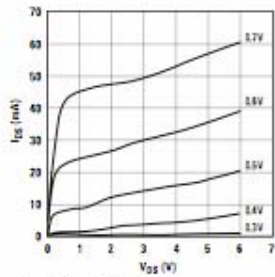


Figure 1. Typical I-V Curves.  
( $V_{DS} = 0.1$  V per step)

### Product Consistency Distribution Charts<sup>(6)</sup>

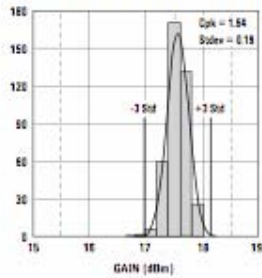


Figure 2. Capability Plot for Gain @ 2.7 V, 10 mA. LSL = 15.5, Nominal = 17.5, USL = 18.5

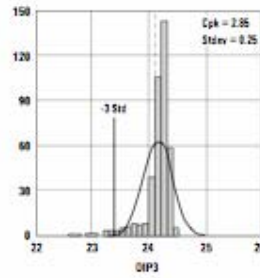


Figure 3. Capability Plot for OIP3 @ 2.7 V, 10 mA. LSL = 22.0, Nominal = 24.1

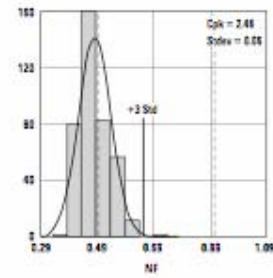


Figure 4. Capability Plot for NF @ 2.7 V, 10 mA. Nominal = 0.5, USL = 0.9

#### Note:

6. Distribution data sample size is 398 samples taken from 4 different wafers. Future wafers allocated to this product may have nominal values anywhere between the upper and lower limits. Measurements made on production test board. This circuit represents a trade-off between an optimal noise match and a realizable match based on production test equipment. Circuit losses have been de-embedded from actual measurements.

### ATF-551M4 Electrical Specifications

$T_A = 25^\circ\text{C}$ , RF parameters measured in a test circuit for a typical device

Symbol	Parameter and Test Condition	Units	Min.	Typ.	Max.		
$V_{gs}$	Operational Gate Voltage	$V_{ds} = 2.7\text{V}, I_{ds} = 10\text{ mA}$	V	0.3	0.47	0.65	
$V_{th}$	Threshold Voltage	$V_{ds} = 2.7\text{V}, I_{ds} = 2\text{ mA}$	V	0.18	0.37	0.53	
$I_{dss}$	Saturated Drain Current	$V_{ds} = 2.7\text{V}, V_{gs} = 0\text{V}$	$\mu\text{A}$	—	0.1	3	
$g_m$	Transconductance	$V_{ds} = 2.7\text{V}, g_m = \Delta I_{dss} / \Delta V_{gs}; \Delta V_{gs} = 0.75 - 0.7 = 0.05\text{V}$	mmho	110	220	285	
$I_{gss}$	Gate Leakage Current	$V_{gd} = V_{gs} = -2.7\text{V}$	$\mu\text{A}$	—	—	95	
NF	Noise Figure <sup>[1]</sup>	$f = 2\text{ GHz}$	$V_{ds} = 2.7\text{V}, I_{ds} = 10\text{ mA}$	dB	—	0.5	0.9
			$V_{ds} = 3\text{V}, I_{ds} = 20\text{ mA}$	dB	—	0.5	—
Gain	Gain <sup>[1]</sup>	$f = 2\text{ GHz}$	$V_{ds} = 2.7\text{V}, I_{ds} = 10\text{ mA}$	dB	15.5	17.5	18.5
			$V_{ds} = 3\text{V}, I_{ds} = 20\text{ mA}$	dB	—	18.0	—
OIP3	Output 3 <sup>rd</sup> Order Intercept Point <sup>[1]</sup>	$f = 2\text{ GHz}$	$V_{ds} = 2.7\text{V}, I_{ds} = 10\text{ mA}$	dBm	22	24.1	—
			$V_{ds} = 3\text{V}, I_{ds} = 20\text{ mA}$	dBm	—	30.0	—
P1dB	1dB Compressed Output Power <sup>[1]</sup>	$f = 2\text{ GHz}$	$V_{ds} = 2.7\text{V}, I_{ds} = 10\text{ mA}$	dBm	—	14.6	—
			$V_{ds} = 3\text{V}, I_{ds} = 20\text{ mA}$	dBm	—	16.0	—

#### Notes:

1. Measurements obtained using production test board described in Figure 5. Typical values were determined from a sample size of 395 parts from 4 wafers.



Figure 5. Block diagram of 2 GHz production test board used for Noise Figure, Gain, P1dB, OIP3, and IIP3 measurements. This circuit represents a trade-off between an optimal noise match, maximum OIP3 match and associated impedance matching circuit losses. Circuit losses have been de-embedded from actual measurements.

### ATF-551M4 Electrical Specifications (see notes 2 and 3, as indicated)

Symbol	Parameter and Test Condition	Units	Min.	Typ.	Max.		
Fmin	Minimum Noise Figure <sup>[2]</sup>	$f = 900\text{ GHz}$	$V_{ds} = 2.7\text{V}, I_{ds} = 10\text{ mA}$	dB	—	0.27	—
		$f = 2\text{ GHz}$	$V_{ds} = 2.7\text{V}, I_{ds} = 10\text{ mA}$	dB	—	0.41	—
		$f = 3.9\text{ GHz}$	$V_{ds} = 2.7\text{V}, I_{ds} = 10\text{ mA}$	dB	—	0.61	—
		$f = 5.8\text{ GHz}$	$V_{ds} = 2.7\text{V}, I_{ds} = 10\text{ mA}$	dB	—	0.88	—
Ga	Associated Gain <sup>[2]</sup>	$f = 900\text{ GHz}$	$V_{ds} = 2.7\text{V}, I_{ds} = 10\text{ mA}$	dB	—	21.8	—
		$f = 2\text{ GHz}$	$V_{ds} = 2.7\text{V}, I_{ds} = 10\text{ mA}$	dB	—	17.9	—
		$f = 3.9\text{ GHz}$	$V_{ds} = 2.7\text{V}, I_{ds} = 10\text{ mA}$	dB	—	14.2	—
		$f = 5.8\text{ GHz}$	$V_{ds} = 2.7\text{V}, I_{ds} = 10\text{ mA}$	dB	—	12.0	—
OIP3	Output 3 <sup>rd</sup> Order Intercept Point <sup>[3]</sup>	$f = 900\text{ GHz}$	$V_{ds} = 2.7\text{V}, I_{ds} = 10\text{ mA}$	dBm	—	22.1	—
		$f = 3.9\text{ GHz}$	$V_{ds} = 2.7\text{V}, I_{ds} = 10\text{ mA}$	dBm	—	24.3	—
		$f = 5.8\text{ GHz}$	$V_{ds} = 2.7\text{V}, I_{ds} = 10\text{ mA}$	dBm	—	24.5	—
P1dB	1dB Compressed Output Power <sup>[3]</sup>	$f = 900\text{ GHz}$	$V_{ds} = 2.7\text{V}, I_{ds} = 10\text{ mA}$	dBm	—	14.3	—
		$f = 3.9\text{ GHz}$	$V_{ds} = 2.7\text{V}, I_{ds} = 10\text{ mA}$	dBm	—	14.5	—
		$f = 5.8\text{ GHz}$	$V_{ds} = 2.7\text{V}, I_{ds} = 10\text{ mA}$	dBm	—	14.3	—

#### Notes:

2. The Fmin values are based on a set of 16 noise figure measurements made at 16 different impedances using an ATN NP5 test system. From these measurements Fmin is calculated. Refer to the noise parameter measurement section for more information.

3. Measurements taken above and below 2 GHz was made using a double stub tuner at the input tuned for low noise and a double stub tuner at the output tuned for maximum OIP3. Circuit losses have been de-embedded from actual measurements.



ATF-551M4 Typical Performance Curves

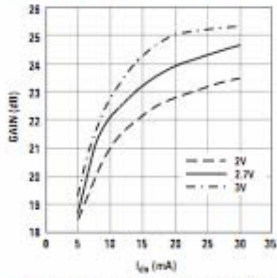


Figure 6. Gain vs.  $I_{dq}$  and  $V_{ds}$  at 900 MHz<sup>[1]</sup>.

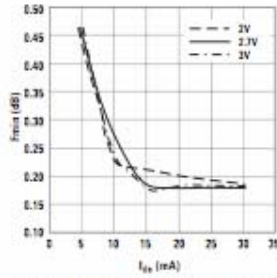


Figure 7.  $F_{min}$  vs.  $I_{dq}$  and  $V_{ds}$  at 900 MHz<sup>[2]</sup>.

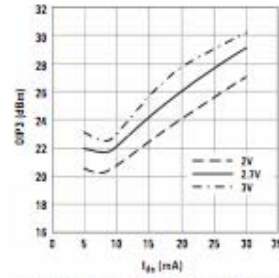


Figure 8. OIP3 vs.  $I_{dq}$  and  $V_{ds}$  at 900 MHz<sup>[1]</sup>.

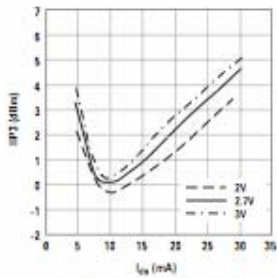


Figure 9. IIP3 vs.  $I_{dq}$  and  $V_{ds}$  at 900 MHz<sup>[1]</sup>.

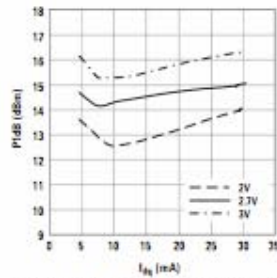


Figure 10. P1dB vs.  $I_{dq}$  and  $V_{ds}$  at 900 MHz<sup>[1]</sup>.

Notes:

1. Measurements at 900MHz were made using an ICM fixture with a double stub tuner at the input tuned for low noise and a double stub tuner at the output tuned for maximum OIP3. Circuit losses have been de-embedded from actual measurements.
2. The  $F_{min}$  values are based on a set of 16 noise figure measurements made at 15 different impedances using an ATN NP5 test system. From these measurements  $F_{min}$  is calculated. Refer to the noise parameter measurement section for more information.
3. P1dB measurements are performed with passive biasing. Quiescent drain current,  $I_{dsq}$ , is set with zero RF drive applied. As P1dB is approached, the drain current may increase or point. At lower values of  $I_{dsq}$ , the device is running close to class B as power output approaches P1dB. This results in higher P1dB and higher PAE (power added efficiency) when compared to a device that is driven by a constant current source as is typically done with active biasing. As an example, at a  $V_{DS} = 2.7V$  and  $I_{dsq} = 5\text{ mA}$ ,  $I_d$  increases to 15 mA as a P1dB of +14.5 dBm is approached.

ATF-551M4 Typical Performance Curves, continued

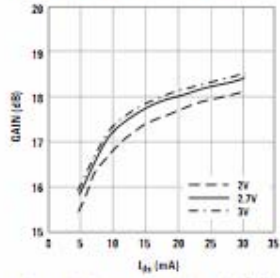


Figure 11. Gain vs.  $I_{dq}$  and  $V_{ds}$  at 2 GHz<sup>[1]</sup>.

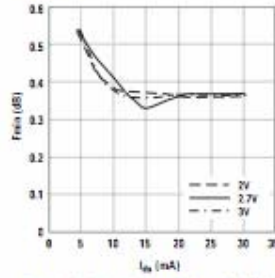


Figure 12.  $F_{min}$  vs.  $I_{dq}$  and  $V_{ds}$  at 2 GHz<sup>[2]</sup>.

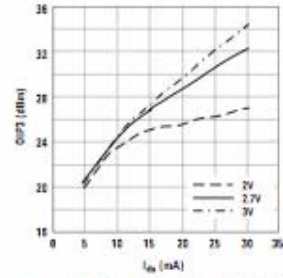


Figure 13. OIP3 vs.  $I_{dq}$  and  $V_{ds}$  at 2 GHz<sup>[1]</sup>.

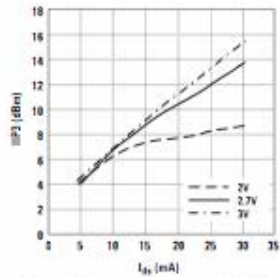


Figure 14. IIP3 vs.  $I_{dq}$  and  $V_{ds}$  at 2 GHz<sup>[1]</sup>.

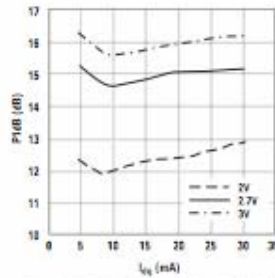


Figure 15. P1dB vs.  $I_{dq}$  and  $V_{ds}$  at 2 GHz<sup>[1]</sup>.

Notes:

1. Measurements at 2 GHz with biasing 2.7V, 10 mA were made on a fixed tuned production test board that was tuned for optimal OIP3 match with reasonable noise figure. This circuit represents a trade-off between optimal noise match, maximum OIP3 match and a realizable match based on production test board requirements. Measurements taken other than 2.7V, 10 mA biasing was made using a double stub tuner at the input tuned for low noise and a double stub tuner at the output tuned for maximum OIP3. Circuit losses have been de-embedded from actual measurements.
2. The  $F_{min}$  values are based on a set of 16 noise figure measurements made at 16 different impedances using an ATN NP5 test system. From these measurements  $F_{min}$  is calculated. Refer to the noise parameter measurement section for more information.
3. P1dB measurements are performed with passive biasing. Quiescent drain current,  $I_{dq}$ , is set with zero RF drive applied. As P1dB is approached, the drain current may increase or point. At lower values of  $I_{dq}$ , the device is running close to class B as power output approaches P1dB. This results in higher P1dB and higher PAE (power added efficiency) when compared to a device that is driven by a constant current source as is typically done with active biasing. As an example, at a  $V_{DS} = 2.7V$  and  $I_{dq} = 5$  mA,  $I_d$  increases to 15 mA as a P1dB of +14.5 dBm is approached.

ATF-551M4 Typical Performance Curves, continued

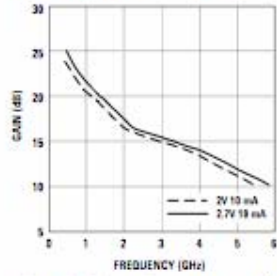


Figure 16. Gain vs. Bias over Frequency<sup>(1)</sup>.

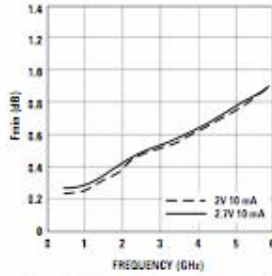


Figure 17. Fmin vs. Bias over Frequency<sup>(2)</sup>.

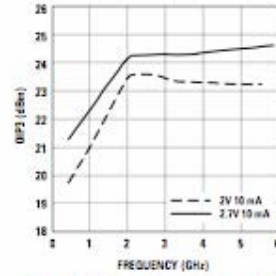


Figure 18. DIP3 vs. Bias over Frequency<sup>(1)</sup>.

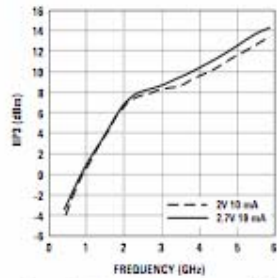


Figure 19. OIP3 vs. Bias over Frequency<sup>(1)</sup>.

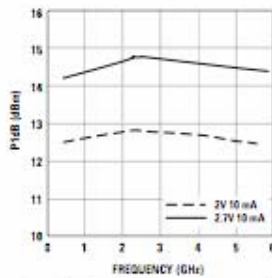


Figure 20. P1dB vs. Bias over Frequency<sup>(1)</sup>.

Notes:

1. Measurements at 2 GHz were made on a fixed tuned production test board that was tuned for optimal OIP3 match with reasonable noise figure at 2.7 V, 10 mA bias. This circuit represents a trade-off between optimal noise match, maximum OIP3 match and a realizable match based on production test board requirements. Measurements taken above and below 2 GHz was made using a double stub tuner at the input tuned for low noise and a double stub tuner at the output tuned for maximum OIP3. Circuit losses have been de-embedded from actual measurements.
2. The Fmin values are based on a set of 16 noise figure measurements made at 16 different impedances using an ATN NP5 test system. From these measurements Fmin is calculated. Refer to the noise parameter measurement section for more information.
3. P1dB measurements are performed with passive biasing. Quiescent drain current, Idsq, is set with zero RF drive applied. As P1dB is approached, the drain current may increase or point. At lower values of Idsq, the device is running close to class B as power output approaches P1dB. This results in higher P1dB and higher PAE (power added efficiency) when compared to a device that is driven by a constant current source as is typically done with active biasing. As an example, at a VDS = 2.7V and Idsq = 5 mA, Id increases to 15 mA as a P1dB of +14.5 dBm is approached.



ATF-551M4 Typical Performance Curves, continued

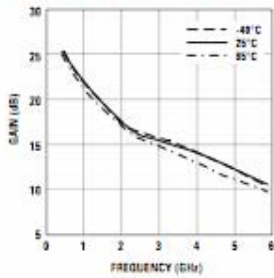


Figure 21. Gain vs. Temperature and Frequency with Bias at 2.7V, 10 mA<sup>[1]</sup>.

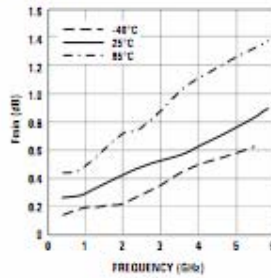


Figure 22. Fmin vs. Temperature and Frequency with Bias at 2.7V, 10 mA<sup>[2]</sup>.

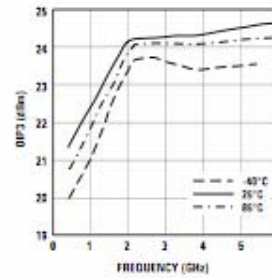


Figure 23. OIP3 vs. Temperature and Frequency with Bias at 2.7V, 10 mA<sup>[1]</sup>.

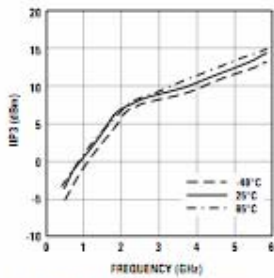


Figure 24. IIP3 vs. Temperature and Frequency with Bias at 2.7V, 10 mA<sup>[1]</sup>.

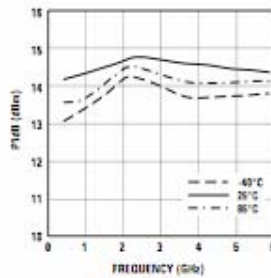


Figure 25. P1dB vs. Temperature and Frequency with Bias at 2.7V, 10 mA<sup>[1]</sup>.

Notes:

1. Measurements at 2 GHz were made on a fixed tuned production test board that was tuned for optimal OIP3 match with reasonable noise figure at 2.7 V, 10 mA bias. This circuit represents a trade-off between optimal noise match, maximum OIP3 match and a realizable match based on production test board requirements. Measurements taken above and below 2 GHz was made using a double stub tuner at the input tuned for low noise and a double stub tuner at the output tuned for maximum OIP3. Circuit losses have been de-embedded from actual measurements.
2. The Fmin values are based on a set of 16 noise figure measurements made at 16 different impedances using an ATN NP5 test system. From these measurements Fmin is calculated. Refer to the noise parameter measurement section for more information.
3. P1dB measurements are performed with passive biasing. Quiescent drain current, Idsq, is set with zero RF drive applied. As P1dB is approached, the drain current may increase or point. At lower values of Idsq, the device is running close to class B as power output approaches P1dB. This results in higher P1dB and higher PAE (power added efficiency) when compared to a device that is driven by a constant current source as is typically done with active biasing. As an example, at a VDS = 2.7V and Idsq = 5 mA, Id increases to 15 mA as a P1dB of +14.5 dBm is approached.

ATF-551M4 Typical Scattering Parameters,  $V_{DS} = 2V$ ,  $I_{DS} = 10\text{ mA}$

Freq. GHz	$S_{11}$			$S_{21}$		$S_{12}$		$S_{22}$		MSG/MAG dB
	Mag.	Ang.	dB	Mag.	Ang.	Mag.	Ang.	Mag.	Ang.	
0.1	0.995	-5.0	20.41	10.479	175.9	0.007	86.3	0.803	-3.3	31.75
0.5	0.954	-29.1	19.95	9.946	158.2	0.031	71.6	0.758	-15.6	25.06
0.9	0.906	-50.7	19.35	9.280	144.2	0.052	60.8	0.710	-27.4	22.52
1.0	0.896	-55.7	19.18	9.103	141.0	0.056	58.3	0.692	-30.2	22.11
1.5	0.833	-79.5	18.15	8.080	125.6	0.075	46.8	0.611	-42.3	20.32
1.9	0.790	-96.5	17.22	7.260	114.9	0.085	39.0	0.547	-56.4	19.32
2.0	0.781	-100.4	17.00	7.078	112.5	0.087	37.3	0.532	-52.3	19.10
2.5	0.739	-118.5	15.84	6.197	101.1	0.095	29.8	0.463	-60.6	18.14
3.0	0.710	-134.4	14.74	5.459	91.2	0.099	23.7	0.404	-67.5	17.41
4.0	0.683	-160.0	12.75	4.341	74.5	0.104	14.8	0.318	-79.6	16.21
5.0	0.679	-179.8	11.03	3.559	60.3	0.105	8.6	0.263	-91.2	15.30
6.0	0.680	166.5	9.65	3.038	48.5	0.107	5.0	0.220	-99.5	14.53
7.0	0.681	154.0	8.43	2.638	37.2	0.107	2.1	0.199	-111.0	13.92
8.0	0.683	143.7	7.43	2.353	26.4	0.110	-0.3	0.185	-123.4	13.30
9.0	0.690	132.7	6.53	2.122	15.7	0.113	-2.6	0.181	-137.7	11.27
10.0	0.687	119.7	5.72	1.932	4.5	0.117	-5.4	0.185	-151.1	9.97
11.0	0.691	106.5	4.98	1.775	-6.4	0.122	-8.4	0.196	-163.5	9.14
12.0	0.696	92.5	4.28	1.636	-17.7	0.129	-12.3	0.209	-174.4	8.44
13.0	0.713	81.8	3.53	1.501	-28.6	0.135	-16.2	0.206	-171.4	7.80
14.0	0.747	67.4	2.82	1.384	-40.4	0.143	-21.8	0.211	-151.2	7.52
15.0	0.759	55.5	1.97	1.255	-51.8	0.149	-27.4	0.237	-131.8	6.73
16.0	0.808	45.4	1.00	1.122	-62.4	0.153	-33.3	0.289	-113.3	6.90
17.0	0.828	37.3	-0.01	0.999	-72.7	0.157	-39.2	0.322	-95.4	6.20
18.0	0.870	30.9	-1.04	0.887	-82.6	0.159	-45.2	0.383	-80.1	7.47

Typical Noise Parameters,  $V_{DS} = 2V$ ,  $I_{DS} = 10\text{ mA}$

Freq. GHz	$F_{min}$ dB	$\Gamma_{opt}$ Mag.	$\Gamma_{opt}$ Ang.	$R_{n/50}$	$G_n$ dB
0.5	0.24	0.62	-4.3	0.14	23.50
0.9	0.24	0.56	8.8	0.13	21.60
1.0	0.28	0.52	13.5	0.12	21.61
1.9	0.45	0.47	38.6	0.11	18.04
2.0	0.39	0.47	42.9	0.11	17.88
2.4	0.47	0.42	52.9	0.11	16.76
3.0	0.55	0.35	74.0	0.09	15.66
3.9	0.61	0.32	105.4	0.08	14.10
5.0	0.74	0.33	144.0	0.06	12.74
5.8	0.89	0.36	164.3	0.05	11.83
6.0	0.90	0.37	166.1	0.05	11.63
7.0	1.03	0.38	-170.9	0.06	10.71
8.0	1.13	0.44	-157.2	0.07	9.99
9.0	1.27	0.48	-142.4	0.09	9.36
10.0	1.53	0.46	-126.0	0.17	8.46

Notes:

1. The  $F_{min}$  values are based on a set of 16 noise figure measurements made at 16 different impedances using an ATN NP5 test system. From these measurements  $F_{min}$  is calculated. Refer to the noise parameter measurement section for more information.
2. S and noise parameters are measured on a microstrip line made on 0.010 inch thick alumina carrier assembly. The input reference plane is at the end of the gate pad. The output reference plane is at the end of the drain pad.

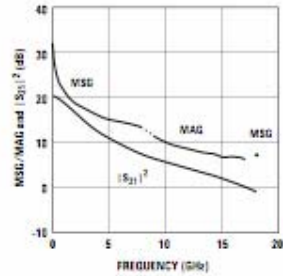


Figure 26. MSG/MAG and  $|S_{21}|^2$  vs. Frequency at 2V, 10 mA.

ATF-551M4 Typical Scattering Parameters,  $V_{DS} = 2V$ ,  $I_{DS} = 15 \text{ mA}$

Freq. GHz	$S_{11}$			$S_{21}$		$S_{12}$		$S_{22}$		MSG/MAG dB
	Mag.	Ang.	dB	Mag.	Ang.	Mag.	Ang.	Mag.	Ang.	
0.1	0.995	-6.6	21.93	12.489	175.5	0.006	86.2	0.785	-3.7	23.18
0.5	0.947	-31.6	21.41	11.757	156.7	0.029	70.9	0.715	-17.0	26.08
0.9	0.892	-54.7	20.67	10.804	142.0	0.048	59.7	0.659	-29.6	23.52
1.0	0.880	-60.1	20.46	10.547	136.8	0.052	57.1	0.641	-32.5	23.07
1.5	0.812	-84.9	19.26	9.186	123.0	0.067	46.0	0.555	-45.0	21.37
1.9	0.768	-102.1	18.23	8.153	112.3	0.076	36.7	0.489	-53.1	20.31
2.0	0.758	-106.1	17.98	7.923	109.9	0.077	37.2	0.474	-55.0	20.12
2.5	0.718	-124.1	16.73	6.859	98.9	0.084	30.5	0.407	-63.2	19.12
3.0	0.692	-139.7	15.55	5.991	89.3	0.088	25.3	0.352	-70.2	18.33
4.0	0.671	-164.5	13.47	4.716	79.3	0.092	18.0	0.272	-82.3	17.10
5.0	0.670	-176.8	11.70	3.845	59.7	0.095	13.1	0.222	-94.5	16.07
6.0	0.671	-163.5	10.30	3.273	48.3	0.098	10.5	0.181	-103.2	15.24
7.0	0.674	-151.5	9.06	2.838	37.4	0.101	8.2	0.164	-115.4	14.49
8.0	0.676	-141.8	8.06	2.528	27.0	0.105	6.1	0.152	-128.5	12.86
9.0	0.684	-130.9	7.14	2.276	16.5	0.111	3.7	0.150	-143.3	11.51
10.0	0.682	-118.0	6.33	2.072	5.6	0.117	0.6	0.156	-156.9	10.35
11.0	0.686	-105.1	5.59	1.903	-5.0	0.124	-3.1	0.170	-169.0	9.57
12.0	0.691	-91.4	4.88	1.753	-16.1	0.132	-7.6	0.183	-179.3	8.87
13.0	0.708	-80.9	4.13	1.609	-26.9	0.140	-12.3	0.181	-185.9	8.27
14.0	0.744	-66.5	3.42	1.483	-38.5	0.148	-18.6	0.188	-145.0	8.14
15.0	0.756	-54.9	2.59	1.347	-49.7	0.155	-24.9	0.217	-125.0	7.23
16.0	0.805	-45.0	1.59	1.201	-60.2	0.158	-31.2	0.253	-106.8	7.38
17.0	0.825	-37.0	0.61	1.073	-70.4	0.161	-37.5	0.310	-89.4	6.61
18.0	0.870	-30.7	-0.41	0.954	-80.1	0.163	-43.8	0.373	-74.9	7.67

Typical Noise Parameters,  $V_{DS} = 2V$ ,  $I_{DS} = 15 \text{ mA}$

Freq. GHz	$F_{min}$ dB	$\Gamma_{opt}$ Mag.	$\Gamma_{opt}$ Ang.	$R_{n/50}$	$G_n$ dB
0.5	0.21	0.61	-6.1	0.12	24.12
0.9	0.21	0.55	7.0	0.12	22.18
1.0	0.27	0.50	11.4	0.11	22.12
1.9	0.42	0.46	38.1	0.10	18.81
2.0	0.37	0.43	42.7	0.10	18.52
2.4	0.44	0.39	52.9	0.10	17.34
3.0	0.52	0.32	74.4	0.08	16.21
3.9	0.57	0.28	108.3	0.07	14.85
5.0	0.71	0.30	149.5	0.06	13.27
5.8	0.65	0.35	170.0	0.05	12.38
6.0	0.68	0.35	171.7	0.05	12.19
7.0	0.97	0.38	-165.9	0.06	11.24
8.0	1.08	0.43	-152.1	0.07	10.49
9.0	1.22	0.47	-138.1	0.10	9.84
10.0	1.44	0.46	-122.5	0.17	8.96

Notes:

- The  $F_{min}$  values are based on a set of 16 noise figure measurements made at 16 different impedances using an ATN NP5 test system. From these measurements  $F_{min}$  is calculated. Refer to the noise parameter measurement section for more information.
- S and noise parameters are measured on a microstrip line made on 0.010 inch thick alumina carrier assembly. The input reference plane is at the end of the gate pad. The output reference plane is at the end of the drain pad.

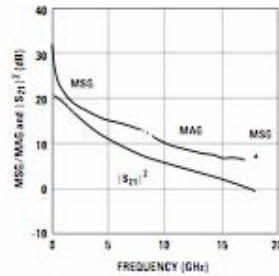


Figure 27. MSG/MAG and  $|S_{21}|^2$  vs. Frequency at 2V, 15 mA.

ATF-551M4 Typical Scattering Parameters,  $V_{DS} = 2V$ ,  $I_{DS} = 20\text{ mA}$

Freq. GHz	$S_{11}$			$S_{21}$		$S_{12}$		$S_{22}$		MSG/MAG dB
	Mag.	Ang.	dB	Mag.	Ang.	Mag.	Ang.	Mag.	Ang.	
0.1	0.994	-6.9	22.85	13.876	175.3	0.006	85.6	0.740	-3.9	33.64
0.5	0.942	-33.3	22.27	12.985	155.7	0.027	70.4	0.687	-17.8	26.82
0.9	0.882	-57.3	21.44	11.806	140.5	0.045	59.0	0.627	-30.9	24.19
1.0	0.869	-62.8	21.21	11.491	137.1	0.048	56.5	0.608	-33.8	23.79
1.5	0.798	-88.1	19.90	9.881	121.3	0.062	45.7	0.520	-46.4	22.02
1.9	0.753	-105.5	18.79	8.704	110.7	0.070	38.9	0.455	-54.4	20.95
2.0	0.744	-109.5	18.53	8.443	108.4	0.071	37.4	0.441	-56.3	20.75
2.5	0.706	-127.4	17.22	7.262	97.5	0.077	31.3	0.376	-64.3	19.75
3.0	0.681	-142.7	16.01	6.314	88.2	0.081	25.7	0.323	-71.0	18.92
4.0	0.663	-167.0	13.88	4.943	72.5	0.085	20.3	0.248	-82.9	17.65
5.0	0.654	174.6	12.09	4.021	59.3	0.089	15.2	0.201	-95.2	16.55
6.0	0.656	161.9	10.58	3.418	48.1	0.093	14.1	0.162	-103.7	15.65
7.0	0.670	150.1	9.43	2.952	37.3	0.097	12.0	0.144	-116.4	14.85
8.0	0.673	140.4	8.42	2.637	27.1	0.103	10.0	0.133	-130.0	12.78
9.0	0.681	129.8	7.51	2.373	16.8	0.109	7.4	0.131	-145.9	11.65
10.0	0.678	117.1	6.68	2.158	6.0	0.117	3.7	0.139	-160.3	10.56
11.0	0.682	104.3	5.94	1.982	-4.6	0.125	-0.2	0.154	-172.7	9.80
12.0	0.688	90.5	5.23	1.826	-15.6	0.133	-5.2	0.168	-175.9	9.11
13.0	0.706	80.3	4.48	1.675	-26.3	0.142	-10.3	0.169	-161.6	8.56
14.0	0.743	65.9	3.76	1.542	-38.0	0.150	-17.0	0.182	-139.6	8.45
15.0	0.753	54.4	2.92	1.400	-48.9	0.157	-23.6	0.212	-121.2	7.48
16.0	0.804	44.7	1.93	1.249	-59.3	0.160	-30.1	0.250	-103.8	7.76
17.0	0.824	36.7	0.95	1.116	-69.4	0.163	-36.5	0.306	-87.0	6.93
18.0	0.869	30.6	-0.05	0.994	-78.9	0.165	-43.0	0.367	-73.0	7.80

Typical Noise Parameters,  $V_{DS} = 2V$ ,  $I_{DS} = 20\text{ mA}$

Freq. GHz	$F_{min}$ dB	$\Gamma_{opt}$		$R_{n/50}$	$G_n$ dB
		Mag.	Ang.		
0.5	0.19	0.69	-7.0	0.11	23.50
0.9	0.20	0.54	6.3	0.11	21.66
1.0	0.25	0.48	10.1	0.10	21.61
1.9	0.41	0.43	38.7	0.09	18.04
2.0	0.36	0.41	43.1	0.09	17.88
2.4	0.43	0.37	53.4	0.09	16.76
3.0	0.51	0.29	76.3	0.08	15.66
3.9	0.58	0.25	112.7	0.07	14.10
5.0	0.70	0.29	154.0	0.05	12.74
5.8	0.85	0.34	173.6	0.05	11.83
6.0	0.86	0.35	175.9	0.05	11.63
7.0	0.94	0.37	-162.3	0.05	10.71
8.0	1.07	0.42	-148.2	0.08	9.99
9.0	1.20	0.48	-135.2	0.10	9.36
10.0	1.43	0.46	-119.5	0.17	8.45

Notes:

1. The  $F_{min}$  values are based on a set of 16 noise figure measurements made at 16 different impedances using an ATN NPS test system. From these measurements  $F_{min}$  is calculated. Refer to the noise parameter measurement section for more information.
2.  $S$  and noise parameters are measured on a microstrip line made on 0.010 inch thick alumina carrier assembly. The input reference plane is at the end of the gate pad. The output reference plane is at the end of the drain pad.

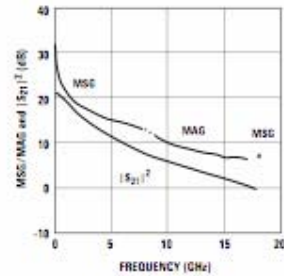


Figure 28. MSG/MAG and  $|S_{21}|^2$  vs. Frequency at 2V, 20 mA.



ATF-551M4 Typical Scattering Parameters,  $V_{DS} = 2.7V$ ,  $I_{DS} = 10\text{ mA}$

Freq. GHz	$S_{11}$			$S_{21}$		$S_{12}$		$S_{22}$		MSG/MAG dB
	Mag.	Ang.	dB	Mag.	Ang.	Mag.	Ang.	Mag.	Ang.	
0.1	0.995	-5.9	20.55	10.856	175.9	0.006	86.3	0.825	-3.0	32.49
0.5	0.955	-28.7	20.11	10.129	158.4	0.028	72.0	0.782	-14.0	25.58
0.9	0.907	-50.0	19.52	9.486	144.6	0.046	61.3	0.735	-24.5	23.13
1.0	0.896	-55.0	19.36	9.292	141.4	0.050	58.8	0.717	-27.0	22.69
1.5	0.833	-78.0	18.34	8.265	126.1	0.067	47.6	0.639	-37.0	20.91
1.9	0.789	-95.5	17.43	7.439	115.4	0.076	40.0	0.577	-44.0	19.91
2.0	0.779	-99.4	17.21	7.255	113.0	0.078	38.4	0.562	-46.2	19.69
2.5	0.737	-117.4	16.07	6.361	101.7	0.085	31.0	0.495	-53.1	18.74
3.0	0.707	-133.4	14.98	5.610	91.8	0.089	25.1	0.439	-58.8	18.00
4.0	0.679	-159.1	13.01	4.471	75.0	0.093	16.6	0.357	-68.3	16.82
5.0	0.674	-178.9	11.30	3.673	60.8	0.094	10.9	0.303	-77.6	15.92
6.0	0.675	167.3	9.93	3.136	49.1	0.095	8.1	0.264	-83.7	15.19
7.0	0.676	154.9	8.72	2.728	37.7	0.096	5.9	0.244	-93.5	14.54
8.0	0.679	144.5	7.73	2.435	27.0	0.099	4.3	0.230	-104.1	12.94
9.0	0.686	133.5	6.84	2.198	16.2	0.102	2.9	0.222	-116.6	11.58
10.0	0.684	120.8	6.03	2.002	5.1	0.107	0.7	0.222	-129.0	10.44
11.0	0.688	107.5	5.30	1.841	-5.9	0.113	-1.7	0.230	-140.8	9.69
12.0	0.693	93.7	4.59	1.696	-17.2	0.121	-5.2	0.239	-151.9	9.02
13.0	0.710	82.7	3.86	1.559	-28.2	0.129	-8.9	0.232	-164.6	8.47
14.0	0.743	68.6	3.19	1.443	-39.8	0.139	-14.3	0.222	-176.6	8.42
15.0	0.760	56.5	2.37	1.314	-51.5	0.147	-20.2	0.232	-155.6	7.69
16.0	0.805	46.2	1.42	1.177	-62.2	0.153	-26.2	0.251	-134.3	8.26
17.0	0.830	38.1	0.43	1.051	-72.0	0.158	-32.5	0.293	-112.0	8.07
18.0	0.872	31.5	-0.58	0.935	-83.1	0.163	-39.1	0.353	-92.7	7.59

Typical Noise Parameters,  $V_{DS} = 2.7V$ ,  $I_{DS} = 10\text{ mA}$

Freq. GHz	$F_{min}$ dB	$\Gamma_{opt}$		$R_{n/50}$	$C_n$ dB
		Mag.	Ang.		
0.5	0.26	0.64	-4.4	0.14	23.79
0.9	0.27	0.57	7.5	0.13	21.80
1.0	0.30	0.54	11.1	0.13	21.60
1.9	0.46	0.49	36.6	0.11	18.06
2.0	0.41	0.48	40.4	0.12	17.92
2.4	0.47	0.44	50.3	0.11	16.79
3.0	0.55	0.36	69.5	0.10	15.70
3.9	0.61	0.32	101.3	0.08	14.24
5.0	0.74	0.32	139.5	0.06	12.86
5.8	0.88	0.35	161.5	0.05	12.01
6.0	0.90	0.35	163.9	0.05	11.82
7.0	1.00	0.37	-173.6	0.06	10.93
8.0	1.12	0.41	-158.2	0.07	10.24
9.0	1.25	0.46	-143.0	0.09	9.66
10.0	1.46	0.46	-127.2	0.15	8.85

Notes:

1. The  $F_{min}$  values are based on a set of 16 noise figure measurements made at 16 different impedances using an ATN NPS test system. From these measurements  $F_{min}$  is calculated. Refer to the noise parameter measurement section for more information.
2.  $S$  and noise parameters are measured on a microstrip line made on 0.010 inch thick alumina carrier assembly. The input reference plane is at the end of the gate pad. The output reference plane is at the end of the drain pad.

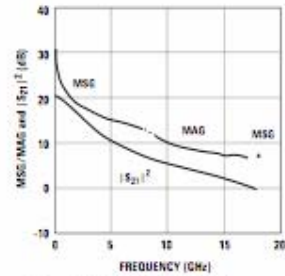


Figure 29. MSG/MAG and  $|S_{21}|^2$  vs. Frequency at 2.7V, 10 mA.

ATF-551M4 Typical Scattering Parameters,  $V_{DS} = 2.7V$ ,  $I_{DS} = 15\text{ mA}$

Freq. GHz	$S_{11}$			$S_{21}$			$S_{12}$			$S_{22}$			MSG/MAG dB
	Mag.	Ang.	dB	Mag.	Ang.	dB	Mag.	Ang.	dB	Mag.	Ang.	dB	
0.1	0.995	-6.5	21.98	12.559	175.6	0.006	86.4	0.793	-3.2	33.21			
0.5	0.949	-31.2	21.47	11.839	156.9	0.026	71.0	0.745	-15.2	26.58			
0.9	0.894	-54.0	20.75	10.905	142.3	0.043	60.1	0.691	-26.4	24.04			
1.0	0.882	-59.4	20.55	10.850	138.9	0.047	57.5	0.673	-28.9	23.55			
1.5	0.814	-84.0	19.37	9.290	123.4	0.061	46.0	0.589	-39.7	21.83			
1.9	0.768	-101.1	18.34	8.265	112.7	0.068	39.5	0.526	-46.0	20.85			
2.0	0.758	-105.1	18.10	8.034	110.3	0.070	38.0	0.511	-48.1	20.60			
2.5	0.718	-123.1	16.86	6.966	99.3	0.076	31.4	0.447	-54.6	19.62			
3.0	0.691	-138.7	15.70	6.095	89.7	0.079	26.3	0.393	-59.9	18.87			
4.0	0.668	-163.5	13.84	4.806	73.6	0.083	19.4	0.318	-68.8	17.63			
5.0	0.667	-177.5	11.88	3.920	59.9	0.085	15.0	0.268	-77.7	16.85			
6.0	0.668	-164.3	10.49	3.345	48.5	0.088	13.1	0.230	-83.3	15.80			
7.0	0.671	-152.2	9.26	2.904	37.5	0.091	11.4	0.212	-89.0	15.04			
8.0	0.673	-142.3	8.27	2.591	27.0	0.095	10.0	0.198	-103.4	12.89			
9.0	0.682	-131.6	7.37	2.335	16.4	0.101	8.4	0.190	-116.2	11.88			
10.0	0.677	-118.5	6.56	2.126	5.4	0.107	5.8	0.190	-129.6	10.70			
11.0	0.684	-105.8	5.83	1.956	-5.3	0.115	2.8	0.198	-142.6	10.06			
12.0	0.690	-91.7	5.12	1.804	-16.7	0.124	-1.7	0.210	-154.2	9.46			
13.0	0.707	-81.2	4.38	1.656	-27.5	0.133	-6.1	0.205	-167.8	8.93			
14.0	0.744	-66.4	3.68	1.528	-39.4	0.143	-12.3	0.200	-172.5	9.10			
15.0	0.750	-55.1	2.85	1.399	-50.6	0.151	-18.7	0.212	-150.9	7.85			
16.0	0.806	-45.2	1.88	1.242	-61.2	0.156	-25.1	0.236	-129.7	9.01			
17.0	0.824	-37.1	0.92	1.112	-71.5	0.162	-31.6	0.282	-107.9	8.37			
18.0	0.872	-31.0	-0.08	0.991	-81.5	0.166	-38.2	0.337	-89.7	7.76			

Typical Noise Parameters,  $V_{DS} = 2.7V$ ,  $I_{DS} = 15\text{ mA}$

Freq. GHz	$F_{min}$	$\Gamma_{opt}$	$\Gamma_{opt}$	$R_{n/50}$	$G_a$
	dB	Mag.	Ang.		
0.5	0.18	0.61	-6.0	0.12	24.49
0.9	0.18	0.58	6.8	0.12	22.38
1.0	0.24	0.5	10.7	0.11	22.32
1.9	0.38	0.45	36.9	0.1	18.78
2.0	0.33	0.43	41.9	0.1	18.85
2.4	0.42	0.39	50.9	0.1	17.47
3.0	0.5	0.31	73.0	0.08	16.37
3.9	0.55	0.28	107.0	0.07	14.93
5.0	0.68	0.29	146.6	0.06	13.4
5.8	0.83	0.33	168.7	0.05	12.54
6.0	0.84	0.34	170.7	0.05	12.36
7.0	0.95	0.36	-166.9	0.06	11.44
8.0	1.06	0.41	-152.3	0.07	10.89
9.0	1.18	0.46	-138.1	0.1	10.12
10.0	1.43	0.44	-122.5	0.16	9.21

Notes:

1. The  $F_{min}$  values are based on a set of 16 noise figure measurements made at 16 different impedances using an ATN NP5 test system. From these measurements  $F_{min}$  is calculated. Refer to the noise parameter measurement section for more information.
2. S and noise parameters are measured on a microstrip line made on a 0.010 inch thick alumina carrier assembly. The input reference plane is at the end of the gate pad. The output reference plane is at the end of the drain pad.

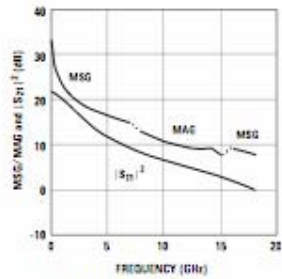


Figure 30. MSG/MAG and  $|S_{21}|^2$  vs. Frequency at 2.7V, 15 mA.

ATF-551M4 Typical Scattering Parameters,  $V_{DS} = 2.7V$ ,  $I_{DS} = 20\text{ mA}$

Freq. GHz	$S_{11}$			$S_{21}$			$S_{12}$			$S_{22}$			MSG/MAG dB
	Mag.	Ang.	dB	Mag.	Ang.	dB	Mag.	Ang.	dB	Mag.	Ang.	dB	
0.1	0.995	-6.8	22.92	13.988	175.4		0.005	86.4		0.772	-3.4	34.47	
0.5	0.943	-33.0	22.35	13.103	155.9		0.024	79.6		0.72	-15.7	27.37	
0.9	0.883	-50.9	21.53	11.932	140.7		0.04	59.4		0.662	-27.1	24.75	
1.0	0.87	-62.4	21.30	11.816	137.3		0.043	56.9		0.643	-29.6	24.32	
1.5	0.798	-87.6	20.00	10.004	121.6		0.056	46.2		0.557	-40.2	22.52	
1.9	0.752	-104.9	18.91	8.822	111.0		0.063	39.6		0.494	-46.7	21.46	
2.0	0.743	-108.8	18.65	8.557	108.6		0.064	38.2		0.48	-48.1	21.26	
2.5	0.704	-126.7	17.35	7.367	97.8		0.069	32.3		0.417	-54.2	20.28	
3.0	0.68	-142.1	16.14	6.411	88.4		0.072	27.8		0.367	-59.0	19.50	
4.0	0.66	-166.3	14.02	5.026	72.8		0.076	22.0		0.297	-67.2	18.20	
5.0	0.662	175.2	12.25	4.095	59.5		0.079	18.6		0.251	-75.7	17.15	
6.0	0.664	152.6	10.84	3.483	48.4		0.083	17.4		0.216	-80.7	16.23	
7.0	0.667	150.9	9.81	3.022	37.6		0.087	16.1		0.199	-90.4	14.69	
8.0	0.67	141.2	8.81	2.695	27.3		0.093	14.8		0.185	-100.6	13.08	
9.0	0.679	130.8	7.71	2.429	16.9		0.099	13.0		0.177	-113.5	12.08	
10.0	0.677	118.1	6.90	2.213	6.0		0.107	9.9		0.178	-127.2	11.08	
11.0	0.683	105.4	6.17	2.034	-4.5		0.116	6.4		0.186	-140.4	10.44	
12.0	0.688	91.4	5.46	1.876	-15.8		0.126	1.8		0.198	-152.2	9.85	
13.0	0.705	80.9	4.72	1.722	-26.5		0.136	-3.2		0.193	-165.9	9.37	
14.0	0.741	66.5	4.03	1.59	-38.3		0.146	-9.8		0.188	-173.7	9.78	
15.0	0.75	55.0	3.19	1.444	-49.5		0.154	-16.5		0.2	-151.1	8.35	
16.0	0.803	45.1	2.22	1.291	-60.1		0.159	-23.2		0.224	-129.5	9.10	
17.0	0.823	37.2	1.26	1.156	-70.3		0.165	-29.8		0.269	-107.3	8.45	
18.0	0.872	31.0	0.27	1.032	-80.2		0.168	-36.6		0.325	-88.8	7.88	

Typical Noise Parameters,  $V_{DS} = 2.7V$ ,  $I_{DS} = 20\text{ mA}$

Freq. GHz	$F_{min}$	$\Gamma_{opt}$	$\Gamma_{opt}$	$R_{n/50}$	$G_a$
	dB	Mag.	Ang.		
0.5	0.18	0.61	-6.7	0.12	24.89
0.9	0.18	0.55	5.9	0.11	22.72
1.0	0.23	0.49	9.9	0.10	22.68
1.9	0.39	0.43	37.8	0.09	19.18
2.0	0.36	0.42	41.6	0.09	18.98
2.4	0.43	0.37	51.7	0.09	17.83
3.0	0.51	0.29	73.8	0.08	16.89
3.9	0.56	0.26	110.7	0.07	15.19
5.0	0.68	0.28	152.8	0.05	13.79
5.8	0.83	0.33	172.9	0.05	12.91
6.0	0.85	0.33	175.6	0.05	12.73
7.0	0.95	0.37	-162.4	0.06	11.80
8.0	1.06	0.41	-148.8	0.08	11.06
9.0	1.19	0.47	-135.5	0.10	10.47
10.0	1.41	0.46	-119.2	0.17	9.59

Notes:

- The  $F_{min}$  values are based on a set of 16 noise figure measurements made at 16 different impedances using an ATN NP5 test system. From these measurements  $F_{min}$  is calculated. Refer to the noise parameter measurement section for more information.
- S and noise parameters are measured on a microstrip line made on a 0.010 inch thick alumina carrier assembly. The input reference plane is at the end of the gate pad. The output reference plane is at the end of the drain pad.

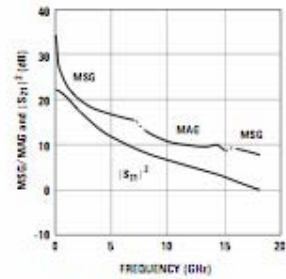


Figure 31. MSG/MAG and  $|S_{21}|^2$  vs. Frequency at 2.7V, 20 mA.

ATF-551M4 Typical Scattering Parameters,  $V_{DS} = 3V$ ,  $I_{DS} = 10\text{ mA}$

Freq. GHz	$S_{11}$			$S_{21}$			$S_{12}$			$S_{22}$			MSG/MAG dB
	Mag.	Ang.	dB	Mag.	Ang.	dB	Mag.	Ang.	dB	Mag.	Ang.	dB	
0.1	0.996	-5.9	20.49	10.578	176.0	0.006	86.1	0.835	-2.8	32.46			
0.5	0.957	-28.4	20.05	10.059	158.5	0.027	72.0	0.792	-13.4	25.71			
0.9	0.909	-49.8	19.48	9.420	144.8	0.045	61.5	0.747	-23.5	23.21			
1.0	0.899	-54.8	19.32	9.246	141.6	0.049	59.1	0.730	-25.9	22.76			
1.5	0.836	-78.1	18.32	8.241	126.3	0.065	47.9	0.653	-36.1	21.03			
1.9	0.792	-94.9	17.41	7.424	115.7	0.074	40.3	0.593	-42.7	20.01			
2.0	0.782	-98.8	17.20	7.241	113.2	0.075	38.6	0.578	-44.2	19.85			
2.5	0.740	-116.8	16.07	6.360	101.9	0.082	31.3	0.513	-50.7	18.90			
3.0	0.709	-132.8	14.99	5.616	91.9	0.086	25.3	0.458	-56.0	18.15			
4.0	0.680	-158.5	13.03	4.481	75.1	0.090	16.9	0.378	-64.9	16.97			
5.0	0.675	-178.4	11.33	3.684	60.9	0.091	11.3	0.325	-73.5	16.07			
6.0	0.675	167.8	9.96	3.146	49.1	0.092	8.7	0.287	-79.1	15.34			
7.0	0.676	155.1	8.75	2.738	37.8	0.093	6.8	0.267	-88.4	14.69			
8.0	0.678	144.9	7.77	2.447	26.8	0.095	5.4	0.252	-98.8	12.90			
9.0	0.686	133.8	6.88	2.209	16.0	0.099	4.1	0.242	-110.5	11.73			
10.0	0.682	120.5	6.09	2.015	4.7	0.104	2.1	0.241	-122.9	10.56			
11.0	0.688	107.5	5.37	1.855	-6.3	0.110	0.0	0.247	-135.1	9.88			
12.0	0.694	93.3	4.67	1.711	-17.8	0.118	-3.4	0.256	-146.5	9.26			
13.0	0.711	82.4	3.92	1.571	-28.8	0.127	-6.9	0.250	-159.0	8.76			
14.0	0.746	67.5	3.24	1.452	-40.8	0.137	-12.8	0.240	-176.5	8.90			
15.0	0.753	55.9	2.41	1.320	-52.4	0.146	-18.5	0.246	-183.0	7.74			
16.0	0.807	45.8	1.46	1.183	-63.1	0.152	-24.5	0.260	-142.0	8.91			
17.0	0.826	37.6	0.48	1.057	-73.7	0.159	-30.8	0.297	-119.0	8.23			
18.0	0.874	31.3	-0.53	0.941	-84.1	0.164	-37.5	0.348	-98.9	7.59			

Typical Noise Parameters,  $V_{DS} = 3V$ ,  $I_{DS} = 10\text{ mA}$

Freq. GHz	$F_{min}$ dB	$\Gamma_{opt}$		$R_{n/50}$	$G_n$ dB
		Mag.	Ang.		
0.5	0.23	0.65	-4.3	0.14	23.81
0.9	0.24	0.58	7.4	0.13	21.82
1.0	0.26	0.54	10.7	0.13	21.62
1.9	0.43	0.50	36.2	0.11	18.05
2.0	0.38	0.48	40.4	0.12	17.96
2.4	0.43	0.44	49.8	0.11	16.84
3.0	0.51	0.38	69.2	0.10	15.76
3.9	0.59	0.31	99.4	0.08	14.23
5.0	0.70	0.32	139.3	0.06	12.94
5.8	0.85	0.35	160.3	0.05	12.04
6.0	0.86	0.35	162.3	0.05	11.85
7.0	0.98	0.38	-173.7	0.06	10.99
8.0	1.09	0.41	-158.8	0.07	10.29
9.0	1.23	0.45	-143.7	0.09	9.71
10.0	1.45	0.44	-126.8	0.15	8.88

Notes:

- The  $F_{min}$  values are based on a set of 16 noise figure measurements made at 16 different impedances using an ATN NPS test system. From these measurements  $F_{min}$  is calculated. Refer to the noise parameter measurement section for more information.
- S and noise parameters are measured on a microstrip line made on 0.010 inch thick alumina carrier assembly. The input reference plane is at the end of the gate pad. The output reference plane is at the end of the drain pad.

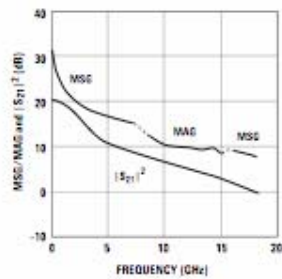


Figure 32. MSG/MAG and  $|S_{21}|^2$  vs. Frequency at 3V, 10 mA.



ATF-551M4 Typical Scattering Parameters,  $V_{DS} = 3V$ ,  $I_{DS} = 15\text{ mA}$

Freq. GHz	$S_{11}$			$S_{21}$		$S_{12}$		$S_{22}$		MSG/MAG dB
	Mag.	Ang.	dB	Mag.	Ang.	Mag.	Ang.	Mag.	Ang.	
0.1	0.995	-6.5	22.02	12.623	175.6	0.005	86.0	0.802	-3.1	34.02
0.5	0.949	-31.2	21.51	11.900	156.9	0.025	71.0	0.754	-14.6	26.76
0.9	0.894	-54.1	20.79	10.958	142.3	0.041	60.1	0.700	-25.4	24.27
1.0	0.882	-59.4	20.59	10.701	138.9	0.045	57.6	0.682	-27.8	23.76
1.5	0.813	-84.0	19.41	9.341	123.3	0.059	46.7	0.599	-38.1	22.00
1.9	0.768	-101.2	18.38	8.301	112.7	0.066	39.7	0.537	-44.5	21.00
2.0	0.758	-105.1	18.14	8.068	110.3	0.067	38.1	0.522	-45.9	20.81
2.5	0.717	-123.1	16.90	6.996	99.2	0.073	31.6	0.459	-52.0	19.82
3.0	0.690	-138.7	15.74	6.120	89.7	0.076	26.7	0.407	-56.9	19.06
4.0	0.668	-163.5	13.68	4.829	73.6	0.080	20.0	0.334	-65.0	17.81
5.0	0.666	-177.5	11.93	3.947	59.9	0.082	15.0	0.286	-73.3	16.82
6.0	0.668	-164.4	10.53	3.363	48.5	0.084	14.2	0.250	-78.4	16.02
7.0	0.670	-152.3	9.31	2.921	37.5	0.087	12.9	0.232	-87.6	14.96
8.0	0.672	-142.4	8.32	2.607	27.0	0.092	11.8	0.216	-97.7	12.99
9.0	0.681	-131.7	7.43	2.351	16.4	0.098	10.4	0.209	-110.0	12.01
10.0	0.678	-118.6	6.82	2.142	5.3	0.104	7.8	0.209	-122.9	10.90
11.0	0.684	-105.8	5.89	1.970	-5.5	0.113	4.9	0.215	-135.4	10.28
12.0	0.690	-91.8	5.19	1.817	-16.8	0.122	0.7	0.226	-147.1	9.70
13.0	0.707	-81.3	4.44	1.667	-27.8	0.132	-3.7	0.221	-160.3	9.23
14.0	0.744	-66.6	3.75	1.540	-39.5	0.142	-10.0	0.211	-179.5	8.82
15.0	0.751	-55.2	2.93	1.401	-50.7	0.151	-16.4	0.216	-159.7	8.26
16.0	0.807	-45.3	1.97	1.254	-61.4	0.157	-22.8	0.236	-137.8	8.02
17.0	0.824	-37.3	1.01	1.123	-71.9	0.163	-29.5	0.277	-114.5	8.38
18.0	0.874	-31.1	0.02	1.002	-82.0	0.167	-36.2	0.330	-85.0	7.78

Typical Noise Parameters,  $V_{DS} = 3V$ ,  $I_{DS} = 15\text{ mA}$

Freq. GHz	$F_{min}$ dB	$\Gamma_{opt}$ Mag.	$\Gamma_{opt}$ Ang.	$R_{n/50}$	$G_n$ dB
0.5	0.18	0.63	-6.3	0.12	24.41
0.9	0.19	0.56	6.8	0.12	22.45
1.0	0.23	0.51	10.0	0.11	22.29
1.9	0.39	0.46	36.5	0.10	18.75
2.0	0.35	0.44	40.8	0.10	18.61
2.4	0.42	0.39	50.1	0.10	17.46
3.0	0.49	0.31	72.5	0.08	16.42
3.9	0.56	0.27	104.4	0.07	14.90
5.0	0.66	0.29	146.9	0.06	13.48
5.8	0.83	0.33	167.4	0.05	12.58
6.0	0.84	0.33	169.0	0.05	12.38
7.0	0.94	0.35	-166.9	0.06	11.49
8.0	1.05	0.40	-152.7	0.07	10.77
9.0	1.19	0.46	-138.6	0.09	10.23
10.0	1.40	0.44	-121.9	0.16	9.32

Notes:

- The  $F_{min}$  values are based on a set of 16 noise figure measurements made at 16 different impedances using an ATN NPS test system. From these measurements  $F_{min}$  is calculated. Refer to the noise parameter measurement section for more information.
- S and noise parameters are measured on a microstrip line made on 0.010 inch thick alumina carrier assembly. The input reference plane is at the end of the gate pad. The output reference plane is at the end of the drain pad.

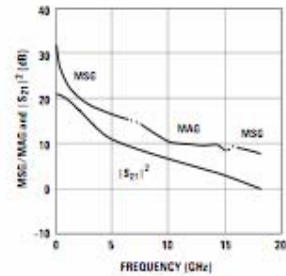


Figure 33. MSG/MAG and  $|S_{21}|^2$  vs. Frequency at 3V, 15 mA.

ATF-551M4 Typical Scattering Parameters,  $V_{DS} = 3V$ ,  $I_{DS} = 20\text{ mA}$

Freq. GHz	$S_{11}$			$S_{21}$			$S_{12}$			$S_{22}$			MSG/MAG dB
	Mag.	Ang.	dB	Mag.	Ang.	dB	Mag.	Ang.	dB	Mag.	Ang.	dB	
0.1	0.995	-6.8	22.91	13.987	175.4		0.005	86.1		0.781	-3.3	34.47	
0.5	0.943	-33.0	22.35	13.101	155.8		0.024	70.5		0.730	-15.2	27.37	
0.9	0.883	-56.9	21.53	11.932	140.7		0.039	59.5		0.672	-26.1	24.86	
1.0	0.870	-62.4	21.30	11.614	137.2		0.042	56.9		0.654	-28.5	24.42	
1.5	0.798	-87.6	20.00	10.004	121.5		0.054	46.3		0.569	-38.5	22.88	
1.9	0.752	-104.9	18.91	8.820	111.0		0.061	39.7		0.506	-44.6	21.80	
2.0	0.743	-108.9	18.84	8.555	108.6		0.062	38.3		0.493	-46.0	21.40	
2.5	0.704	-126.7	17.35	7.368	97.7		0.067	32.4		0.431	-51.6	20.41	
3.0	0.679	-142.1	16.14	6.412	88.4		0.070	28.1		0.383	-56.0	19.62	
4.0	0.660	-166.3	14.83	5.028	72.7		0.074	22.5		0.314	-63.5	18.32	
5.0	0.662	-175.3	12.25	4.099	59.4		0.076	19.2		0.270	-71.5	17.32	
6.0	0.664	-162.6	10.85	3.488	48.3		0.080	16.3		0.237	-76.2	16.39	
7.0	0.667	-150.9	9.62	3.027	37.5		0.084	17.2		0.220	-85.2	14.66	
8.0	0.670	-141.3	8.63	2.701	27.2		0.090	16.3		0.207	-95.2	13.18	
9.0	0.679	-130.9	7.73	2.435	16.8		0.096	14.6		0.198	-107.6	12.20	
10.0	0.677	-118.1	6.92	2.219	5.9		0.104	11.7		0.190	-120.6	11.21	
11.0	0.683	-105.4	6.19	2.040	-4.8		0.114	8.4		0.205	-133.4	10.64	
12.0	0.689	-91.4	5.49	1.881	-16.0		0.124	3.8		0.216	-145.2	10.10	
13.0	0.705	-80.9	4.75	1.727	-26.8		0.134	-1.0		0.210	-158.4	9.62	
14.0	0.742	-66.4	4.05	1.594	-38.6		0.145	-7.7		0.199	-170.0	10.41	
15.0	0.751	-55.0	3.23	1.451	-49.8		0.153	-14.4		0.207	-180.3	8.80	
16.0	0.806	-45.1	2.27	1.298	-60.4		0.159	-21.1		0.225	-138.1	9.12	
17.0	0.826	-37.2	1.32	1.164	-70.8		0.165	-27.9		0.285	-114.0	8.48	
18.0	0.874	-31.1	0.33	1.039	-80.6		0.170	-34.9		0.320	-94.1	7.86	

Typical Noise Parameters,  $V_{DS} = 3V$ ,  $I_{DS} = 20\text{ mA}$

Freq. GHz	$F_{min}$ dB	$\Gamma_{opt}$ Mag.	$\Gamma_{opt}$ Ang.	$R_n/50$	$G_n$ dB
0.5	0.17	0.62	-6.2	0.12	24.92
0.9	0.18	0.55	6.0	0.11	22.79
1.0	0.24	0.50	9.5	0.10	22.59
1.9	0.39	0.43	37.5	0.10	19.22
2.0	0.36	0.41	41.2	0.09	19.00
2.4	0.42	0.37	50.9	0.09	17.83
3.0	0.50	0.29	73.6	0.08	16.72
3.9	0.57	0.25	109.4	0.07	15.18
5.0	0.68	0.28	151.6	0.06	13.80
5.8	0.83	0.32	172.5	0.05	12.93
6.0	0.85	0.33	175.6	0.05	12.77
7.0	0.93	0.36	-162.7	0.06	11.84
8.0	1.05	0.41	-149.1	0.08	11.09
9.0	1.19	0.46	-135.5	0.10	10.53
10.0	1.39	0.45	-119.4	0.17	9.64

Notes:

1. The  $F_{min}$  values are based on a set of 16 noise figure measurements made at 16 different impedances using an ATN NPS test system. From these measurements  $F_{min}$  is calculated. Refer to the noise parameter measurement section for more information.
2.  $S$  and noise parameters are measured on a microstrip line made on 0.010 inch thick alumina carrier assembly. The input reference plane is at the end of the gate pad. The output reference plane is at the end of the drain pad.

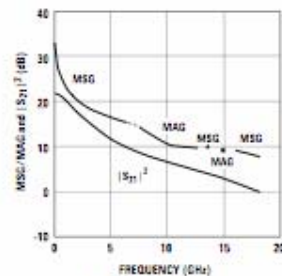


Figure 34. MSG/MAG and  $|S_{21}|^2$  vs. Frequency at 3V, 20 mA.

ATF-551M4 Typical Scattering Parameters,  $V_{DS} = 3V$ ,  $I_{DS} = 30\text{ mA}$

Freq. GHz	$S_{11}$			$S_{21}$			$S_{12}$			$S_{22}$			MSG/MAG dB
	Mag.	Ang.	dB	Mag.	Ang.	dB	Mag.	Ang.	dB	Mag.	Ang.	dB	
0.1	0.994	-7.4	23.90	15.662	175.0		0.005	86.1		0.760	-3.4	34.96	
0.5	0.936	-35.3	23.25	14.544	154.5		0.022	69.8		0.705	-15.4	28.20	
0.9	0.870	-60.4	22.32	13.058	138.7		0.035	58.7		0.644	-26.2	25.72	
1.0	0.856	-66.1	22.05	12.665	135.2		0.038	56.2		0.624	-28.5	25.23	
1.5	0.781	-92.0	20.61	10.732	119.4		0.048	46.0		0.539	-37.7	23.49	
1.9	0.736	-109.4	19.44	9.374	106.9		0.054	40.1		0.480	-43.1	22.40	
2.0	0.726	-113.3	19.15	9.072	106.6		0.055	38.0		0.467	-44.2	22.17	
2.5	0.690	-131.0	17.79	7.753	96.0		0.059	33.7		0.410	-49.0	21.19	
3.0	0.668	-146.1	16.54	6.713	86.9		0.062	30.3		0.367	-52.7	20.35	
4.0	0.653	-169.6	14.38	5.234	71.7		0.066	26.1		0.307	-59.2	18.99	
5.0	0.656	172.7	12.58	4.258	58.7		0.069	23.0		0.268	-66.7	17.90	
6.0	0.659	160.5	11.17	3.618	47.9		0.074	23.6		0.238	-70.9	16.89	
7.0	0.663	148.0	9.93	3.138	37.2		0.079	22.9		0.224	-79.8	14.61	
8.0	0.666	139.6	8.94	2.798	27.1		0.086	21.9		0.211	-89.5	13.35	
9.0	0.676	129.3	8.03	2.522	16.8		0.094	20.1		0.203	-101.5	12.55	
10.0	0.674	116.6	7.22	2.296	5.9		0.103	16.9		0.202	-114.5	11.58	
11.0	0.680	104.1	6.40	2.109	-4.6		0.113	13.1		0.208	-127.3	11.01	
12.0	0.688	90.3	5.77	1.944	-15.8		0.124	8.0		0.219	-138.4	10.62	
13.0	0.705	80.1	5.03	1.784	-26.4		0.135	3.0		0.213	-152.3	10.38	
14.0	0.743	65.0	4.34	1.648	-38.0		0.147	-4.1		0.200	-170.8	10.50	
15.0	0.751	54.5	3.53	1.502	-49.2		0.156	-11.1		0.203	-186.8	9.84	
16.0	0.806	44.9	2.56	1.343	-59.8		0.162	-18.1		0.218	-143.9	9.19	
17.0	0.826	37.0	1.64	1.208	-70.1		0.168	-25.2		0.254	-119.4	8.57	
18.0	0.875	31.0	0.67	1.080	-80.2		0.174	-32.4		0.306	-97.4	7.93	

Typical Noise Parameters,  $V_{DS} = 3V$ ,  $I_{DS} = 30\text{ mA}$

Freq. GHz	$F_{min}$ dB	$\Gamma_{opt}$		$R_{n/50}$	$G_n$ dB
		Mag.	Ang.		
0.5	0.18	0.50	-6.2	0.11	25.60
0.9	0.18	0.55	6.4	0.11	23.17
1.0	0.24	0.47	10.1	0.10	23.19
1.9	0.39	0.39	39.1	0.09	19.73
2.0	0.38	0.38	42.7	0.09	19.48
2.4	0.45	0.33	54.2	0.09	18.36
3.0	0.52	0.28	79.0	0.08	17.20
3.9	0.59	0.23	119.0	0.06	15.86
5.0	0.71	0.28	162.1	0.05	14.28
5.8	0.86	0.33	-179.3	0.05	13.39
6.0	0.89	0.33	-176.7	0.05	13.20
7.0	0.99	0.37	-156.1	0.07	12.27
8.0	1.12	0.42	-143.5	0.09	11.50
9.0	1.26	0.48	-130.8	0.12	10.96
10.0	1.50	0.46	-115.1	0.20	10.01

Notes:

1. The  $F_{min}$  values are based on a set of 16 noise figure measurements made at 16 different impedances using an ATN NPS test system. From these measurements  $F_{min}$  is calculated. Refer to the noise parameter measurement section for more information.
2. S and noise parameters are measured on a microstrip line made on 0.010 inch thick alumina carrier assembly. The input reference plane is at the end of the gate pad. The output reference plane is at the end of the drain pad.

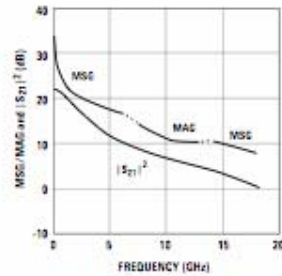


Figure 35. MSG/MAG and  $|S_{21}|^2$  vs. Frequency at 3V, 30 mA.



### S and Noise Parameter Measurements

The position of the reference planes used for the measurement of both S and Noise Parameter measurements is shown in Figure 36. The reference plane can be described as being at the center of both the gate and drain pads.

S and noise parameters are measured with a 50 ohm microstrip test fixture made with a 0.010" thickness aluminum substrate. Both source pads are connected directly to ground via a 0.010" thickness metal rib which provides a very low inductance path to ground for both source pads. The inductance associated with the addition of printed circuit board plated through holes and source bypass capacitors must be added to the computer circuit simulation to properly model the effect of grounding the source leads in a typical amplifier design.

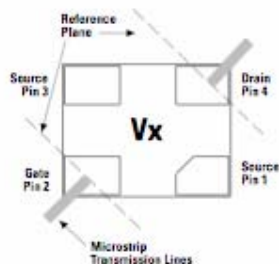


Figure 36. Position of the Reference Planes.

### Noise Parameter Applications Information

The Fmin values are based on a set of 16 noise figure measurements made at 16 different impedances using an ATN NP5 test system. From these measurements, a true Fmin is calculated. Fmin represents the true minimum noise figure of the device when the device is presented with an impedance matching network that transforms the

source impedance, typically 50Ω, to an impedance represented by the reflection coefficient  $\Gamma_o$ . The designer must design a matching network that will present  $\Gamma_o$  to the device with minimal associated circuit losses. The noise figure of the completed amplifier is equal to the noise figure of the device plus the losses of the matching network preceding the device. The noise figure of the device is equal to Fmin only when the device is presented with  $\Gamma_o$ . If the reflection coefficient of the matching network is other than  $\Gamma_o$ , then the noise figure of the device will be greater than Fmin based on the following equation.

$$NF = F_{min} + 4 R_n \frac{|\Gamma_s - \Gamma_o|^2}{Z_o (1 + \Gamma_o)^2 (1 - |\Gamma_o|^2)}$$

Where  $R_n/Z_o$  is the normalized noise resistance,  $\Gamma_o$  is the optimum reflection coefficient required to produce Fmin and  $\Gamma_s$  is the reflection coefficient of the source impedance actually presented to the device.

The losses of the matching networks are non-zero and they will also add to the noise figure of the device creating a higher amplifier noise figure. The losses of the matching networks are related to the Q of the components and associated printed circuit board loss.  $\Gamma_o$  is typically fairly low at higher frequencies and increases as frequency is lowered. Larger gate width devices will typically have a lower  $\Gamma_o$  as compared to narrower gate width devices. Typically for FETs, the higher  $\Gamma_o$  usually infers that an impedance much higher than 50Ω is required for the device to produce Fmin. At VHF frequencies and even lower L Band frequencies, the required impedance can be in the vicinity of several thousand

ohms. Matching to such a high impedance requires very hi-Q components in order to minimize circuit losses. As an example at 900 MHz, when air wound coils (Q>100) are used for matching networks, the loss can still be up to 0.25 dB which will add directly to the noise figure of the device. Using multilayer molded inductors with Qs in the 30 to 50 range results in additional loss over the air wound coil. Losses as high as 0.5 dB or greater add to the typical 0.15 dB Fmin of the device creating an amplifier noise figure of nearly 0.65 dB.

### SMT Assembly

The package can be soldered using either lead-bearing or lead-free alloys (higher peak temperatures). Reliable assembly of surface mount components is a complex process that involves many material, process, and equipment factors, including: method of heating (e.g. IR or vapor phase reflow, wave soldering, etc) circuit board material, conductor thickness and pattern, type of solder alloy, and the thermal conductivity and thermal mass of components. Components with a low mass, such as the Minipak 1412 package, will reach solder reflow temperatures faster than those with a greater mass.

The recommended leaded solder time-temperature profile is shown in Figure 37. This profile is representative of an IR reflow type of surface mount assembly process. After ramping up from room temperature, the circuit board with components attached to it (held in place with solder paste) passes through one or more preheat zones. The preheat zones increase the temperature of the board and components to prevent thermal shock and begin evaporating solvents from the solder paste. The reflow zone

briefly elevates the temperature sufficiently to produce a reflow of the solder.

The rates of change of temperature for the ramp-up and cool-down zones are chosen to be low enough to not cause deformation of board or damage to components due to thermal shock. The maximum temperature in the reflow zone ( $T_{max}$ ) should not exceed 235°C for leaded solder.

These parameters are typical for a surface mount assembly process for the ATF-551M4. As a general guideline, the circuit board and components should only be exposed to the minimum temperatures and times the necessary to achieve a uniform reflow of solder.

The recommended lead-free reflow profile is shown in Figure 38.

#### Electrostatic Sensitivity

FETs and RFICs are electrostatic discharge (ESD) sensitive devices. Agilent devices are manufactured using a very robust and reliable PHEMT process, however, permanent damage may occur to these devices if they are subjected to high-energy electrostatic discharges. Electrostatic charges as high as several thousand volts (which readily accumulate on the human body and on test equipment) can discharge without detection and may result in failure or degradation in performance and reliability.

Electronic devices may be subjected to ESD damage in any of the following areas:

- Storage & handling
- Inspection
- Assembly & testing
- In-circuit use

The ATF-551M4 is an ESD Class 1 device. Therefore, proper ESD precautions are recommended when handling, inspecting, testing, and assembling these devices to avoid damage.

Any user-accessible points in wireless equipment (e.g. antenna or battery terminals) provide an opportunity for ESD damage.

For circuit applications in which the ATF-551M4 is used as an input or output stage with close coupling to an external antenna, the device should be protected from high voltage spikes due to human contact with the antenna. A good practice, illustrated in Figure 39, is to place a shunt inductor or RF choke at the antenna connection to protect the receiver and transmitter circuits. It is often advantageous to integrate the RF choke into the design of the diplexer or T/R switch control circuitry.

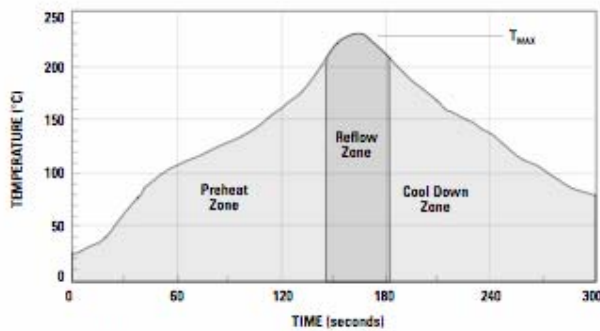


Figure 37. Leaded Solder Reflow Profile.

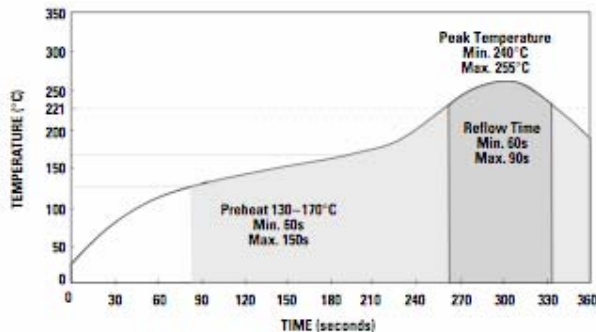


Figure 38. Lead-free Solder Reflow Profile.

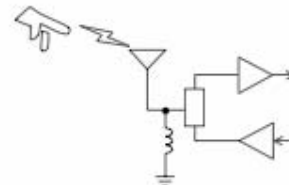


Figure 39. In-circuit ESD Protection.



## ATF-551M4 Applications Information

### Introduction

Agilent Technologies's ATF-551M4 is a low noise enhancement mode PHEMT designed for use in low cost commercial applications in the VHF through 10 GHz frequency range. As opposed to a typical depletion mode PHEMT where the gate must be made negative with respect to the source for proper operation, an enhancement mode PHEMT requires that the gate be made more positive than the source for normal operation. Therefore a negative power supply voltage is not required for an enhancement mode device. Biasing an enhancement mode PHEMT is much like biasing the typical bipolar junction transistor. Instead of a 0.7V base to emitter voltage, the ATF-551M4 enhancement mode PHEMT requires a nominal 0.47V potential between the gate and source for a nominal drain current of 10 mA.

### Matching Networks

The techniques for impedance matching an enhancement mode device are very similar to those for matching a depletion mode device. The only difference is in the method of supplying gate bias. S and Noise Parameters for various bias conditions are listed in this data sheet. The circuit shown in Figure 1 shows a typical LNA circuit normally used for 900 and 1900 MHz applications. Consult the Agilent Technologies web site for application notes covering specific designs and applications. High pass impedance matching networks consisting of L1/C1 and L4/C4 provide the appropriate match for noise figure, gain, S11 and S22. The high pass structure also provides low frequency gain reduction which can be beneficial

from the standpoint of improving out-of-band rejection.

Capacitors C2 and C5 provide a low impedance in-band RF bypass for the matching networks. Resistors R3 and R4 provide a very important low frequency termination for the device. The resistive termination improves low frequency stability. Capacitors C3 and C6 provide the RF bypass for resistors R3 and R4. Their value should be chosen carefully as C3 and C6 also provide a termination for low frequency mixing products. These mixing products are as a result of two or more in-band signals mixing and producing third order in-band distortion products. The low frequency or difference mixing products are terminated by C3 and C6. For best suppression of third order distortion products based on the CDMA 1.25 MHz signal spacing, C3 and C6 should be 0.1 uF in value. Smaller values of capacitance will not suppress the generation of the 1.25 MHz difference signal and as a result will show up as poorer two tone IP3 results.

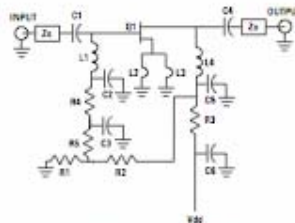


Figure 1. Typical ATF-551M4 LNA with Passive Biasing.

### Bias Networks

One of the major advantages of the enhancement mode technology is that it allows the designer to be able to dc ground the source leads and then merely

apply a positive voltage on the gate to set the desired amount of quiescent drain current Id.

Whereas a depletion mode PHEMT pulls maximum drain current when  $V_{gs} = 0V$ , an enhancement mode PHEMT pulls only a small amount of leakage current when  $V_{gs} = 0V$ . Only when  $V_{gs}$  is increased above  $V_{th}$ , the device threshold voltage, will drain current start to flow. At a  $V_{ds}$  of 2.7V and a nominal  $V_{gs}$  of 0.47V, the drain current  $I_d$  will be approximately 10 mA. The data sheet suggests a minimum and maximum  $V_{gs}$  over which the desired amount of drain current will be achieved. It is also important to note that if the gate terminal is left open circuited, the device will pull some amount of drain current due to leakage current creating a voltage differential between the gate and source terminals.

### Passive Biasing

Passive biasing of the ATF-551M4 is accomplished by the use of a voltage divider consisting of R1 and R2. The voltage for the divider is derived from the drain voltage which provides a form of voltage feedback through the use of R3 to help keep drain current constant. In the case of a typical depletion mode FET, the voltage divider which is normally connected to a negative voltage source is connected to the gate through resistor R4. Additional resistance in the form of R5 (approximately 10KΩ) is added to provide current limiting for the gate of enhancement mode devices such as the ATF-551M4. This is especially important when the device is driven to P1dB or Psat.

Resistor R3 is calculated based on desired  $V_{ds}$ ,  $I_{ds}$  and available power supply voltage.

$$R3 = \frac{V_{DD} - V_{ds}}{I_{ds} + I_{IBB}} \quad (1)$$

$V_{DD}$  is the power supply voltage.  
 $V_{ds}$  is the device drain to source voltage.  
 $I_{ds}$  is the desired drain current.  
 $I_{IBB}$  is the current flowing through the R1/R2 resistor voltage divider network.

The value of resistors R1 and R2 are calculated with the following formulas.

$$R1 = \frac{V_{gs}}{I_{IBB}} \quad (2)$$

$$R2 = \frac{(V_{ds} - V_{gs}) R1}{V_{gs}} \quad (3)$$

#### Example Circuit

$V_{DD} = 3V$   
 $V_{ds} = 2.7V$   
 $I_{ds} = 10 \text{ mA}$   
 $V_{gs} = 0.47V$

Choose  $I_{IBB}$  to be at least 10X the maximum expected gate leakage current.  $I_{IBB}$  was conservatively chosen to be 0.5 mA for this example. Using equations (1), (2), and (3) the resistors are calculated as follows

$R1 = 940\Omega$   
 $R2 = 4460\Omega$   
 $R3 = 28.6\Omega$

#### Active Biasing

Active biasing provides a means of keeping the quiescent bias point constant over temperature and constant over lot to lot variations in device dc performance. The advantage of the active biasing of an enhancement mode PHEMT versus a depletion mode PHEMT is that a negative power source is not required. The techniques of active biasing an enhancement mode device are very similar to those used to bias a bipolar junction transistor.

An active bias scheme is shown in Figure 2.

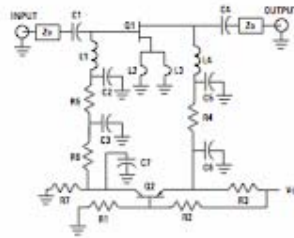


Figure 2. Typical ATF-551M4 LNA with Active Biasing.

R1 and R2 provide a constant voltage source at the base of a PNP transistor at Q2. The constant voltage at the base of Q2 is raised by 0.7 volts at the emitter. The constant emitter voltage plus the regulated  $V_{DD}$  supply are present across resistor R3. Constant voltage across R3 provides a constant current supply for the drain current. Resistors R1 and R2 are used to set the desired  $V_{gs}$ . The combined series value of these resistors also sets the amount of extra current consumed by the bias network. The equations that describe the circuit's operation are as follows.

$$V_E = V_{ds} + (I_{ds} \cdot R4) \quad (1)$$

$$R3 = \frac{V_{DD} - V_E}{I_{ds}} \quad (2)$$

$$V_B = V_E - V_{BE} \quad (3)$$

$$V_B = \frac{R1}{R1 + R2} V_{DD} \quad (4)$$

$$V_{DD} = I_{IBB} (R1 + R2) \quad (5)$$

Rearranging equation (4) provides the following formula

$$R2 = \frac{R1 (V_{DD} - V_B)}{V_B} \quad (4A)$$

and rearranging equation (5) provides the follow formula

$$R1 = \frac{V_{DD}}{I_{IBB} \left( 1 + \frac{V_{DD} - V_B}{V_B} \right)} \quad (5A)$$

#### Example Circuit

$V_{DD} = 3V$   
 $V_{ds} = 2.7V$   
 $I_{ds} = 10 \text{ mA}$   
 $R4 = 10\Omega$   
 $V_{BE} = 0.7V$

Equation (1) calculates the required voltage at the emitter of the PNP transistor based on desired  $V_{ds}$  and  $I_{ds}$  through resistor R4 to be 2.8V. Equation (2) calculates the value of resistor R3 which determines the drain current  $I_{ds}$ . In the example  $R3 = 18.2\Omega$ . Equation (3) calculates the voltage required at the junction of resistors R1 and R2. This voltage plus the step-up of the base emitter junction determines the regulated  $V_{gs}$ . Equations (4) and (5) are solved simultaneously to determine the value of resistors R1 and R2. In the example  $R1 = 4200\Omega$  and  $R2 = 1800\Omega$ .

R7 is chosen to be 1 k $\Omega$ . This resistor keeps a small amount of current flowing through Q2 to help maintain bias stability. R6 is chosen to be 10 K $\Omega$ . This value of resistance is high enough to limit Q1 gate current in the presence of high RF drive levels as experienced when Q1 is driven to the P1dB gain compression point. C7 provides a low frequency bypass to keep noise from Q2 effecting the operation of Q1. C7 is typically 0.1  $\mu$ F.

#### Maximum Suggested Gate Current

The maximum suggested gate current for the ATF-551M4 is 1 mA. Incorporating resistor R5 in the passive bias network or resistor R6 in the active bias network safely limits gate current to 500  $\mu$ A at P1dB drive levels. In order to minimize component count in the passive biased amplifier circuit, the 3 resistor bias circuit consisting of R1, R2, and R5 can be simplified if desired. R5 can be removed if R1 is replaced with a 5.6K $\Omega$  resistor



and if R2 is replaced with a 27KΩ resistor. This combination should limit gate current to a safe level.

### PCB Layout

A suggested PCB pad print for the miniature, Minipak 1412 package used by the ATF-551M4 is shown in Figure 3.

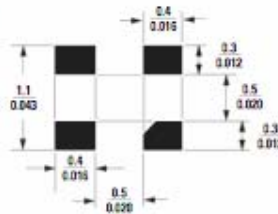


Figure 3. PCB Pad Print for Minipak 1412. Package (mm [inches]).

This pad print provides allowance for package placement by automated assembly equipment without adding excessive parasitics that could impair the high frequency performance of the ATF-551M4. The layout is shown with a footprint of the ATF-551M4 superimposed on the PCB pads for reference.

### ATF-551M4 Die Model

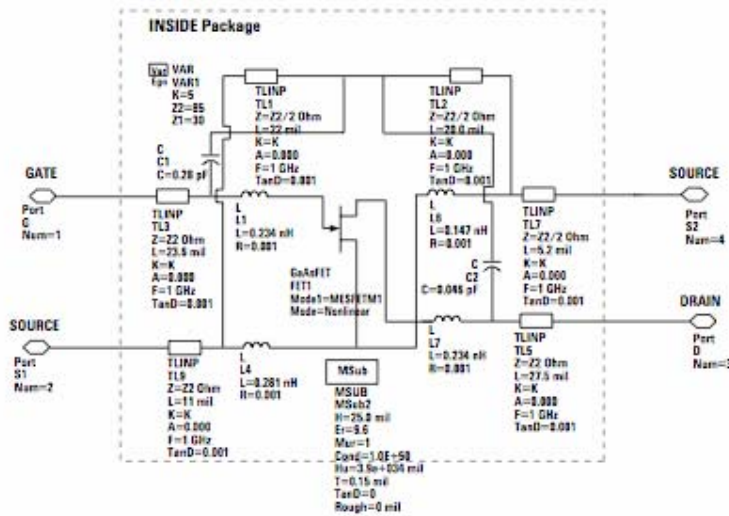


Advanced Curlice2_Model	Rf=	Crf=0.1 F	N=
MESFETM1	Gscap=2	Gsfwd=	Fnc=1 MHz
NFET=no	Cgs=0.6193 pF	Gsrsv=	R=0.08
Vto=0.3	Cgd=0.1435 pF	Gdfwd=	P=0.2
Beta=0.444	Gdscap=2	Gdrsv=	C=0.1
Lambda=72e-3	Fc=0.65	R1=	Tsumdl=no
Alpha=13	Rgd=0.5 Ohm	R2=	wVghwd=
Tau=	Rd=2.025 Ohm	Vbi=0.95	wVgs=
Tnom=16.85	Rg=1.7 Ohm	Vbr=	wVgd=
Idsc=	Rs=0.575 Ohm	Vjr=	wVds=
Ucrn=0.72	Ld=	Is=	wIdsmax=
Vgexp=1.91	Lg=0.094 nH	Ir=	wPmax=
Gamds=1e-4	Ls=	Imax=	AllParams=
Vtotc=	Cds=0.100 pF	Xci=	
Betacce=	Rc=390 Ohm	Eg=	
Rps=0.5 Ohm			

### For Further Information

The information presented here is an introduction to the use of the ATF-551M4 enhancement mode PHEMT. More detailed application circuit information is available from Agilent Technologies. Consult the web page or your local Agilent Technologies sales representative.

### ATF-551M4 Minipak Model

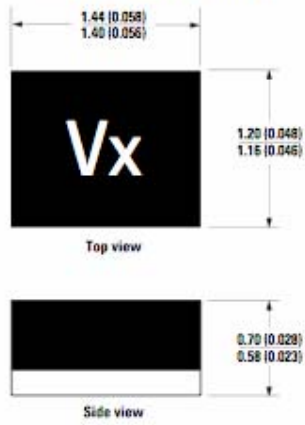




**Ordering Information**

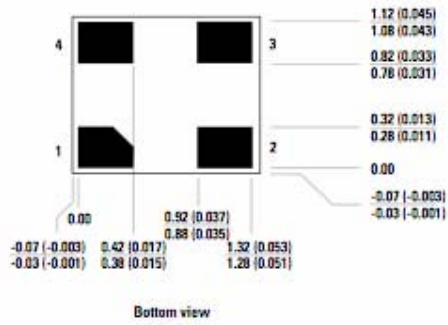
Part Number	No. of Devices	Container
ATF-551M4-TR1	3000	7" Reel
ATF-551M4-TR2	10,000	13" Reel
ATF-551M4-BLK	100	antistatic bag

**MiniPak Package Outline Drawing**

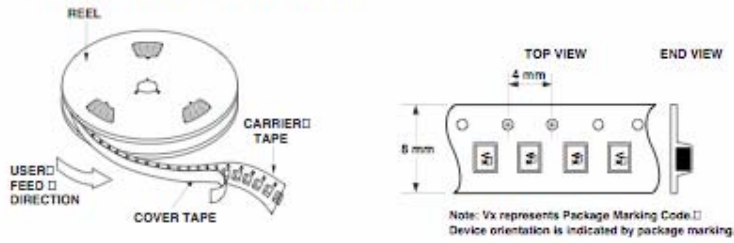


Dimensions are in millimeters (inches)

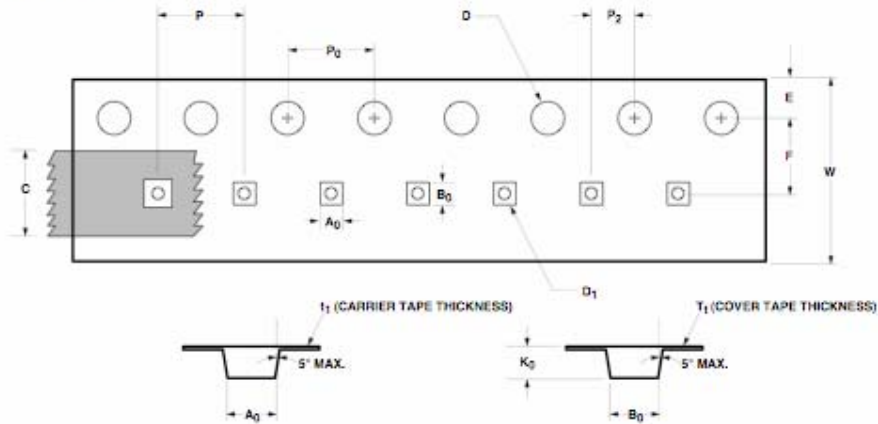
**Solder Pad Dimensions**



**Device Orientation for Outline 4T, MiniPak 1412**



**Tape Dimensions**



	DESCRIPTION	SYMBOL	SIZE (mm)	SIZE (INCHES)
CAVITY	LENGTH	A <sub>0</sub>	1.40 ± 0.05	0.055 ± 0.002
	WIDTH	B <sub>0</sub>	1.53 ± 0.05	0.064 ± 0.002
	DEPTH	K <sub>0</sub>	0.80 ± 0.05	0.031 ± 0.002
	PITCH	P	4.00 ± 0.10	0.157 ± 0.004
	BOTTOM HOLE DIAMETER	D <sub>1</sub>	0.80 ± 0.05	0.031 ± 0.002
	PERFORATION	DIAMETER	D	1.50 ± 0.10
PITCH		P <sub>0</sub>	4.00 ± 0.10	0.157 ± 0.004
POSITION		E	1.75 ± 0.10	0.069 ± 0.004
CARRIER TAPE	WIDTH	W	8.00 ± 0.30 - 0.10	0.315 ± 0.012 - 0.004
	THICKNESS	t <sub>1</sub>	0.254 ± 0.02	0.010 ± 0.0008
COVER TAPE	WIDTH	C	5.40 ± 0.10	0.213 ± 0.004
	TAPE THICKNESS	T <sub>1</sub>	0.062 ± 0.001	0.0024 ± 0.00004
DISTANCE	CAVITY TO PERFORATION (WIDTH DIRECTION)	F	3.50 ± 0.05	0.138 ± 0.002
	CAVITY TO PERFORATION (LENGTH DIRECTION)	P <sub>2</sub>	2.00 ± 0.05	0.079 ± 0.002

For product information and a complete list of Agilent contacts and distributors, please go to our web site:  
[www.agilent.com/semiconductors](http://www.agilent.com/semiconductors)  
 E-mail: SemiconductorSupport@agilent.com  
 Date subject to change.  
 Copyright © 2004 Agilent Technologies, Inc.  
 Obsolete: 5988-4455EN  
 July 16, 2004  
 5988-6001EN



## Appendix E

### Surface Coil Components List.

Reference	Manufacturer	Part Number	Description	Supplier	Supplier Part Number
C1, C3,Cc	Sprague-Goodman	GKG20066-07	VAR-CAP, 4.5-20pF	Digikey	SG2003CT-ND
C2	Sprague-Goodman	GKG6R066-07	VAR-CAP, 2.0-6pF	Digikey	SG2001CT-ND
CL1	Voltronics Corp	11 Series	11 Series Cap 24pF	Voltronics Corp	11 Series
CL2	Voltronics Corp	11 Series	11 Series Cap 12pF	Voltronics Corp	11 Series
L1	Toko America	656LZ-08K=P3	41.1nH	Digikey	TKS2680CT-ND
L2	J W Miller Magnetics	PM1008-1R5K	1.5uH	Digikey	M1202CT-ND
D1	MACOM	MA4P7470F1072 T	Diode	MACOM	MA4P7470F-1072T
Cable	Belden	#9222	Cable	Belden	#9222

### Dual stage Preamplifier Components List.

Reference	Manufacturer	Part Number	Description	Supplier	Supplier Part Number
LD1, LD2	API Delevan Inc	1210-561K	0.56uH	Digikey	Dn10561CT-ND
LM1	Murata Electronics	LQW18AN22NJ0 0D	22nH	Digikey	490-1173-1-ND
LM2	Murata Electronics	LQW18AN27NJ0 0D	27nH	Digikey	490-1174-2-ND
LF1, LF2, LF3, LF4	Panasonic	ELJ-FJR39GF2	390nH	Digikey	PCD1609CT-ND

LM3	Panasonic	ELJ-RE2N2DF2	2.2nH	Digikey	PCD1143CT-ND
CD1, CD2	Panasonic	ECJ-3FB2J102K	1000pF	Digikey	PCC2291CT-ND
CM1	Murata Electronics	GRM1885C1H5R0CZ01D	5.0pF	Digikey	490-1390-1-ND
CM2	Murata Electronics	GRM1885C1H3R6CZ01D	3.6pF	Digikey	490-1385-1-ND
CB1,CB2, CB3,CB4	Murata Electronics	GRM1885C1H102JA01D	1000pF	Digikey	490-1451-1-ND
C1, C2, C3 C4	Panasonic	ECJ-1VB0J105K	1.0uF	Digikey	PCC1915CT-ND
C5, C6	Panasonic	ECJ-1VB1C104K	0.1uF	Digikey	PCC1762CT-ND
RL1, RR1	Yageo America	9C06031A4301F KHFT	4.30K $\Omega$	Digikey	311-4.30KHCT-ND
RL2, RR2	Yageo America	9C06031A5761F KHFT	5.76K $\Omega$	Digikey	311-5.76KHCT-ND
RL3, RR3	Yageo America	9C06031A1430F KHFT	143 $\Omega$	Digikey	311-143HCT-ND
RL4, RR4	Yageo America	9C06031A10R0F KHFT	10 $\Omega$	Digikey	311-10.0HCT-ND
RL5, RR5	Yageo America	9C06031A1002F KHFT	10K $\Omega$	Digikey	311-10.0KHCT-ND
RL6, RR6	Yageo America	9C06031A1001F KHFT	1.0K $\Omega$	Digikey	311-1.00KHCT-ND
RM2, RM4	Yageo America	9C06031A93R1F KHFT	93 $\Omega$	Digikey	311-93.1HDR-ND
RM3	Yageo America	9C06031A76R8F KHFT	76.8 $\Omega$	Digikey	311-76.8HCT-ND
RM6	Yageo America	9C06031A75R0F KHFT	75 $\Omega$	Digikey	311-75.0HCT-ND
M1, M2	Agilent	ATF-551M4-BLK	ATF-551M4	Agilent	ATF-551M4-BLK
PNP1, PNP2	Panasonic	2SB1219ASL	PNP	Digikey	2SB1219ASLCT-ND
D1, D2	Panasonic	MA2SP0100L	Pin diode	Digikey	MA2SP0100LCT-ND